

Proceedings of the third
“international Traveling Workshop
on Interactions between Sparse models
and Technology”

iTWIST'16

Aalborg, Denmark

August 24-26, 2016.



iTWIST'16 PRESENTATION

The third edition of the “*international - Traveling Workshop on Interactions between Sparse models and Technology*” (iTWIST) will take place in Aalborg, the 4th largest city in Denmark situated beautifully in the northern part of the country. The workshop venue will be at the Aalborg University campus.

One implicit objective of this biennial workshop is to foster collaboration between international scientific teams by disseminating ideas through both specific oral/poster presentations and free discussions.

For this third edition, iTWIST'16 gathers about 50 international participants and features 8 invited talks, 12 oral presentations, and 12 posters on the following themes, all related to the theory, application and generalization of the “sparsity paradigm”:

- ▶ Sparsity-driven data sensing and processing (e.g., optics, computer vision, genomics, biomedical, digital communication, channel estimation, astronomy)
- ▶ Application of sparse models in non-convex/non-linear inverse problems (e.g., phase retrieval, blind deconvolution, self calibration)
- ▶ Approximate probabilistic inference for sparse problems
- ▶ Sparse machine learning and inference
- ▶ “Blind” inverse problems and dictionary learning
- ▶ Optimization for sparse modelling
- ▶ Information theory, geometry and randomness
- ▶ Sparsity? What's next?
 - ▶ Discrete-valued signals
 - ▶ Union of low-dimensional spaces,
 - ▶ Cosparsity, mixed/group norm, model-based, low-complexity models, ...
- ▶ Matrix/manifold sensing/processing (graph, low-rank approximation, ...)
- ▶ Complexity/accuracy tradeoffs in numerical methods/optimization
- ▶ Electronic/optical compressive sensors (hardware)

SCIENTIFIC ORGANIZING COMMITTEE

- ▶ **Thomas Arildsen** (general chair)
Department of Electronic Systems at Aalborg University, Denmark.
- ▶ **Morten Nielsen** (co-chair)
Department of Mathematical Sciences at Aalborg University, Denmark.
- ▶ **Laurent Jacques**
Institute of Information and Communication Technologies,
Electronics and Applied Mathematics (ICTEAM) at Université catholique de Louvain, Belgium.
- ▶ **Sandrine Anthoine**
Marseille Institute of Mathematics, at Aix-Marseille Université and CNRS, France.
- ▶ **Yannick Boursier**
Center for Particle Physics of Marseille, at Aix-Marseille Université and CNRS, France.
- ▶ **Aleksandra Pizurica**
Department of Telecommunications and Information Processing at Ghent University, Belgium.
- ▶ **Pascal Frossard**
Electrical Engineering Institute at Ecole Polytechnique Fédérale de Lausanne, Switzerland.
- ▶ **Pierre Vandergheynst**
Electrical Engineering Institute at Ecole Polytechnique Fédérale de Lausanne, Switzerland.
- ▶ **Christine De Mol**
Department of Mathematics and ECARES (European Center for Advanced Research in Economics and Statistics) at Brussels Free University, Belgium.
- ▶ **Christophe De Vleeschouwer**
Institute of Information and Communication Technologies,
Electronics and Applied Mathematics (ICTEAM) at Université catholique de Louvain, Belgium.

Table of contents

- “Sparse matrix factorization for PSFs field estimation” (p. 1)
F. Ngolè (CEA Saclay, France) and J.-L. Starck (CEA Saclay, France).
- “Sparse BSS with corrupted data in transformed domains”..... (p. 4)
C. Chenot (IRFU, CEA, France) and J. Bobin (IRFU, CEA, France).
- “Randomness is sufficient! Approximate recovery from CS samples”..... (p. 7)
V. Abrol (SCEE, IIT Mandi, India), P. Sharma (SCEE, IIT Mandi, India) and Anil K. Sao (SCEE, IIT Mandi, India).
- “The Effect of Atom Replacement Strategies on Dictionary Learning”..... (p. 10)
Paul Irofti (U. Politehnica Bucharest, Romania).
- “Blind Deconvolution of PET Images using Anatomical Priors”..... (p. 12)
Stéphanie Guérit (UCLouvain, Belgium), Adriana González (UCLouvain, Belgium) (UCLouvain, Belgium), Anne Bol (UCLouvain, Belgium), John A. Lee (UCLouvain, Belgium) and Laurent Jacques (UCLouvain, Belgium).
- “A Non-Convex Approach to Blind Calibration for Linear Random Sensing Models”..... (p. 15)
Valerio Cambareri (UCLouvain, Belgium) and Laurent Jacques (UCLouvain, Belgium).
- “Sparse Support Recovery with ℓ_∞ Data Fidelity”..... (p. 18)
Kévin Degraux (UCLouvain, Belgium), Gabriel Peyré (CNRS, Ceremade, U. Paris-Dauphine, France), Jalal M. Fadili (ENSICAEN, UNICAEN, GREYC, France) and Laurent Jacques (UCLouvain, Belgium).
- “Low Rank and Group-Average Sparsity Driven Convex Optimization for Direct Exoplanets Imaging”..... (p. 21)
Benoît Pairet (UCLouvain, Belgium), Laurent Jacques (UCLouvain, Belgium), Carlos A. Gomez Gonzalez (ULg, Belgium), Olivier Absil (ULg, Belgium).
- “A fast algorithm for high-order sparse linear prediction”..... (p. 24)
Tobias Lindstrøm Jensen (Aalborg Universitet, Denmark), Daniele Giacobello (DTS Inc., Calabasas, CA, USA), Toon van Waterschoot (KULeuven, Belgium), Mads Græsbøll Christensen (Aalborg Universitet, Denmark).
- “Compressive Hyperspectral Imaging with Fourier Transform Interferometry”..... (p. 27)
A. Moshtaghpour (UCLouvain, Belgium), K. Degraux (UCLouvain, Belgium), V. Cambareri (UCLouvain, Belgium), A. Gonzalez (UCLouvain, Belgium), M. Roblin (Lambda-X, Belgium), L. Jacques (UCLouvain, Belgium), and P. Antoine (Lambda-X, Belgium).
- “Inferring Sparsity: Compressed Sensing using Generalized Restricted Boltzmann Machines”..... (p. 30)
Eric W. Tramel (Ecole Normale Supérieure, PSL Research University, France), Andre Manoel (Ecole Normale Supérieure, PSL Research University, France), Francesco Caltagirone (INRIA Paris), Marylou Gabrié (Ecole Normale Supérieure, PSL Research University, France) and Florent Krzakala (Ecole Normale Supérieure, PSL Research University, France).
- “Interpolation on manifolds using Bézier functions”..... (p. 33)
Pierre-Yves Gousenbourger (UCLouvain, Belgium), P.-A. Absil (UCLouvain, Belgium), Benedikt Wirth (U. Münster, Germany) and Laurent Jacques (UCLouvain, Belgium).
- “Reliable recovery of hierarchically sparse signals”..... (p. 36)
Ingo Roth (Freie Universität Berlin, Germany), Martin Kliesch (Freie Universität Berlin, Germany), Gerhard Wunder (Freie Universität Berlin, Germany), and Jens Eisert (Freie Universität Berlin, Germany).

- “Minimizing Isotropic Total Variation without Subiterations”..... (p. 39)
Ulugbek S. Kamilov (MERL, USA).
- “Learning MMSE Optimal Thresholds for FISTA”..... (p. 42)
Ulugbek S. Kamilov (MERL, USA) and Hassan Mansour (MERL, USA).
- “The best of both worlds: synthesis-based acceleration
for physics-driven cosparsity regularization”..... (p. 45)
Srđan Kitić (Technicolor R&D, France), Nancy Bertin (CNRS - UMR 6074, France) and Rémi Gribonval (Inria, France).
- “A Student-t based sparsity enforcing hierarchical prior for linear inverse problems
and its efficient Bayesian computation for 2D and 3D Computed Tomography”..... (p. 48)
Ali Mohammad-Djafari (CentraleSupélec-U. Paris Saclay, France), Li Wang (CentraleSupélec-U. Paris Saclay, France),
Nicolas Gac (CentraleSupélec-U. Paris Saclay, France) and Folkert Bleichrodt (CWI, The Netherlands).
- “Simultaneous reconstruction and separation in a spectral CT framework”..... (p. 50)
S. Tairi (CPPM, France), S. Anthoine (Aix Marseille Université, France), C. Morel (CPPM, France) and Y. Boursier
(CPPM, France).
- “Debiasing incorporated into reconstruction of low-rank modelled dynamic MRI data”..... (p. 53)
Marie Daňková (Brno University of Technology & Masaryk University, Czech Republic) and Pavel Rajmic (Brno University
of Technology, Czech Republic).
- “Sparse MRI with a Markov Random Field Prior for the Subband Coefficients”..... (p. 56)
Marko Panić (University of Novi Sad, Serbia), Dejan Vukobratovic (University of Novi Sad, Serbia), Vladimir Crnojević
(University of Novi Sad, Serbia) and Aleksandra Pižurica (Ghent University, Belgium).
- “Active GAP screening for the LASSO”..... (p. 59)
A. Bonnefoy (Aix Marseille Université, France) and S. Anthoine (Aix Marseille Université, France).
- “Paint Loss Detection in Old Paintings by Sparse Representation Classification”..... (p. 62)
Shaoguang Huang (Ghent University, Belgium), Wenzhi Liao (Ghent University, Belgium), Hongyan Zhang (Wuhan Uni-
versity, China) and Aleksandra Pižurica (Ghent University, Belgium).

Sparse matrix factorization for PSFs field estimation

F. Ngolè¹ and J.-L. Starck¹.

¹Laboratoire AIM, CEA/DSM-CNRS-Universite Paris Diderot, Irfu, Service d'Astrophysique, CEA Saclay, Orme des Merisiers, 91191 Gif-sur-Yvette, France.

Abstract— In large-scale spatial surveys, the Point Spread Function (PSF) varies across the instrument field of view (FOV). Local measurements of the PSFs are given by the isolated stars images. Yet, these estimates may not be directly usable because of the observational noise and the aliasing.

Given a set of aliased and noisy stars images from a telescope, we want to estimate well-resolved and noise-free PSFs at the observed stars positions, exploiting the spatial correlation of the PSFs across the FOV.

We introduce RCA (Resolved Components Analysis) which is a dimension reduction and super-resolution method based on matrix-factorization. We propose an original way of using the PSFs spatial correlation in the restoration process through sparsity.

We tested RCA on simulated PSFs of Euclid telescope. We show that a coupled sparsity constraint on individual PSFs and their spatial distribution improves significantly the accuracy over the restored PSFs shapes, compared to existing methods.

1 Introduction

In many applications such as astronomical or biomedical imaging, the optical system introduces a blurring of the images that needs to be taken into account for scientific analyses. The blurring function, also called Point Spread Function (PSF), is not always stationary on the observed field of view (FOV). A typical example is the case of the Euclid space mission [1], to be launched in 2020, where we need to measure with a very high accuracy the shapes of more than one billion of galaxies. An extremely important step to derive such measurements is to get an estimate of the PSF at any spatial position of the observed images.

In astronomical imaging, unresolved objects such as stars, can provide PSFs measurements at different locations in the FOV. Nevertheless, these images can be aliased given the CCD sensors sizes which makes a super-resolution (SR) step necessary.

In this paper, we consider the case where the PSF is both space variant and under-sampled, and we want to get an accurate modeling at high resolution of the PSFs, assuming we have under-sampled measurements of different PSFs in the observed field. We assume that the PSFs vary slowly across the field. This implies a compressibility of the PSFs field which we define as the smallest manifold on which the PSFs lie. which raises the question of what would be a concise representation of a spatially indexed set of PSFs accounting for the regularity of the PSFs field.

Several methods in the spatial data processing literature give possible answers to this question, in the case there is no under-sampling. For instance, in [2, 3, 4] the authors proposed "PCA-based" methods that explicitly include spatial constraints in the dimension reduction. Other interesting dimension reduction methods can be found in [7] and [5, 6]; the former builds an hierarchical representation of the data set, by identifying corre-

lated samples entries; the latter provides a sparse representation of data lying on a low dimensional manifold. To the best of our knowledge, the only method performing both restoration, dimension reduction and super-resolution is the one used in the PSF modeling software PSFEx [8], which assumes a polynomial dependency of the PSFs low dimensional coordinates to the PSFs spatial positions in the FOV.

While the present work deals with the estimation of the PSFs from degraded measurements, a method for implementing efficiently a spatially varying blurring operator is introduced in [9], relying on similar compressibility priors.

2 Data model

We assume that we have an image I , which contains p unresolved objects such as stars, which can be used to estimate the PSFs. Noting \mathbf{y}_k one of these p objects at spatial position \mathbf{u}_k , \mathbf{y}_k is therefore a small patch of I with n_y pixels, around the spatial position \mathbf{u}_k . We will write \mathbf{y}_k as a 1D vector. The relation between the "true" PSF \mathbf{x}_k and the noisy \mathbf{y}_k observation is

$$\mathbf{y}_k = \mathbf{M}_k \mathbf{x}_k + \mathbf{n}_k, \quad (1)$$

where \mathbf{M}_k is a linear operator and \mathbf{n}_k is a noise that we assume to be Gaussian and white. We will consider two kinds of operators in this paper: the first one is the simple case where $\mathbf{M}_k = \mathbf{I}_{n_x}$ and we have the number of pixels n_x in \mathbf{x}_k is equal to n_y . The second one is a registration+downsampling degradation operator and $n_x = m_d^2 n_y$, where m_d is the downsampling factor. This case corresponds to the situation where the observations are aliased and one wish to compute the PSFs at a finer resolution. The registration is a simple translation shift which accounts for the fact that the observed stars centroids are not randomly distributed at a subpixelic level; this is in fact necessary for the resolution enhancement to be possible.

Noting $\mathbf{Y} = [\mathbf{y}_1 \cdots \mathbf{y}_p]$ the matrix of n_y lines and p columns of all observed patches, $\mathbf{X} = [\mathbf{x}_1 \cdots \mathbf{x}_p]$ the matrix $n_x \times p$ of all unknown PSF, we can rewrite Eq. 1 as

$$\mathbf{Y} = \mathcal{F}(\mathbf{X}) + \mathbf{N}, \quad (2)$$

where $\mathcal{F}(\mathbf{X}) = [\mathbf{M}_1 \mathbf{x}_1, \dots, \mathbf{M}_p \mathbf{x}_p]$.

We assume that the registered PSFs live in a r dimensional subspace Ω of \mathbb{R}^{n_x} , with $r \ll \min(n_x, p)$. The PSFs field is therefore included in Ω . Let $(\mathbf{s}_i)_{1 \leq i \leq r}$ be a basis of Ω . By definition, we can write

$$\mathbf{X} = \mathbf{S} \mathbf{A}, \quad (3)$$

where $\mathbf{S} = [\mathbf{s}_1, \dots, \mathbf{s}_r]$ and \mathbf{A} is a $r \times p$ matrix containing the coefficients $\mathbf{A}[:, k]$ of the vectors \mathbf{x}_k ($k = 1 \dots p$) in the dictionary \mathbf{S} . Therefore, we will be considering the optimization problem

$$\min_{\mathbf{A}, \mathbf{S}} \|\mathbf{Y} - \mathcal{F}(\mathbf{S} \mathbf{A})\|_F^2, \quad (4)$$

subject to various constraints that we precise in the next section.

3 Proposed method

3.1 Constraints

We introduce the Resolved Components Analysis (RCA), which is dimension reduction and super-resolution method based on the following priors:

- positivity constraint: the PSFs \mathbf{x}_k should be positive;
- low rank constraint: as described above, we assume that $\mathbf{x}_k = \sum_{i=1}^r a_{ik} \mathbf{s}_i$, with $r \ll \min(n_x, p)$; this dimension reduction has the advantage that there are much less unknown to find, leading to more robustness;
- smoothness constraint: we can assume that \mathbf{x}_k vectors are structured; the low rank constraint does not necessary impose \mathbf{x}_k to be smooth or piece-wise smooth; adding an additional constraint on \mathbf{S} atoms, such as a sparsity constraint, allows to capture spatial correlation within the PSFs themselves; an additional dictionary Φ_s can therefore be introduced which is assumed to give a sparse representation of the vectors \mathbf{s}_k ;
- proximity constraints: we can assume that a given \mathbf{x}_k at a position \mathbf{u}_k is very close to another PSF $\mathbf{x}_{k'}$ at position $\mathbf{u}_{k'}$ if the distance between \mathbf{u}_k and $\mathbf{u}_{k'}$ is small; this means that the field f must be regular; this regularity can be forced by adding constraints on the lines of the matrix \mathbf{A} ; indeed, the p values relative to a line $\mathbf{A}[i, :]$ correspond to the contribution of the i th *eigen PSF* relative to different locations in the FOV.

Since we do not estimate individual PSFs directly, the smoothness constraint is introduced by promoting \mathbf{S} 's columns sparsity with respect to a chosen dictionary Φ_s . By definition, a typical imaging system's PSF concentrates most of its power in few pixels. Therefore a straightforward choice for Φ_s is \mathbf{I}_{n_x} . In other words, we will enforce the sparsity of \mathbf{S} 's columns in the pixels domain.

On the other hand, we take Φ_s as the second generation Starlet forward transform [11] which is particularly suitable for images with nearly isotropic features.

As previously stated, the proximity constraint relies on the structure of the matrix \mathbf{A} . Each line of \mathbf{A} is calculated as a sparse linear combination of discrete approximated harmonics defined over the set of spatial positions $\{\mathbf{u}_k, k = 1 \dots p\}$: we have $\mathbf{A} = \alpha \mathbf{V}^T$, where α is a $n_x \times q$ matrix with sparse lines, and \mathbf{V} is a $p \times q$ matrix whose columns are approximated harmonics, for some integer q . By representing each line of \mathbf{A} by a few number of harmonics, the highest field's frequencies in the observations tend to be discarded, since they carry less energy than the lower frequencies because of the PSFs field smoothness. This, in turn, enforces local similarity of the PSFs. The dictionary \mathbf{V} is built as follows:

- we define a family of quadratic forms over the set $\{\mathbf{u}_k, k = 1 \dots p\}$ which eigenvectors are discrete harmonics if the \mathbf{u}_k 's are uniformly distributed on a 2D cartesian grid;
- we form the dictionary \mathbf{V} by concatenating these eigenvectors.

3.2 Algorithm

The aforementioned constraints lead us to the following optimization problem:

$$\min_{\alpha, \mathbf{S}} \frac{1}{2} \|\mathbf{Y} - \mathcal{F}(\mathbf{S}\alpha \mathbf{V}^T)\|_F^2 + \sum_{i=1}^r \|\mathbf{w}_i \odot \Phi_s \odot \mathbf{s}_i\|_1 \quad (5)$$

$$\text{s.t. } \|\alpha[l, :]\|_0 \leq \eta_l, \quad l = 1 \dots r \text{ and } \mathbf{S}\alpha \mathbf{V}^T \geq 0. \quad (6)$$

where the last inequality is entry-wise and \odot denotes the Hadamard product. The ℓ_1 term promotes the sparsity of \mathbf{S} columns with respect to Φ_s . The vectors $(\mathbf{w}_i)_i$ weight the sparsity against the other constraints and allow some adaptivity of the penalty, with respect to the uncertainties propagated to each entry of \mathbf{S} [10].

The Problem 6 being non-convex, we solve approximately using the following alternate scheme[12]:

1. Initialization: $\alpha_0 \in M_{r, rp}(\mathbb{R})$,
 $\mathbf{S}_0 = \underset{\mathbf{S}}{\operatorname{argmin}} \frac{1}{2} \|\mathbf{Y} - \mathcal{F}(\mathbf{S}\alpha_0 \mathbf{V}^T)\|_F^2 + \sum_{i=1}^r \|\mathbf{w}_i \odot \Phi_s \odot \mathbf{S}[:, i]\|_1$ s.t. $\mathbf{S}\alpha_0 \mathbf{V}^T \geq 0$
2. For $k = 0 \dots k_{\max}$:
 - (a) $\alpha_{k+1} = \underset{\alpha}{\operatorname{argmin}} \frac{1}{2} \|\mathbf{Y} - \mathcal{F}(\mathbf{S}_k \alpha \mathbf{V}^T)\|_F^2$
 s.t. $\|\alpha[l, :]\|_0 \leq \eta_l, \quad l = 1 \dots r$,
 - (b) $\mathbf{S}_{k+1} = \underset{\mathbf{S}}{\operatorname{argmin}} \frac{1}{2} \|\mathbf{Y} - \mathcal{F}(\mathbf{S}\alpha_{k+1} \mathbf{V}^T)\|_F^2 + \sum_{i=1}^r \|\mathbf{w}_i \odot \Phi_s \odot \mathbf{S}[:, i]\|_1$ s.t. $\mathbf{S}\alpha_{k+1} \mathbf{V}^T \geq 0$.

The optimization problem involved in step (a) remains non-convex but is approximately solved using an heuristic based on iterative hard-thresholding [13]. The optimization problem involved in step (b) is solved using an instance of the family of algorithms described in [14].

4 Results

We tested RCA on simulated optical Euclid PSFs as in [10], downsampled to Euclid resolution. We compared our approach to the standard PCA and the methods presented in [5] and [8] respectively.

The proposed method with Φ_s chosen as a wavelet's is at least one order of magnitude more accurate with respect to the PSFs ellipticities and sizes [15, 16, 17] and the pixels mean square error, with and without downsampling. An example is given in Fig. 1.

5 Conclusion

We introduced RCA which is a dimension reduction method for continuous and positive data field which is noise robust and handles undersampled data. As a linear dimension reduction method, RCA computes the input data as linear combinations of few components which are estimated, as well as the linear combination coefficients, through a matrix factorization.

The method was tested over a field of simulated Euclid telescope PSFs. We show that constraining both the components matrix and the coefficients matrix using sparsity yield at least one order of magnitude more accurate PSFs restoration than existing methods, with respect to the PSFs shapes parameters; in particular, constraining the coefficients matrix yields a significantly better identification of the PSFs embedding subspace when the data are undersampled.

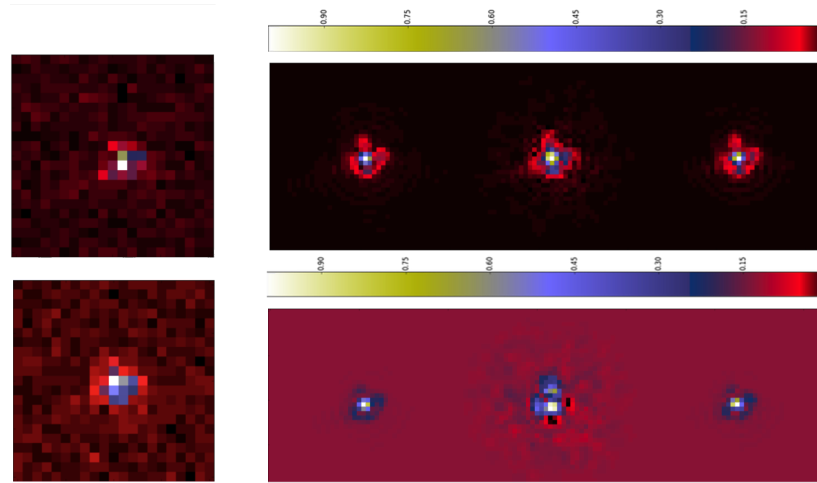


Figure 1: Example of reconstructions from undersampled images; from the left to the right: observation, original, PSFEX, RCA.

References

- [1] ESA/SRE, “EUCLID Mapping the geometry of the dark universe”, 2011
- [2] W.-T. Wang and H.-C. Huang, “Regularized Principal Component Analysis for Spatial Data”, ArXiv e-prints, 1501.03221, 2015
- [3] Qiuming Cheng, “Spatial and Spatially Weighted Principal Component Analysis for Images Processing”, IEEE International Conference on Geoscience and Remote Sensing Symposium, 972-975, 2006.
- [4] P. Harris, C. Brunson and M. Charlton, “Geographically weighted principal components analysis”, International Journal of Geographical Information Science, **25**(10):1717-1736, 2011.
- [5] W.K. Allard, G. Chen and M. Maggioni, “Multiscale Geometric Methods for Data Sets II: Geometric Multi-Resolution Analysis”, ArXiv e-prints, 1105.4924, 2011
- [6] M. Maggioni, S. Minsker and N. Strawn, “Multiscale Dictionary Learning: Non-Asymptotic Bounds and Robustness”, ArXiv e-prints, 1401.5833, 2014.
- [7] A.B. Lee, B. Nadler and L. Wasserman, “Treelets—An adaptive multi-scale basis for sparse unordered data”, The Institute of Mathematical Statistics, **2**(2): 435-471, 2008.
- [8] E. Bertin, “Automated Morphometry with SExtractor and PSFEX”, Astronomical Data Analysis Software and Systems XX, **442**:435, 2011.
- [9] P. Escande and P. Weiss, “Sparse wavelet representations of spatially varying blurring operators”, SIAM Journal on Imaging Sciences, **8**(4):2976-3014, 2015.
- [10] F. Ngolè, J.-L. Starck, S. Ronayette, K. Okumura and J. Amiaux, “Super-resolution method using sparse regularization for point-spread function recovery”, Astronomy & Astrophysics, 1410.7679, 2015.
- [11] J.-L. Starck, F. Murtagh and M. Bertero, “Starlet Transform in Astronomical Data Processing”, Handbook of Mathematical Methods in Imaging, 1489-1531, 2011.
- [12] Amir Beck, “On the Convergence of Alternating Minimization for Convex Programming with Applications to Iteratively Reweighted Least Squares and Decomposition Schemes”, SIAM Journal on Optimization, **25**(1): 185-209, 2015.
- [13] T. Blumensath and M. Davies, “Iterative Thresholding for Sparse Approximations”, Journal of Fourier Analysis and Applications, **14**(5-6): 629-654, 2008.
- [14] P.-L. Combettes, L. Condat and J.-C. Pesquet and B. Cong Vu, “A forward-backward view of some primal-dual optimization methods in image recovery”, ArXiv e-prints, 1406.5439, 2014.
- [15] M. Cropper et al., “Defining a weak lensing experiment in space”, Monthly Notices of the Royal Astronomical Society, **431** 1210.7691, 2013.
- [16] Paulin-Henriksson, “Point spread function calibration requirements for dark energy from cosmic shear”, Astronomy & Astrophysics, **484**: 67-77, 2008.
- [17] S. Dodelson, “Weak lensing and polarization”, Modern Cosmology, 292 - III, 2003.

Sparse BSS with corrupted data in transformed domains

C. Chenot and J. Bobin.

IRFU, CEA, Université Paris-Saclay, F-91191 Gif-sur-Yvette, France

Abstract— The presence of corrupted data is not innocuous when analyzing multichannel data. Most techniques of Blind Source Separation (BSS), well-suited to extract the meaningful information from the observations, are sensitive to gross errors. We propose a new method for handling outliers, assuming that their morphology is different from the one of the sources. The proposed method is two-step. Firstly, an initializing scheme using MCA and AMCA is performed. Then the mixing matrix, the outliers and the sources are jointly estimated by employing a reweighting procedure. Preliminary numerical experiments show the effectiveness of the proposed method compared to the state-of-the-art algorithms.

1 Introduction

We consider m multichannel observations $\{\mathbf{X}_i\}_{i=1..m}$, corresponding to the linear mixture of $n \leq m$ sources $\{\mathbf{S}_j\}_{j=1..n}$ with $t > m$ samples. Besides, we assume that these measurements can be corrupted by a Gaussian noise accounting for small and dense noise and also by few large errors, designated as outliers. The model can be recast with the following matrix form:

$$\mathbf{X} = \mathbf{AS} + \mathbf{O} + \mathbf{N},$$

where $\mathbf{X} \in \mathbf{R}^{m \times t}$ stands for the observations, $\mathbf{A} \in \mathbf{R}^{m \times n}$ the mixing matrix, $\mathbf{S} \in \mathbf{R}^{n \times t}$ the sources, $\mathbf{O} \in \mathbf{R}^{m \times t}$ the outliers, and $\mathbf{N} \in \mathbf{R}^{m \times t}$ the Gaussian noise.

The outliers designate large corrupted entries in the measurements which can encompass errors done by defective sensors or large local mismodeling deviations for instance. According to the rarity of these errors, we will consider that \mathbf{O} is sparse in the direct domain. Besides, we assume that the outliers are in general position: they do not cluster in any specific direction. For this purpose, we will assume in the following that the outliers corrupt independently some columns of \mathbf{X} . In hyperspectral imaging for instance, this corresponds to the presence of spectrally distinct anomalies in the observed scene.

Although the percentage of corrupted data is generally low, the presence of outliers is common in real-world applications. Unfortunately, few BSS methods are able to handle them. In the ICA framework, the authors of [1] propose to promote the independence of the sources by using the β -divergence instead of the Kullback-Leibler divergence [2] which is sensitive to outliers. Another approach consists in, if $m \gg n$, separating the low-rank term \mathbf{AS} from the sparse outliers [3] and then applying a BSS technique on the denoised observations. This has particularly been popularized in hyperspectral imaging, where the low-rank assumption is valid [4], [5]. Last, the outliers, the sources and the mixing matrix can be jointly estimated using appropriate priors for each components such as the non-negativity of \mathbf{A} and \mathbf{S} in [6], [7], [8], and

[9] or the parsimony of \mathbf{O} and \mathbf{S} in a same dictionary [10], [11].

In many domains such as astrophysics [12], the sought-after signals are not sparse in the direct domain whereas the outliers can still be considered as being sparse in the direct domain, or at least are sparse in another dictionary than the one used for the sources. To the best of our knowledge, the difference of morphology between sources and outliers has not been exploited to retrieve robustly the mixing matrix, the sources and the outliers simultaneously. We propose a two-steps method to perform the BSS problem in the presence of outliers taking advantage of the difference of morphology between outliers and the sources, as well as the clustering structure of the term \mathbf{AS} .

2 Optimization problems

We consider that the outliers are sparse in the direct domain and some of its columns are active. The sources are assumed to be sparse in the dictionary Φ . To estimate jointly \mathbf{A} , \mathbf{S} and \mathbf{O} , we propose to minimize the following problem:

$$\underset{\mathbf{A}, \mathbf{S}, \mathbf{O}}{\text{minimize}} \frac{1}{2} \|\mathbf{X} - \mathbf{AS} - \mathbf{O}\|_2^2 + \lambda \|\mathbf{S}\Phi\|_1 + \beta \|\mathbf{O}\|_{2,1}, \quad (1)$$

where the first term is the data fidelity term, the second one favors sources having a sparse representation in Φ and last, the third term promotes outliers with few entirely active columns. The main difficulty in the minimization of the above problem is its non-convexity due to the product \mathbf{AS} . In the presence of large outliers, it would be nearly impossible to recover the signals if the problem were not correctly initialized. That is why, we adopt a two-step method: the first one consists in finding a good initialization point and then to minimize eq.1.

2.1 Initialization step

The aim of this step is to obtain a good starting point to then minimize eq.1 without being trapped into a local minimum located away from the global optimum. To do so, the outliers are firstly separated from \mathbf{AS} by using a modified MCA [13] and then the sources are unmixed from the outliers-free observations by using AMCA [14] as follows:

Initialization: rmMCA

Input \mathbf{X} , Φ
 Separate $\tilde{\mathbf{O}}$ from $\tilde{\mathbf{A}}\tilde{\mathbf{S}}$ with $MCA_{\ell_{2,1}}$:

$$\underset{\mathbf{O}, \mathbf{AS}}{\text{minimize}} \frac{1}{2} \|\mathbf{X} - \mathbf{AS} - \mathbf{O}\|_2^2 + \alpha_1 \|(\mathbf{AS})\Phi\|_{2,1} + \alpha_2 \|\mathbf{O}\|_{2,1}.$$

 Unmix $(\mathbf{X} - \tilde{\mathbf{O}})$:

$$\tilde{\mathbf{S}}, \tilde{\mathbf{A}} = AMCA(\mathbf{X} - \tilde{\mathbf{O}})$$

return $\tilde{\mathbf{S}}, \tilde{\mathbf{A}}, \tilde{\mathbf{O}}$.

The separation between \mathbf{O} and \mathbf{AS} is carried out by a modified version of MCA which takes advantages of the difference of morphology between the two components. Besides, we propose to use the $\ell_{2,1}$ norm instead of ℓ_0 norm to exploit and

This work is supported by the European Community through the grants PhySIS (contract no. 640174) and DEDALE (contract no. 665044) within the H2020 Framework Program

preserve the structure of the two components (both composed of few active columns) over all the measurements.

Then, the algorithm AMCA [14] is used to unmix the sources from the outliers-free observations $\mathbf{X} - \mathbf{O}$. Indeed, in [11], it has been shown that AMCA is robust to the presence of the outliers. Hence, as the previous component separation done by $MCA_{\ell_{2,1}}$ may not be exact, it would be safer to use AMCA to obtain a robust estimate of \mathbf{A} rather than another outliers sensitive BSS method.

The major drawback of this algorithm, called robust multichannel MCA (rmMCA), is that the error done in the estimation of the outliers with $MCA_{\ell_{2,1}}$ is propagated in the estimations of \mathbf{A} , \mathbf{S} with AMCA. That is why, the returned tuple $(\tilde{\mathbf{S}}, \tilde{\mathbf{A}}, \tilde{\mathbf{O}})$ is only used as the starting point of the next step which estimates jointly \mathbf{A} , \mathbf{S} , and \mathbf{O} by minimizing eq.1.

2.2 Estimating jointly \mathbf{O} , \mathbf{S} and \mathbf{A}

In this step, we propose to estimate jointly \mathbf{O} , \mathbf{S} and \mathbf{A} by using proximal operators [15] and reweighted ℓ_1 [16], what has been shown to greatly improved the results obtained in sparse BSS in [17]. The reweighting procedure will be denoted as robust AMCA (rAMCA) in the following:

Joint Estimation: rAMCA

Input \mathbf{X}, Φ
 Initialization $\tilde{\mathbf{S}}, \tilde{\mathbf{A}}, \tilde{\mathbf{O}} = rmMCA(\mathbf{X}, \Phi)$
 Reestimate $\tilde{\mathbf{O}}$ and $\tilde{\mathbf{S}}$ given $\tilde{\mathbf{A}}$ with:

$$\operatorname{argmin}_{\mathbf{O}, \mathbf{S}} \frac{1}{2} \|\mathbf{X} - \tilde{\mathbf{A}}\mathbf{S} - \mathbf{O}\|_2^2 + \lambda \|\mathbf{S}\Phi\|_1 + \beta \|\mathbf{O}\|_{2,1}.$$

 Start the reweighting scheme:
for $k < K_{max}$ **do**
 Update the weights for the reweighted ℓ_1 : $\mathbf{W} = \frac{1}{\epsilon + |\tilde{\mathbf{S}}_{i,j}|}$
 while Do not converge **do**
 $\tilde{\mathbf{A}} = \operatorname{argmin}_{\mathbf{A}} \frac{1}{2} \|\mathbf{X} - \mathbf{A}\tilde{\mathbf{S}} - \tilde{\mathbf{O}}\|_2^2$
 $\tilde{\mathbf{S}} = \operatorname{argmin}_{\mathbf{S}} \frac{1}{2} \|\mathbf{X} - \tilde{\mathbf{A}}\mathbf{S} - \tilde{\mathbf{O}}\|_2^2 + \lambda \times \mathbf{W} \|\mathbf{S}\Phi\|_1$
 $\tilde{\mathbf{O}} = \operatorname{argmin}_{\mathbf{O}} \frac{1}{2} \|\mathbf{X} - \tilde{\mathbf{A}}\tilde{\mathbf{S}} - \mathbf{O}\|_2^2 + \beta \|\mathbf{O}\|_{2,1}$
 end while
end for
return $\tilde{\mathbf{S}}, \tilde{\mathbf{A}}, \tilde{\mathbf{O}}$.

Firstly, the sources and outliers are reestimated with the previous estimation of $\tilde{\mathbf{A}}$. This provides a better separation between the sources contribution and the outliers, what is necessary to start the following reweighted procedure in order to limit the propagation of errors. The reweighting procedure leads to a more accurate estimation of the sources, as it decreases the bias introduced by the ℓ_1 . Moreover, this also provides some robustness against local minima. The weights \mathbf{W} are updated once the convergence given the current weights has been reached [18].

3 Numerical experiments

In this section, we propose to compare the performances obtained by the minimization of the β -divergence [1], the combinations PCP+GMCA [3], MCA+GMCA [19], rmMCA, and the proposed procedure rAMCA. We consider that 8 sources have been mixed in 20 observations, in the presence of 5% of corrupted entries. Each source is a sum of sinusoids with varying frequencies of different amplitudes, and consequently, Φ is chosen to represent the DCT transform. The amplitudes of the entries of \mathbf{O} are generated from a centered Gaus-

sian law, whose standard deviation varies according to fig.1 (the averaged amplitude of \mathbf{S} in the direct domain is around 500). The means of the errors $\Delta_{\mathbf{S}} = 20 \log_{10} \left(\frac{\|\tilde{\mathbf{S}}\|_2}{\|\mathbf{S} - \tilde{\mathbf{S}}\|_2} \right)$ (expected for the minimization of the β -divergence which does not perform the separation of the components) and $\Delta_{\mathbf{A}} = \left\| \left(\tilde{\mathbf{A}}^T \tilde{\mathbf{A}} \right)^{-1} \tilde{\mathbf{A}}^T \mathbf{A} - \mathbf{I} \right\|_1$ over 16 runs are displayed.

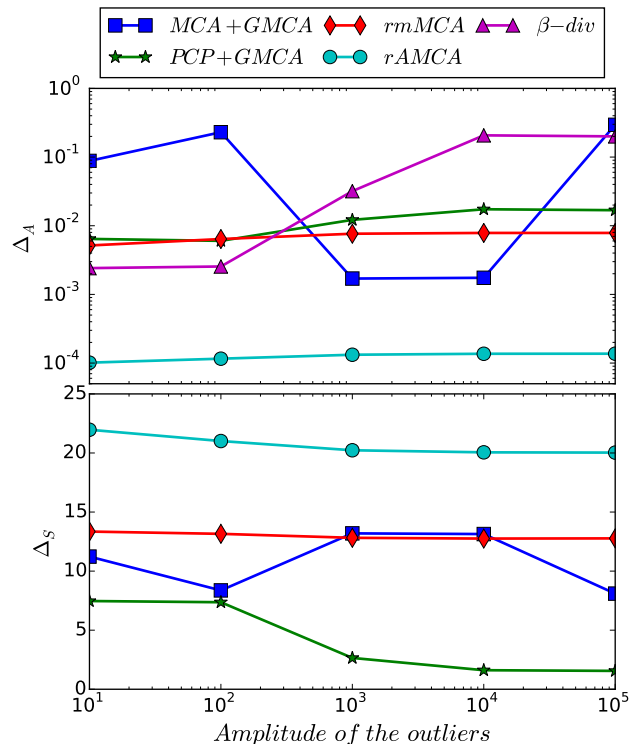


Figure 1: Influence of amplitude of the outliers

As it can be seen in fig.1, the combination rmMCA is indeed more robust than MCA+GMCA. This supports our proposition of using AMCA to overcome the fact that the data may not have been completely cleaned with MCA. Besides, only rmMCA and rAMCA are almost not influenced by the amplitude of the outliers, whereas the other methods are hampered by a large amplitude of \mathbf{O} . Last, the results reaches by rAMCA clearly outperforms, in term of robustness and accuracy, the other compared methods.

4 Conclusion and future works

We present a new sparse BSS method able to handle outliers whose morphology is different from the one of the sources. The preliminary numerical experiments show that this two-step procedure can indeed estimate reliably the sources, the outliers and the mixing matrix with a good accuracy. This supports the idea of not only using MCA to separate the components with different morphology but also a procedure taking into account the clustering structure of the observations. Future work will focus on developing and analyzing other approaches for the reweighting procedure. Indeed, finding the best strategy for the joint estimation is challenging and raises several issues such as robustness against local minima or convergence, as the problem is not convex.

References

- [1] M. Mihoko and S. Eguchi, "Robust blind source separation by beta divergence," *Neural computation*, vol. 14, no. 8, pp. 1859–1886, 2002.
- [2] P. Comon, "Independent component analysis, a new concept?" *Signal processing*, vol. 36, no. 3, pp. 287–314, 1994.
- [3] E. J. Candès, X. Li, Y. Ma, and J. Wright, "Robust principal component analysis?" *Journal of the ACM (JACM)*, vol. 58, no. 3, p. 11, 2011.
- [4] Q. Li, H. Li, Z. Lu, Q. Lu, and W. Li, "Denoising of hyperspectral images employing two-phase matrix decomposition," *Selected Topics in Applied Earth Observations and Remote Sensing, IEEE Journal of*, vol. 7, no. 9, pp. 3742–3754, Sept 2014.
- [5] H. Zhang, W. He, L. Zhang, H. Shen, and Q. Yuan, "Hyperspectral image restoration using low-rank matrix recovery," *Geoscience and Remote Sensing, IEEE Transactions on*, vol. 52, no. 8, pp. 4729–4743, Aug 2014.
- [6] L. Zhang, Z. Chen, M. Zheng, and X. He, "Robust non-negative matrix factorization," *Frontiers of Electrical and Electronic Engineering in China*, vol. 6, no. 2, pp. 192–200, 2011.
- [7] B. Shen, B. D. Liu, Q. Wang, and R. Ji, "Robust non-negative matrix factorization via ℓ_1 norm regularization by multiplicative updating rules," in *Image Processing (ICIP), 2014 IEEE International Conference on*, Oct 2014, pp. 5282–5286.
- [8] C. Févotte and N. Dobigeon, "Nonlinear Hyperspectral Unmixing With Robust Nonnegative Matrix Factorization," *IEEE Transactions on Image Processing*, vol. 24, no. 12, pp. 4810–4819, Dec 2015.
- [9] Y. Altmann, S. McLaughlin, and A. Hero, "Robust linear spectral unmixing using outlier detection," in *Acoustics, Speech and Signal Processing (ICASSP), 2015 IEEE International Conference on*. IEEE, 2015, pp. 2464–2468.
- [10] C. Chenot, J. Bobin, and J. Rapin, "Robust Sparse Blind Source Separation," *Signal Processing Letters, IEEE*, vol. 22, no. 11, pp. 2172–2176, 2015.
- [11] C. Chenot and J. Bobin, "Unsupervised separation of sparse sources in the presence of outliers," http://jbobin.cosmostat.org/Documents/rAMCA_Mar9.pdf, Technical report.
- [12] J. Bobin, F. Sureau, J.-L. Starck, A. Rassat, and P. Paykari, "Joint Planck and WMAP CMB map reconstruction," *A&A*, vol. 563, no. A105, 2014.
- [13] M. Elad, J.-L. Starck, P. Querre, and D. L. Donoho, "Simultaneous cartoon and texture image inpainting using morphological component analysis (MCA)," *Applied and Computational Harmonic Analysis*, vol. 19, no. 3, pp. 340–358, 2005.
- [14] J. Bobin, J. Rapin, A. Larue, and J.-L. Starck, "Sparsity and adaptivity for the blind separation of partially correlated sources," *Signal Processing, IEEE Transactions on*, vol. 63, no. 5, pp. 1199–1213, March 2015.
- [15] P. L. Combettes and V. R. Wajs, "Signal recovery by proximal forward-backward splitting," *Multiscale Modeling & Simulation*, vol. 4, no. 4, pp. 1168–1200, 2005.
- [16] E. J. Candes, M. B. Wakin, and S. P. Boyd, "Enhancing sparsity by reweighted ℓ_1 minimization," *Journal of Fourier analysis and applications*, vol. 14, no. 5-6, pp. 877–905, 2008.
- [17] J. Rapin, J. Bobin, A. Larue, and J.-L. Starck, "NMF with Sparse Regularizations in Transformed Domains," *SIAM Journal on Imaging Sciences*, vol. 7, no. 4, pp. 2020–2047, 2014.
- [18] P. Tseng, "Convergence of a block coordinate descent method for nondifferentiable minimization," *Journal of optimization theory and applications*, vol. 109, no. 3, pp. 475–494, 2001.
- [19] J. Bobin, J.-L. Starck, J. Fadili, and Y. Moudden, "Sparsity and morphological diversity in blind source separation," *Image Processing, IEEE Transactions on*, vol. 16, no. 11, pp. 2662–2674, 2007.

Randomness is sufficient ! Approximate recovery from CS samples

V. Abrol, P. Sharma and Anil K. Sao

SCEE, IIT Mandi, India

Abstract— In the framework of compressed sensing (CS), for recovery of the original signal, the sensing matrix must preserve the relative distances among the underlying sparse vectors. Provided this condition is fulfilled, we show that CS samples will also preserve the envelope of the actual signal. Exploiting the envelope preserving property of CS samples, we propose to extract prototype signals from compressive samples to obtain the sparse representation for approximate recovery of actual signals. These prototype signals are orthogonal intrinsic mode functions (IMFs) extracted using empirical mode decomposition (EMD). The dictionary is seeded using the extracted IMFs which are obtained without even comprehending the original signal or the sensing matrix. The efficiency of the proposed approach is demonstrated experimentally for the recovery of speech signals.

1 Introduction

Compressed sensing (CS) enables us to reconstruct a signal $\mathbf{x} \in \mathbb{R}^n$, which is assumed to be sparse in an overcomplete dictionary $\Psi \in \mathbb{R}^{n \times d}$ ($d=n$ for complete dictionary), via recovery of its sparse representation $\mathbf{a} \in \mathbb{R}^d$ from few measurements $\mathbf{y} \in \mathbb{R}^m$ sampled using a matrix $\Phi \in \mathbb{R}^{m \times n}$ with $m \ll n$ [1, 2, 3]. The estimation of sparse vector (or equivalently the original signal) using compressed samples is very much influenced by the choice of the dictionary [1, 4]. When only CS samples are available, recovering the signal while simultaneously learning the dictionary is a difficult task. Works in [5, 6, 7, 8], have proposed dictionary learning (DL) methods, from CS samples. However, such DL methods are computationally expensive, and for efficient sparse recovery rely on some assumptions e.g., knowledge of signal's support set [5].

As an alternative, we show that it is indeed possible to approximately recover a signal, by eliminating the abundant cost of learning a dictionary or recovering any irrelevant data. Moreover, this can be done without even comprehending the original signal or the sensing matrix used to acquire the signal. The proposed approach exploits the fact that though random, CS samples still approximately preserve important signal properties [1]. For instance in [9], it was shown that principal component analysis (PCA) on low-dimensional random projections is as good as performing PCA on the original data. This was supported by our observation that for many types of signals, CS samples indeed preserves its envelope. Exploiting the envelope preserving property of CS measurements, we propose a novel optimization free method, where the aim is to express a signal as a sparse linear combination of prototype signals extracted from CS samples. These prototype signals, can be intrinsic mode functions (IMFs) extracted using empirical mode decomposition (EMD), which is one of the popular methods to capture the envelope of a signal [10]. We show that the IMFs extracted from compressed signal show similar characteristics to the ones extracted from the signal itself. Hence, the extracted IMFs can be used to seed a dictionary, using which one can re-

cover the original signal from CS samples.

Authors would like to emphasize that the goal of the paper is not to outperform a state-of-the-art CS recovery method, but is to propose an approach which can perform with an acceptable level of accuracy in heavily resource-constrained environments, both in terms of storage and computation. To the best of our knowledge, none of the previous papers have proposed such methods for compressively sensed signals.

2 Modeling Signals using CS

In CS framework, given a matrix $\mathbf{Y} \in \mathbb{R}^{m \times l}$ consisting of l compressive signals $\{\mathbf{y}_i\}_{i=1}^l$ as columns, the recovery of the corresponding signal set $\mathbf{X} \in \mathbb{R}^{n \times l}$ is formulated as [11, 12]:

$$\hat{\mathbf{X}} \approx \Psi \hat{\mathbf{A}} \quad \text{where } \hat{\mathbf{A}} \text{ is computed as,}$$

$$\hat{\mathbf{A}} = \underset{\mathbf{A}}{\operatorname{argmin}} f(\mathbf{A}) \quad \text{s.t. } \|\mathbf{Y} - \Phi \Psi \mathbf{A}\|_F^2 = \|\mathbf{Y} - \mathbf{D}\mathbf{A}\|_F^2 < \epsilon \quad (1)$$

Here, $\mathbf{A} \in \mathbb{R}^{d \times l}$ is the sparse coefficient matrix corresponding to \mathbf{X} , ϵ is the error tolerance, $f(\cdot)$ is a function (e.g., l_1 -norm) that promotes sparsity and $\mathbf{D} \in \mathbb{R}^{m \times d}$ is the overall effective dictionary. Provided Φ satisfies restricted isometry property (RIP), and is incoherent with Ψ , (1) can be solved by linear programming methods [1].

2.1 Randomness Do Make Sense: Properties of Compressive Samples

CS acquires random signal measurements¹ and hence do not preserve any structures in their raw form. However, random projections approximately preserves the properties such as sample mean, variance, as well as the relative distance between sparse vectors of two signals [1, 9], i.e.,

$$\|\mathbf{D}(\mathbf{a}_1 - \mathbf{a}_2)\|_2^2 \approx \|\mathbf{a}_1 - \mathbf{a}_2\|_2^2 \forall \mathbf{a}_1, \mathbf{a}_2 \in \mathbb{R}^d$$

$$\hat{\Sigma} = \mathbf{Y}\mathbf{Y}^T = \Phi \mathbf{X}\mathbf{X}^T \Phi^T = \Phi \Sigma \Phi^T \quad \text{and} \quad \mathbf{E}[\|\Phi \mathbf{x}\|_2^2] = \|\mathbf{x}\|_2^2 \quad (2)$$

As an illustration, Figure 1, shows a example of the original and compressively sensed speech signal. Note that the sampling rate of a compressed signal is less than that of the original signal, and for a fair comparison, the interpolated compressed signal, computed using cosine interpolation is plotted in the figure. It can be observed that though the measurement vector exhibits some random noise-like nature, envelopes² of both the original and the compressive speech signal are approximately similar, even at different compression ratios.

3 Proposed Method

The proposed CS-EMD approach sparsely represents a signal as a linear combination of few IMFs from the dictionary. However, the IMFs used to build the dictionary are extracted directly

¹The elements of Φ are assumed to be i.i.d. random variables

²With a slight abuse of definition, envelope here denotes evolution of signal over time/samples

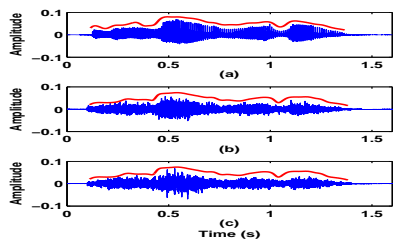


Figure 1: Comparison of the envelopes (manually marked red) of (a) original speech signal, (b) and (c) interpolated compressive speech signal originally sampled at compression ratio (m/n) of 0.6 and 0.4 respectively.

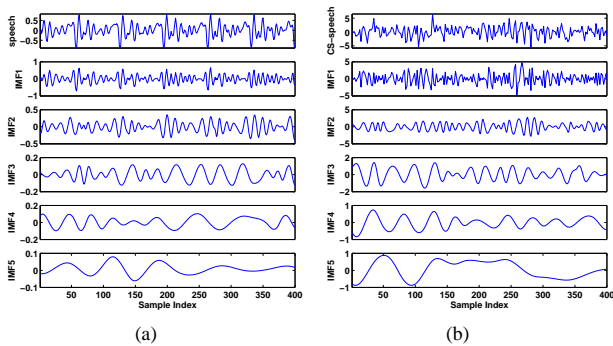


Figure 2: EMD decomposition of a voiced frame of (a) original speech signal and (b) interpolated compressive speech signal

from CS samples. Using EMD, a given compressed signal y is expressed as

$$y = \sum_{q=1}^J \mathbf{m}_q + \mathbf{r} \quad (3)$$

i.e., a sum of J orthogonal modes $\mathbf{m}_q \in \mathbb{R}^m$ and a residual $\mathbf{r} \in \mathbb{R}^m$ [10]. Since CS vector will have low dimensionality, for efficient decomposition, we used the raised cosine EEMD method [13] (with roll-off factor $\beta = 1$) on interpolated CS vector to extract IMFs of appropriate dimensions. One can observe that most of the IMFs extracted using CS samples (Figure 2 (b)) show similar characteristics as in case of the IMFs extracted using raw speech samples (Figure 2 (a)). The main advantage of this method is in its time complexity, which follows from the fact that extracting IMFs do not require the sensing matrix to be known. This motivated us to use these IMFs directly as dictionary atoms. Further, the extracted IMFs being orthogonal leads to low coherence among atoms. Each level of EMD decomposition has different structural information, and to restrict the atoms to a desired number, the extracted IMFs from the J^{th} level across all training signals are clustered using K-means algorithm and the cluster centers are used as dictionary atoms. To have a sparser representation, more atoms should come from initial levels which are more informative.

3.0.1 Computational Complexity

The time complexity of EMD for extracting all IMFs from L n -dimensional signal frames approximately scales to $\mathcal{O}(nL \log n)$, that is equal to that of Fast Fourier transform. Thus, the overall complexity of the proposed non-iterative approach (including clustering) is less as compared to conventional DL methods, for which the time complexity per iteration scales to $\mathcal{O}(n^2L)$, or in some cases to $\mathcal{O}(n^3L)$ [14].

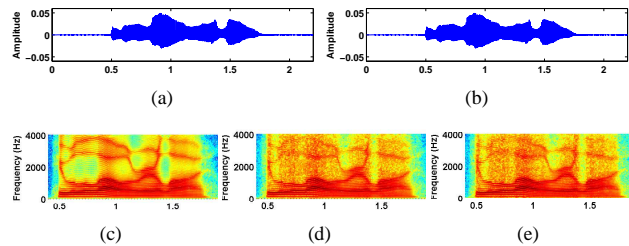


Figure 3: (a) Original speech signal, (b) Recovered speech signal at compression ratio of 0.4. Spectrogram plot of (c) original speech signal, (b) and (c) recovered speech signal at compression ratio of 0.4 and 0.6 respectively.

Table 1: Comparative Analysis of Different Methods for Signal Recovery averaged for 20 utterances over 10 trials.

Method	CS Matrix $m/n = 0.4$	DL Iterations	PESQ	Runtime
Proposed	Sparse-Gaussian	N.A	2.91	0.83 min
	SRM [18]		2.90	
	Gaussian		2.89	
	Bernoulli		2.83	
CS+DCT	Gaussian	N.A	2.30	0.3 min
Blind CS [7]	Gaussian	20	2.96	5 min
IHT [8]	Gaussian	20	3.01	3 min

4 Experimental Results

Our experiments are done using speech signals (sampled at 8 kHz) taken from KED TIMIT corpus [15]. Speech is processed over short time frames, where framing is done using a 50 ms long Hanning window with 50% overlap. The number of dictionary atoms to be learned is set to 600. The number of IMFs extracted using EEMD (with 50 different noise realizations) for each compressive speech frame is set to 5. The number of dictionary atoms chosen empirically from each IMF level across all training frames after clustering are 140, 140, 110, 110, and 100 respectively. The dictionary is then used to solve (1) using YALL1 package [16], and the speech utterance was reconstructed using the standard overlap and add method.

Figure 3 shows an example of the original and the recovered speech waveform, along with their respective spectrogram plots. Further, Table 1 shows the perceptual evaluation of speech quality (PESQ) scores [17], for the recovered speech using different methods. It can be observed that the proposed method is able to recover the speech signal well. Table 1 also show the average CPU run times to recover a speech utterance of approximately 3 sec (including the time for DL), and the results confirms that the proposed approach is indeed fast compared to existing approaches.

Our experiments shows that one can approximately recover a signal directly from its CS samples, provided they preserve envelope of the signal. The choice of sensing matrix is crucial and if a sensing matrix is carefully chosen or designed one can improve the performance of the proposed approach by learning a better dictionary. Further, the extracted IMFs can reveal important properties about signal segments without the requirement of sensing matrix used to acquire the signal. For instance, this has promising applications in various inference problems where actual signal recovery is not required, and only CS samples (which require less memory) are available e.g., voiced/nonvoiced speech detection [19].

References

- [1] D. L. Donoho, "Compressed sensing," *IEEE Transactions on Information Theory*, vol. 52, no. 4, pp. 1289–1306, April 2006.
- [2] I. Tasic and P. Frossard, "Dictionary learning," *IEEE Signal Processing Magazine*, vol. 28, no. 2, pp. 27–38, March 2011.
- [3] P. Sharma, V. Abrol, and A. K. Sao, "Compressed sensing for unit selection based speech synthesis system.," in *European Signal Processing Conference (EUSIPCO)*, August 2015.
- [4] P. Sharma, V. Abrol, A. D Dileep, and A. K. Sao, "Sparse coding based features for speech units classification," in *16th INTERSPEECH*. September 2015, ISCA.
- [5] C. Studer and R. G. Baraniuk, "Dictionary learning from sparsely corrupted or compressed signals," in *IEEE International Conference on Acoustics, Speech and Signal Processing (ICASSP)*, March 2012, pp. 3341–3344.
- [6] F. Pourkamali Anaraki and S. M. Hughes, "Compressive K-SVD," in *IEEE International Conference on Acoustics, Speech and Signal Processing (ICASSP)*, May 2013, pp. 5469–5473.
- [7] S. Gleichman and Y.C. Eldar, "Blind compressed sensing," *IEEE Transactions on Information Theory*, vol. 57, no. 10, pp. 6958–6975, October 2011.
- [8] Ch. Srikanth Raj and T. V. Sreenivas, "Time-varying signal adaptive transform and IHT recovery of compressive sensed speech," in *12th INTERSPEECH*, August 2011, pp. 73–76.
- [9] J. E. Fowler, "Compressive-projection principal component analysis," *IEEE Transactions on Image Processing*, vol. 18, no. 10, pp. 2230–2242, October 2009.
- [10] A. Bouzid and N. Ellouze, "Empirical mode decomposition of voiced speech signal," in *First International Symposium on Control, Communications and Signal Processing (ISCCSP)*, March 2004, pp. 603–606.
- [11] E. J. Candés and M. B. Wakin, "An introduction to compressive sampling," *IEEE Signal Processing Magazine*, vol. 25, no. 2, pp. 21–30, March 2008.
- [12] V. Abrol, P. Sharma, and A. K. Sao, "Speech enhancement using compressed sensing," in *14th INTERSPEECH*. September 2013, pp. 3274–3278, ISCA.
- [13] A. Roy and J.F. Doherty, "Raised cosine filter-based empirical mode decomposition," *IET Signal Processing*, vol. 5, no. 2, pp. 121–129, April 2011.
- [14] Michael Elad, *Sparse and Redundant Representations - From Theory to Applications in Signal and Image Processing*, Springer, 2010.
- [15] "University of Edinburgh's KED TIMIT," <http://festvox.org/>.
- [16] J. Yang Y. Zhang and W. Yin, "YALL1: Your algorithms for l1," <http://www.yall1.blogs.rice.edu>, 2011.
- [17] A. Benyassine, E. Shlomot, Su Huan-yu, D. Massaloux, C. Lamblin, and J. P. Petit, "ITU-T recommendation G.729 Annex B: a silence compression scheme for use with G.729 optimized for V.70 digital simultaneous voice and data applications," *IEEE Communications Magazine*, vol. 35, no. 9, pp. 64–73, August 1997.
- [18] T.T. Do, Lu Gan, N.H. Nguyen, and T.D. Tran, "Fast and efficient compressive sensing using structurally random matrices," *IEEE Transactions on Signal Processing*, vol. 60, no. 1, pp. 139–154, Jan 2012.
- [19] V. Abrol, P. Sharma, and A. K. Sao, "Voiced/nonvoiced detection in compressively sensed speech signals," *Speech Communication*, vol. 72, no. 0, pp. 194 – 207, 2015.

The Effect of Atom Replacement Strategies on Dictionary Learning

Paul Irofti¹.

¹ University Politehnica of Bucharest, Romania.

Abstract— The sparse representations field presents a wide set of algorithms for learning overcomplete dictionaries. During the learning process many of the dictionary columns remain unused by the resulting representations. In this paper we present a few replacement strategies and their direct impact on a set of popular algorithms such as K-SVD. Experiments show significant reductions in the representation error and also evidentiate clear differences between the strategies.

1 Introduction

The signal processing domain presents an increased interest for sparse representations through overcomplete dictionary learning (DL)[1, 2], which showed significant improvements compared to fixed dictionaries built from various transform basis.

Starting with the matrix $Y \in \mathbb{R}^{p \times m}$, built from m training signals of dimension p , and a sparsity target s we aim to solve the optimization problem

$$\begin{aligned} & \underset{D, X}{\text{minimize}} && \|Y - DX\|_F^2 \\ & \text{subject to} && \|d_j\|_2 = 1, 1 \leq j \leq n \\ & && \|x_i\|_0 \leq s, 1 \leq i \leq m, \end{aligned} \quad (1)$$

where the variables are the dictionary $D \in \mathbb{R}^{p \times n}$, whose n columns d_j are called atoms, and the sparse representations $X \in \mathbb{R}^{n \times m}$. The columns x_i of X are at most s -sparse as denoted by $\|\cdot\|_0$ which is the l_0 pseudo-norm. The atoms are normalized so that the multiplicative indeterminateness of the DX factorization is removed.

Equation (1) is non-convex and bilinear which is why DL methods approach it in two stages. First, the dictionary D is fixed and the representations are computed. This is a hard combinatorial problem that can be solved through greedy algorithms. The popular choice is orthogonal matching pursuit (OMP)[3]. Next, the resulting representations are kept fixed and the dictionary is updated to reduce the approximation error.

Investigating the sparsity pattern provided by OMP we can see how many times each dictionary atom is used for representation. While popular atoms help with classification and compression, what about the ones that are rarely or never used?

In this paper we focus on different strategies for replacing unused atoms with new ones leading to an overall improvement of the DL process. In Section 2 we briefly present existing dictionary update methods followed by Section 3, where we describe and present numerical results with different replacement strategies, and afterwards we conclude in Section 4.

2 DL algorithms

K-SVD[4] updates the atoms in sequence following the Gauss-Seidel approach: the current atom is refined using informa-

tion from the atoms that were previously updated in the current stage. K-SVD solves the optimization problem

$$\min_{d_j, X_{j, \mathcal{I}_j}} \left\| \left(Y - \sum_{\ell \neq j} d_\ell X_{\ell, \mathcal{I}_\ell} \right) - d_j X_{j, \mathcal{I}_j} \right\|_F^2, \quad (2)$$

where \mathcal{I}_j is the sparse signals subset that use atom j in their representation, X_{j, \mathcal{I}_j} denotes row j from the sparse representations restricted to the columns in \mathcal{I}_j , and all atoms excepting d_j are fixed. Problem (2) is a rank-1 approximation whose solution is given by the singular vectors corresponding to the largest singular value. Note that the solution updates both the atom and the associated representations.

Approximate K-SVD (AK-SVD)[5] is a faster version that computes the singular vectors through a single iteration of the power method

In order to guarantee certain properties, such as clustering, sequential generalization of K-means (SGK) [6] preserves the sparse structure and proposes a similar optimization problem that refines only the atom d_j . This can be reduced to a simple least-squares problem.

NSGK [7] follows the same strategy, but accounts for differences between the previous and current values of the dictionary and representations. Empirical evidence indicates that NSGK provides better results than the former methods.

3 Replacement Strategies

The sequential nature of the dictionary update allows us to replace unused atoms during refinement as soon as we encounter them.

Let us assume that the default action is to leave the atom as it is. Numerical evidence shows that once an atom stops being used it never gets picked up again, so we could just remove it and shrink the dictionary. While this does not affect the approximation it does improve performance and storage.

Given that common practice dictates that we start with a random dictionary, a natural idea is to substitute with a new randomly generated column. Another option is to find the worst represented signal and make it a part of the dictionary (marked 'Worst' in our tables and figures). In our experiments we also performed this replacement in bulk at the end of the dictionary refinement stage. We label this 'Post'.

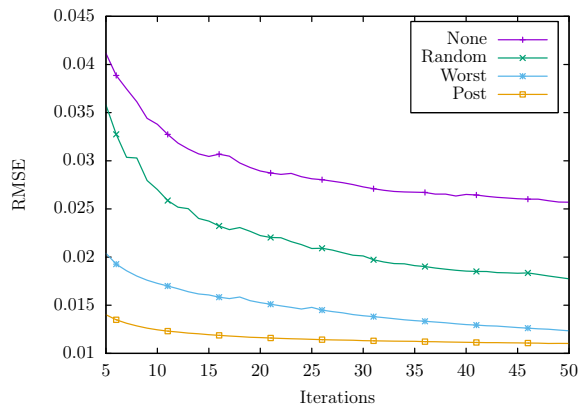
We built the signal set Y from random 8×8 image patches taken from the USC-SIPI [8] database. The results presented here are the average of executing 10 runs of each method with the same parametrization. Every algorithm performed 50 DL iterations before stopping.

We compare the approximation of the original signals by the dictionary and sparse representations through the root mean square error $\text{RMSE} = \frac{\|Y - DX\|_F}{\sqrt{pm}}$.

In Table 1 we show the DL results on a set of $m = 2048$ signals of size $p = 64$ each, with a sparsity constraint $s = 8$,

Table 1: Final RMSE with various replacement strategies

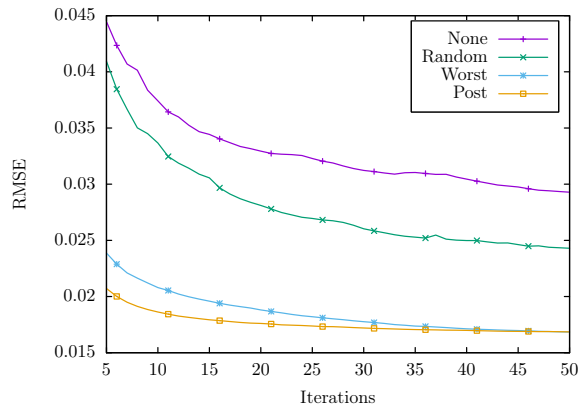
n	Method	Replacement			
		None	Random	Worst	Post
128	K-SVD	0.029406	0.026723	0.019096	0.019355
	AK-SVD	0.029497	0.026876	0.019134	0.019369
	SGK	0.029402	0.026800	0.019079	0.019612
	NSGK	0.025004	0.024707	0.020558	0.019804
192	K-SVD	0.030805	0.027013	0.018812	0.018803
	AK-SVD	0.031010	0.026661	0.018804	0.018835
	SGK	0.031328	0.026938	0.018799	0.018885
	NSGK	0.023911	0.025168	0.021471	0.019271
256	K-SVD	0.029146	0.023979	0.016773	0.016730
	AK-SVD	0.029291	0.024300	0.016843	0.016858
	SGK	0.029836	0.024201	0.016928	0.016923
	NSGK	0.022099	0.022590	0.020913	0.017563
384	K-SVD	0.024984	0.018467	0.012522	0.011930
	AK-SVD	0.024721	0.018697	0.012665	0.011972
	SGK	0.024693	0.019048	0.012791	0.011946
	NSGK	0.016995	0.016820	0.018473	0.012650
512	K-SVD	0.025699	0.017744	0.012343	0.011034
	AK-SVD	0.025318	0.018016	0.012436	0.011078
	SGK	0.025617	0.017668	0.012579	0.011072
	NSGK	0.016795	0.016769	0.017951	0.012128

Figure 1: Error descent averaged over 10 runs for K-SVD ($n = 512$).

while varying the dictionary size. We can see that, except for a few NSGK results, replacing the unused atoms provides much better approximations. While using random atoms for substitution improves the situation, choosing the worst represented data item instead is clearly the best choice. The difference comes with dictionary size: smaller dictionaries prefer substitution during refinement ($n = 128$ and part of $n = 256$), while larger ones show smaller errors by replacing all unused atoms post-refinement.

Figure 1 shows the average error evolution of K-SVD with different atom replacement strategies. Employing post-refinement substitution is the clear winner at every iteration, followed by performing signal substitution during dictionary update. Random replacement comes in last, but is clearly ahead of the plain K-SVD version.

In Figure 2 we present the average error curve for AK-SVD dictionaries of size $n = 256$. This case is particularly interesting because post-refinement substitution starts ahead but is caught up and beaten by substitution during dictionary update. Even though both are well behind, we can see that random re-

Figure 2: Error descent averaged over 10 runs for AK-SVD ($n = 256$).

placement is better than no replacement.

4 Conclusion

We presented the impact of different atom replacement techniques on the DL process. Numerical results have shown, with small exceptions, that substitution has a significant impact on the approximation error. Our experiments suggest that replacing unused atoms with the worst represented signals from the training set is the best approach.

Acknowledgements

This work was supported by the Romanian National Authority for Scientific Research, CNCS - UEFISCDI, project number PN-II-RU-TE-2014-4-2713.

References

- [1] R. Rubinstein, A.M. Bruckstein, and M. Elad, "Dictionaries for Sparse Representations Modeling," *Proc. IEEE*, vol. 98, no. 6, pp. 1045–1057, June 2010.
- [2] I. Tomic and P. Frossard, "Dictionary Learning," *IEEE Signal Proc. Mag.*, vol. 28, no. 2, pp. 27–38, Mar. 2011.
- [3] Y.C. Pati, R. Rezaifar, and P.S. Krishnaprasad, "Orthogonal matching pursuit: Recursive function approximation with applications to wavelet decomposition," in *27th Asilomar Conf. Signals Systems Computers*, Nov. 1993, vol. 1, pp. 40–44.
- [4] M. Aharon, M. Elad, and A.M. Bruckstein, "K-SVD: An Algorithm for Designing Overcomplete Dictionaries for Sparse Representation," *Signal Processing, IEEE Transactions on*, vol. 54, no. 11, pp. 4311–4322, 2006.
- [5] R. Rubinstein, M. Zibulevsky, and M. Elad, "Efficient Implementation of the K-SVD Algorithm using Batch Orthogonal Matching Pursuit," *Technical Report - CS Technion*, 2008.
- [6] S.K. Sahoo and A. Makur, "Dictionary training for sparse representation as generalization of k-means clustering," *Signal Processing Letters, IEEE*, vol. 20, no. 6, pp. 587–590, 2013.
- [7] M. Sadeghi, M. Babaie-Zadeh, and C. Jutten, "Dictionary Learning for Sparse Representation: a Novel Approach," *IEEE Signal Proc. Letter*, vol. 20, no. 12, pp. 1195–1198, Dec. 2013.
- [8] A.G. Weber, "The USC-SIPI Image Database," 1997.

Blind Deconvolution of PET Images using Anatomical Priors

Stéphanie Guérit^{1,*}, Adriana González^{1,*}, Anne Bol², John A. Lee^{1,2,†} and Laurent Jacques^{1,†}

¹ICTEAM/ELEN, ISPGROUP, UCL, Belgium. ²MIRO/IREC, UCL, Belgium.

Abstract – Images from positron emission tomography (PET) provide metabolic information about the human body. They present, however, a spatial resolution that is limited by physical and instrumental factors often modeled by a blurring function. Since this function is typically unknown, blind deconvolution (BD) techniques are needed in order to produce a useful restored PET image. In this work, we propose a general BD technique that restores a low resolution blurry image using information from data acquired with a high resolution modality (e.g., CT-based delineation of regions with uniform activity in PET images). The proposed BD method is validated on synthetic and actual phantoms.

1 Introduction

Positron emission tomography (PET) is a powerful functional imaging technique. Often combined with anatomical computed tomography (CT) images, it provides physicians with relevant information for patient management [1]. For instance, a radioactive analogue of glucose, the ¹⁸F-fluorodeoxyglucose (¹⁸FDG), is injected in the patient's body and accumulates mainly in tissues of abnormally high metabolic activity. Emitted positrons are subsequently detected by the PET imaging system via anti-collinear annihilation photons.

Motivation. PET data suffer from two drawbacks restricting their direct use: (i) low spatial resolution and (ii) high level of noise. Both physical and instrumental factors limit the spatial resolution [1]. They are commonly represented as a blurring function that is estimated by imaging a radioactive point source. The resulting blur is usually approximated by a Gaussian point spread function (PSF) [1]. Noise, which is Poissonian in the raw data, is due to low photon detection efficiency of the detectors and to the limited injected tracer dose.

Improving the quality of PET images is a key element for better medical interpretation. Post-reconstruction restoration techniques are more adapted to clinical use since only reconstructed images are generally available. Nowadays, existing approaches are dedicated to denoising, deblurring, or combining both steps [2, 3, 4, 5]. Most of the approaches that include deblurring use an empirically estimated PSF.

Since the design of PET scanners can vary greatly between manufacturers and models, their imaging properties (e.g., their PSF) are different. Restoration of images acquired in the context of a multicentric study (with centralization of the reconstructed data) is then challenging: the raw data are not always accessible and the PSF cannot be directly measured. This context motivates the development of *blind* deconvolution (BD) techniques to jointly estimate the PSF and the PET image.

Contributions. Anatomical information can be useful to regularize such an ill-posed inverse problem [4]. Due to its perfect dilution in the kidneys, ¹⁸FDG accumulates uniformly in the patient bladder with a high concentration (see Fig. 1) [1]. An

accurate delineation of this organ is obtained from high resolution CT images. This provides a strong prior information that can be used to regularize the inverse problem: inside this region, the intensity of the restored image must be constant (i.e., the gradient is zero). In this work, we propose a method using this prior to regularize the BD inverse problem. A similar prior is used in [6] for BD of astronomical images with a celestial transit. Any PSF is directly inferred from the observations without assuming a parametric model. We only assume that the PSF (i) preserves the photon counts, (ii) is non-negative and (iii) is spatially invariant over the whole field-of-view (FOV).

2 Problem Statement

Let $\mathbf{x} \in \mathbb{R}^N$ be the original PET image defined in a $n \times n$ grid of $N = n^2$ pixels. Since the PSF is assumed to be uniform, the observed PET image $\mathbf{y} \in \mathbb{R}^N$ can be modeled as a linear convolution of \mathbf{x} with a function $\mathbf{h} \in \mathbb{R}^N$, the discrete equivalent of the PSF. If we assume that the acquisition time is long enough to have a high photon counts, the Poisson noise intrinsic to the PET imaging process can be approximated as an additive, white and Gaussian noise (AWGN) $\boldsymbol{\eta} \in \mathbb{R}^N$, with $\eta_i \sim_{\text{i.i.d.}} \mathcal{N}(0, \sigma_n^2)$. The acquisition process is thus modeled as follows:

$$\mathbf{y} = \mathbf{h} \otimes \mathbf{x} + \boldsymbol{\eta}, \quad (1)$$

where $\|\boldsymbol{\eta}\|_2^2 < \varepsilon^2 := \sigma_n^2(N + c\sqrt{N})$ with high probability for $c = \mathcal{O}(1)$ [7]. Noise variance σ_n^2 can be estimated using a robust median estimator [8].

3 Blind Deconvolution

In this work, we aim at reconstructing both \mathbf{x} and \mathbf{h} from the noisy observations \mathbf{y} . Since the data are assumed to be corrupted by AWGN, we adopt a data fidelity term based on the ℓ_2 -norm of the residual vector, i.e., $\|\mathbf{y} - \mathbf{h} \otimes \mathbf{x}\|_2$.

If we formulate the BD as a least-squares problem that minimizes the energy of the residual vector, we have an ill-posed problem since an infinite number of solutions can produce the observations \mathbf{y} . The problem needs to be regularized by enforcing prior knowledge about the PSF and the image, avoiding in this way the trivial solution.

We use an anatomical prior where the image is assumed to be constant inside set Ω containing the pixels that represent the patient's bladder. This means that the image gradi-

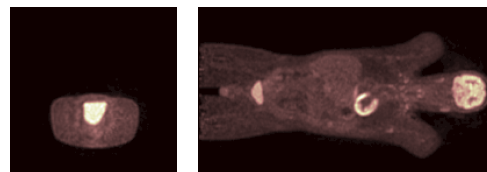


Figure 1: Transaxial (left) and coronal (right) PET images of a patient. Activity in the bladder is high and uniform. Source: Cliniques universitaires Saint-Luc.

*These authors contributed equally.

†Research Associates with the Belgian F.R.S.-FNRS.

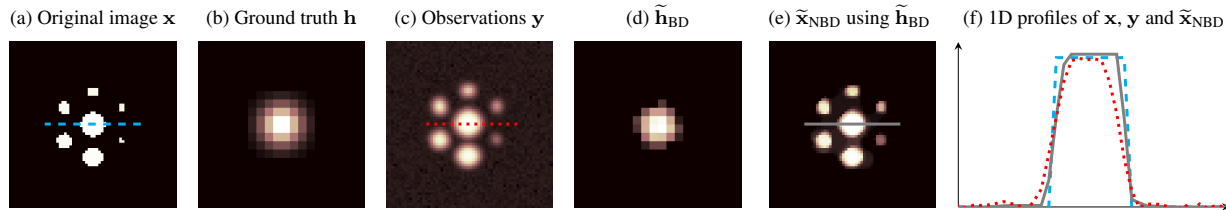


Figure 2: Results on synthetic phantom data (BSNR = 30 dB). The original, observed and estimated images present a horizontal line at $n/2 + 1 = 33$. This corresponds to the profiles shown in Figure 2f, with \mathbf{x} in dashed cyan, \mathbf{y} in dotted red and $\tilde{\mathbf{x}}_{\text{NBD}}$ in solid gray.

ent belongs to the set of pixels with zero intensity in Ω as $\mathcal{G} = \{\mathbf{u} \in \mathbb{R}^{2N} | u_i = 0, \forall i \in \Omega\}$.

As commonly done in the literature [4, 9, 10], we assume that images analyzed in this work are composed by slowly varying areas separated by sharp boundaries corresponding to tissue interfaces. Therefore, the inverse problem can be further regularized by promoting small Total-Variation norm (denoted $\|\mathbf{u}\|_{\text{TV}}$), which corresponds to the ℓ_1 -norm of the magnitude of the gradient of $\mathbf{u} \in \mathbb{R}^N$ [10].

The physics of PET imaging suggests three additional constraints to model (1): (i) image *non-negativity*, i.e., $\mathbf{x} \in \mathcal{P} = \{\mathbf{u} \in \mathbb{R}^N | \mathbf{u} \geq \mathbf{0}\}$, since the original image \mathbf{x} represents non-negative metabolic activity; (ii) *photometry invariance*, i.e., $\sum_{i=1}^N x_i \approx \sum_{i=1}^N y_i$; (iii) *PSF non-negativity*, since the PSF is an observation of a point. From (ii) and (iii) we know that the PSF must belong to the probability simplex [11], defined as $\mathcal{PS} = \{\mathbf{h} \in \mathbb{R}^N | \mathbf{h} \geq \mathbf{0}, \|\mathbf{h}\|_1 = 1\}$.

Gathering all these aspects, we propose the following regularized BD formulation:

$$\{\tilde{\mathbf{x}}_{\text{B}}, \tilde{\mathbf{h}}_{\text{B}}\} = \arg \min_{\tilde{\mathbf{x}}, \tilde{\mathbf{h}}} \{L(\tilde{\mathbf{x}}, \tilde{\mathbf{h}}) := \rho \|\tilde{\mathbf{x}}\|_{\text{TV}} + \frac{1}{2} \|\mathbf{y} - \tilde{\mathbf{h}} \otimes \tilde{\mathbf{x}}\|_2^2 + \iota_{\mathcal{P}}(\tilde{\mathbf{x}}) + \iota_{\mathcal{G}}(\nabla \tilde{\mathbf{x}}) + \iota_{\mathcal{PS}}(\tilde{\mathbf{h}})\}, \quad (2)$$

with $\tilde{\mathbf{x}}, \tilde{\mathbf{h}} \in \mathbb{R}^N$, $L(\tilde{\mathbf{x}}, \tilde{\mathbf{h}})$ the objective function and $\nabla: \mathbb{R}^N \rightarrow \mathbb{R}^{2N}$ the gradient operator [12]. The function $\iota_{\mathcal{C}}(\mathbf{u})$ denotes the convex indicator function on the set $\mathcal{C} \in \{\mathcal{P}, \mathcal{G}, \mathcal{PS}\}$, which is equal to 0 if $\mathbf{u} \in \mathcal{C}$ and $+\infty$ otherwise. Regularization parameter ρ , unknown *a priori*, controls the trade-off between sparsity of the image gradient magnitude and fidelity to the observations. In this work, we estimate ρ iteratively based on [6], with an initial value given by $\sigma\sqrt{2\log N}$ [8]. Non-convex problem (2) is solved by means of the proximal alternating minimization proposed in [13].

Once the PSF has been estimated using the BD scheme (2), image $\tilde{\mathbf{x}}_{\text{NBD}}$ can be estimated using a non-blind deconvolution (NBD) scheme that does not take into account the anatomical

prior. The NBD formulation is solved for an observation \mathbf{y} that has not been used in (2) for the PSF estimation.

4 Results and discussion

Method. The synthetic image used for first validation of the method (see Fig. 2a) is similar to the image obtained from a phantom with cylindrical holes of known diameters filled with the same ^{18}F FDG activity concentration (1 mCi/100 mL). The discrete PSF is simulated by an isotropic Gaussian kernel with $\sigma = 1.3$ pixels (see Fig. 2b), i.e., a PSF similar to those empirically estimated. The measurements are generated according to (1) (see Fig. 2c). Noise variance σ_n^2 is chosen such that the blurred signal-to-noise ratio (SNR) defined as $\text{BSNR} = 10 \log_{10} \text{var}(\mathbf{h} \otimes \mathbf{x}) / \sigma_n^2$ is in $\{10, 20, 30, 40\}$ dB. Quality of $\tilde{\mathbf{x}}$ and $\tilde{\mathbf{h}}$ is measured with the increase in SNR (ISNR) and the reconstruction SNR (RSNR), respectively [6].

Real images were acquired on a Philips GEMINI-TF PET/CT scanner with an acquisition time of 15 min (see Fig. 3a). The pixel size in transaxial slices is $2 \times 2 \text{ mm}^2$. For comparison, we made a Gaussian approximation of the PSF ($\tilde{\mathbf{h}}_{\text{Gaussian}}$, see Fig. 3b) by imaging a needle filled with ^{18}F FDG (3 mCi/mL). This PSF was used in the NBD scheme to deconvolve \mathbf{y} , resulting in $\tilde{\mathbf{x}}_{\text{Gaussian}}$ (see Fig. 3c).

Image size is 64×64 pixels ($N = 64^2$). For restoration, we consider that region Ω is composed of the five largest disks in the phantom mask, delineated thanks to the CT image (see Fig. 3d).

Results. Table 1 presents the reconstruction results using the BD scheme for the considered levels of noise. They correspond to the average value over 10 trials. The results for BSNR = 30 dB are depicted in Figs. 2d-2f. In terms of RSNR and visual observation, $\tilde{\mathbf{h}}_{\text{BD}}$ is close to the ground truth for different noise levels. When $\tilde{\mathbf{h}}_{\text{BD}}$ is used for the NBD, $\tilde{\mathbf{x}}_{\text{NBD}}$ presents, as expected, a constant intensity in region Ω .

BSNR [dB]	RSNR($\tilde{\mathbf{h}}_{\text{BD}}$) [dB]	ISNR($\tilde{\mathbf{x}}_{\text{BD}}$) [dB]
40	19.47	11.38
30	16.34	10.18
20	12.60	7.82
10	6.20	4.71

Table 1: BD results for synthetic phantom data and for different levels of noise.

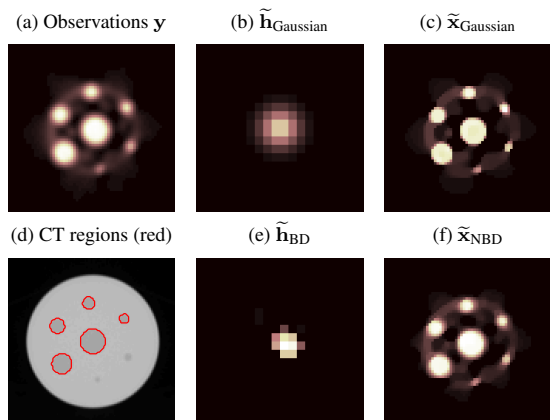


Figure 3: Results on real phantom data.

Figure 3 presents the results on real phantom data. The PSF $\tilde{\mathbf{h}}_{\text{BD}}$ is well-localized. Quality of the resulting NBD image is not as satisfactory as expected due to reconstruction artifacts.

Perspectives. In further research, we would like to improve: (i) the forward model by considering the whole 3D image as well as Poisson noise statistics and (ii) the assumptions and priors on the PSF by considering its spatial variation in the FOV and additional constraints (e.g., sparsity).

References

- [1] P. E. Valk, D. L. Bailey, D. W. Townsend and M. N. Maisey, “Positron emission tomography: basic science and clinical practice,” Springer, 2004.
- [2] J. Lee, X. Geets, V. Grégoire et al., “Edge-preserving filtering of images with low photon counts,” *IEEE transactions on pattern analysis and machine intelligence*, **30**(6):1014–1027, 2008.
- [3] N. M. Alpert, A. Reilhac, T. C. Chio and I. Selesnick, “Optimization of dynamic measurement of receptor kinetics by wavelet denoising,” *Neuroimage*, **30**(2):444–451, 2006.
- [4] F. Sroubek, M. Sorel, J. Boldys et al., “PET Image Reconstruction using Prior Information from CT or MRI,” in *Image Processing (ICIP), IEEE International Conference on*, 2493–2496, 2009.
- [5] S. Guérit, L. Jacques, B. Macq and J. Lee, “Post-Reconstruction Deconvolution of PET Images by Total Generalized Variation Regularization,” in *23rd European Signal Processing Conference (EUSIPCO)*, 629–633, 2015.
- [6] A. González, V. Delouille and L. Jacques, “Non-parametric PSF estimation from celestial transit solar images using blind deconvolution,” *J. Space Weather Space Clim.*, **6**(A1), 2016.
- [7] W. Hoeffding, “Probability Inequalities for Sums of Bounded Random Variables,” *J. Amer. Statist. Assoc.*, **58**(301):13–30, 1963.
- [8] D. L. Donoho and J. M. Johnstone, “Ideal spatial adaptation by wavelet shrinkage,” *Biometrika*, **81**(3):425–455, 1994.
- [9] S. Anthoine, J.-F. Aujol, Y. Boursier, and C. Mélot, “Some proximal methods for Poisson intensity CBCT and PET,” *Inverse Prob. Imaging*, **6**(4):565–598, 2012.
- [10] A. Chambolle and T. Pock, “A first-order primal-dual algorithm for convex problems with applications to imaging,” *J. Math. Imaging Vision*, **40**(1):120–145, 2011.
- [11] N. Parikh and S. Boyd, “Proximal Algorithms,” *Found. Trends Optim.*, **1**(3):127–239, 2014.
- [12] A. Chambolle, “An algorithm for total variation minimization and applications,” *J. Math. Imaging Vision*, **20**(1-2):89–97, 2004.
- [13] H. Attouch, J. Bolte, P. Redont and A. Soubeyran, “Proximal Alternating Minimization and Projection Methods for Nonconvex Problems: An Approach Based on the Kurdyka-Łojasiewicz Inequality,” *Math. Oper. Res.*, **35**(2):438–457, 2010.

A Non-Convex Approach to Blind Calibration for Linear Random Sensing Models

Valerio Cambarelli*, Laurent Jacques*

ICTEAM/ELEN, ISPGROUP, Université catholique de Louvain, Belgium.

Abstract— Performing blind calibration is highly important in modern sensing strategies, particularly when calibration aided by multiple, accurately designed training signals is infeasible or resource-consuming. We here address it as a naturally-formulated non-convex problem for a linear model with sub-Gaussian random sensing vectors in which both the sensor gains and the signal are unknown. A sample complexity bound is derived to assess that solving the problem by projected gradient descent with a suitable initialisation provably converges to the global optimum. These findings are supported by numerical evidence on the phase transition of blind calibration and by an imaging example.

1 Introduction

The problem of acquiring an unknown signal under sensing model errors is crucial for modern sensing strategies such as Compressed Sensing (CS), in which such errors are inevitable in physical implementations, have direct impact on the attainable quality [1], and may be to some extent exploited for security purposes [2]. However, if the signals and model errors are stationary, the use of random sensing operators in CS also suggests that repeating the acquisition (*i.e.*, taking more *snapshots*) under new draws of the sensing model could suffice to diversify the measurements and learn both unknown quantities. We address the case of sensing a single unstructured vector $\mathbf{x} \in \mathbb{R}^n$ by collecting p snapshots of m random projections, *i.e.*,

$$\mathbf{y}_l = \bar{\mathbf{d}} \mathbf{A}_l \mathbf{x}, \quad \bar{\mathbf{d}} := \text{diag}(\mathbf{d}) \in \mathbb{R}^{m \times m}, \quad l \in [p] := \{1, \dots, p\}, \quad (1)$$

where $\mathbf{y}_l = (y_{1,l}, \dots, y_{m,l})^\top \in \mathbb{R}^m$ is the l -th snapshot; $\mathbf{d} = (d_1, \dots, d_m)^\top \in \mathbb{R}_+^m$ is an unknown, positive and bounded gain vector that is identical throughout the p snapshots; the random matrices $\mathbf{A}_l \in \mathbb{R}^{m \times n}$ are independent and identically distributed (i.i.d.) and each \mathbf{A}_l has i.i.d. rows, the i -th row $\mathbf{a}_{i,l}^\top \in \mathbb{R}^n$ being a centred isotropic sub-Gaussian random vector (*i.e.*, $\mathbb{E}[\mathbf{a}_{i,l}] = \mathbf{0}_n$, $\mathbb{E}[\mathbf{a}_{i,l} \mathbf{a}_{i,l}^\top] = \mathbf{I}_n$).

This essentially bilinear model, referred to as *blind calibration* [3, 4] is motivated by compressive imaging applications, where unknown \mathbf{d} are associated to physical gains and attenuations in a sensor array, while the random projections of an image \mathbf{x} are obtained by light modulation (*e.g.*, by random convolution [5–8]). Similarly, model errors concern radar signal processing applications (*e.g.*, as discussed in [9, 10]). In such contexts, the knowledge of \mathbf{d} could critically improve the accuracy of the sensing model. This is typically achieved by solving convex or alternating minimisation problems [3, 4, 11] that use multiple training signals \mathbf{x}_l instead of randomising the sensing operator. More recently, *lifting* approaches [9, 10] have been proposed to jointly recover (\mathbf{x}, \mathbf{d}) in (1) (as well as more general *blind deconvolution* models, [12–14]). Their main limitation is in that a semidefinite program is solved to recover a very large rank-one matrix $\mathbf{x} \mathbf{d}^\top$, an approach that rapidly becomes computationally inefficient as m and n exceed a few hundreds.

Quantity	Finite-sample ($p < \infty$)	Expectation ($\mathbb{E}_{\mathbf{a}_i, l}, p \rightarrow \infty$)
Objective: $f(\boldsymbol{\xi}, \boldsymbol{\gamma})$	$\frac{1}{2mp} \sum_{l=1}^p \ \bar{\boldsymbol{\gamma}} \mathbf{A}_l \boldsymbol{\xi} - \mathbf{d} \mathbf{A}_l \mathbf{x}\ _2^2$	$\frac{1}{2m} (\ \boldsymbol{\xi}\ _2^2 \ \boldsymbol{\gamma}\ _2^2 + \ \mathbf{x}\ _2^2 \ \mathbf{d}\ _2^2 - 2(\boldsymbol{\gamma}^\top \mathbf{d})(\boldsymbol{\xi}^\top \mathbf{x}))$
Signal gradient: $\nabla_{\boldsymbol{\xi}} f(\boldsymbol{\xi}, \boldsymbol{\gamma})$	$\frac{1}{mp} \sum_{l=1}^p \mathbf{A}_l^\top \bar{\boldsymbol{\gamma}} (\bar{\boldsymbol{\gamma}} \mathbf{A}_l \boldsymbol{\xi} - \mathbf{d} \mathbf{A}_l \mathbf{x})$	$\frac{1}{m} (\ \boldsymbol{\gamma}\ _2^2 \boldsymbol{\xi} - (\boldsymbol{\gamma}^\top \mathbf{d}) \mathbf{x})$
Gain gradient: $\nabla_{\boldsymbol{\gamma}} f(\boldsymbol{\xi}, \boldsymbol{\gamma})$	$\frac{1}{mp} \sum_{l=1}^p \bar{\mathbf{A}}_l \bar{\boldsymbol{\xi}} (\bar{\boldsymbol{\gamma}} \mathbf{A}_l \boldsymbol{\xi} - \mathbf{d} \mathbf{A}_l \mathbf{x})$	$\frac{1}{m} (\ \boldsymbol{\xi}\ _2^2 \boldsymbol{\gamma} - (\boldsymbol{\xi}^\top \mathbf{x}) \mathbf{d})$
Hessian: $\mathcal{H}^2 f(\boldsymbol{\xi}, \boldsymbol{\gamma})$	$\frac{1}{mp} \sum_{l=1}^p \begin{bmatrix} \mathbf{A}_l^\top \bar{\boldsymbol{\gamma}} \bar{\boldsymbol{\gamma}} \mathbf{A}_l & \mathbf{A}_l^\top \bar{\boldsymbol{\gamma}} \mathbf{d} \mathbf{A}_l \mathbf{x} \\ \bar{\boldsymbol{\gamma}} \mathbf{d} \mathbf{A}_l \mathbf{x} \bar{\boldsymbol{\gamma}} \mathbf{A}_l & \mathbf{d} \mathbf{d}^\top \end{bmatrix}$	$\frac{1}{m} \begin{bmatrix} \ \boldsymbol{\gamma}\ _2^2 \mathbf{I}_n & -\boldsymbol{\gamma} \boldsymbol{\xi}^\top - \boldsymbol{\xi} \boldsymbol{\gamma}^\top \\ \boldsymbol{\xi} \boldsymbol{\gamma}^\top + \boldsymbol{\gamma} \boldsymbol{\xi}^\top & \ \boldsymbol{\xi}\ _2^2 \mathbf{I}_m \end{bmatrix}$
Initialisation: $(\boldsymbol{\xi}_0, \boldsymbol{\gamma}_0)$	$\left(\frac{1}{mp} \sum_{l=1}^p (\mathbf{A}_l)^\top \mathbf{d} \mathbf{A}_l \mathbf{x}, \mathbf{1}_m \right)$	$\left(\frac{\ \mathbf{d}\ _1}{m} \mathbf{x}, \mathbf{1}_m \right)$

Table 1: Finite-sample and expected values of the objective function; its gradient components and Hessian matrix; the initialisation point $(\boldsymbol{\xi}_0, \boldsymbol{\gamma}_0)$. $\bar{\cdot}$ abbreviates the $\text{diag}(\cdot)$ operator.

2 A Non-Convex Approach

Inspired by recent results on fast, provably convergent non-convex approaches to phase retrieval [15–18] we argue that the blind calibration problem of recovering the two unstructured vectors (\mathbf{x}, \mathbf{d}) in (1) can be solved exactly by a non-convex problem described hereafter. Since no *a priori* structure is assumed on (\mathbf{x}, \mathbf{d}) we operate in the case $mp \geq n + m$ and solve

$$(\hat{\mathbf{x}}, \hat{\mathbf{d}}) = \underset{\boldsymbol{\xi} \in \mathbb{R}^n, \boldsymbol{\gamma} \in \Pi_+^m}{\text{argmin}} \frac{1}{2mp} \sum_{l=1}^p \|\bar{\boldsymbol{\gamma}} \mathbf{A}_l \boldsymbol{\xi} - \mathbf{y}_l\|_2^2, \quad (2)$$

given $\{\mathbf{y}_l\}_{l=1}^p, \{\mathbf{A}_l\}_{l=1}^p$ with $\Pi_+^m = \{\boldsymbol{\gamma} \in \mathbb{R}_+^m, \mathbf{1}_m^\top \boldsymbol{\gamma} = m\}$ being the scaled probability simplex. The geometry of this problem is well understood by observing the objective $f(\boldsymbol{\xi}, \boldsymbol{\gamma})$ with its gradient and Hessian matrix, computed in Table 1 for finite and asymptotic p . All finite-sample expressions therein are unbiased estimates of their expectation w.r.t. $\mathbf{a}_{i,l}$. There, we evince that all points in $\{(\boldsymbol{\xi}, \boldsymbol{\gamma}) \in \mathbb{R}^n \times \mathbb{R}^m : \boldsymbol{\xi} = \frac{1}{\alpha} \mathbf{x}, \boldsymbol{\gamma} = \alpha \mathbf{d}, \alpha \in \mathbb{R} \setminus \{0\}\}$ are global minimisers of $f(\boldsymbol{\xi}, \boldsymbol{\gamma})$. Moreover, $f(\boldsymbol{\xi}, \boldsymbol{\gamma})$ is easily shown to be generally non-convex¹ as there exist plenty of counterexamples $(\boldsymbol{\xi}', \boldsymbol{\gamma}')$ for which $\mathcal{H}f(\boldsymbol{\xi}', \boldsymbol{\gamma}') \not\leq 0$.

By applying the constraint $\boldsymbol{\gamma} \in \Pi_+^m$, one minimiser $(\mathbf{x}^*, \mathbf{d}^*) = \left(\frac{\|\mathbf{d}\|_1}{m} \mathbf{x}, \frac{m}{\|\mathbf{d}\|_1} \mathbf{d} \right)$ remains for $mp \geq n + m$, which is exact up to $\alpha = m/\|\mathbf{d}\|_1$. Assuming that $\mathbf{d} \in \mathbb{R}_+^m$ in (1) is bounded amounts to letting² $\mathbf{d}^* := \mathbf{1}_m + \boldsymbol{\omega} \in \mathcal{C}_\rho \subset \Pi_+^m$, $\boldsymbol{\omega} \in \mathbf{1}_m^\perp \cap \rho \mathbb{B}_\infty^m$ for a maximum deviation $\rho = \|\mathbf{d}^* - \mathbf{1}_m\|_\infty < 1$ where $\mathcal{C}_\rho := \mathbf{1}_m + \mathbf{1}_m^\perp \cap \rho \mathbb{B}_\infty^m$. The test vector is also cast as $\boldsymbol{\gamma} := \mathbf{1}_m + \boldsymbol{\varepsilon} \in \mathcal{C}_\rho$. While the problem clearly remains non-convex, by defining a *distance* $\Delta(\boldsymbol{\xi}, \boldsymbol{\gamma}) := \|\boldsymbol{\xi} - \mathbf{x}^*\|_2^2 + \frac{\|\boldsymbol{\omega}\|_2^2}{m} \|\boldsymbol{\gamma} - \mathbf{d}^*\|_2^2$, and a *neighbourhood* of the global minimiser $(\mathbf{x}^*, \mathbf{d}^*)$ as $\mathcal{D}_{\kappa, \rho} := \{(\boldsymbol{\xi}, \boldsymbol{\gamma}) \in \mathbb{R}^n \times \mathcal{C}_\rho : \Delta(\boldsymbol{\xi}, \boldsymbol{\gamma}) \leq \kappa^2 \|\mathbf{x}^*\|_2^2\}$ for $\kappa, \rho \in [0, 1)$, it is easily shown that (2) is locally convex in expectation on $\mathcal{D}_{\kappa, \rho}$ for sufficiently small κ . Thus, we require an *initialisation* point $(\boldsymbol{\xi}_0, \boldsymbol{\gamma}_0)$ to lie in a small $\mathcal{D}_{\kappa, \rho}$ for which a notion of local convexity holds for finite p . Similarly to [15] we see that initialising $\boldsymbol{\xi}_0$ as in Table 1 grants $\mathbb{E}[\boldsymbol{\xi}_0] \equiv \mathbf{x}^*$, *i.e.*, asymptotically in p this initialisation yields the exact solution. We also let $\boldsymbol{\gamma}_0 = \mathbf{1}_m$ ($\boldsymbol{\varepsilon}_0 = \mathbf{0}_m$) and run projected gradient descent to solve (2), as summarised in Algorithm 1. Note that, since we assume ρ to be small (*i.e.*, \mathbf{d}^* is far from the vertices of Π_+^m) and the optimisation starts on

*LJ and VC are funded by the Belgian FNRS. Part of this study is funded by the project ALTERSENSE (MIS-FNRS).

¹It is *biconvex* [10], *i.e.*, convex once either $\boldsymbol{\xi}$ or $\boldsymbol{\gamma}$ are fixed.

²The orthogonal complement of $\mathbf{1}_m$ is $\mathbf{1}_m^\perp = \{\mathbf{v} \in \mathbb{R}^m : \mathbf{1}_m^\top \mathbf{v} = 0\}$.

```

1: Initialise  $\xi_0 := \frac{1}{mp} \sum_{l=1}^p (\mathbf{A}_l)^\top \mathbf{y}_l$ ,  $\gamma_0 := \mathbf{1}_m$ ,  $k := 0$ .
2: while stop criteria not met do
3:    $\mu_\xi := \operatorname{argmin}_{v \in \mathbb{R}} f(\xi_k - v \nabla_{\xi} f(\xi_k, \gamma_k), \gamma_k)$  {Line search in  $\xi$ }
4:    $\mu_\gamma := \operatorname{argmin}_{v \in \mathbb{R}} f(\xi_k, \gamma_k - v \nabla_{\gamma} f(\xi_k, \gamma_k))$  {Line search in  $\gamma$ }
5:    $\xi_{k+1} := \xi_k - \mu_\xi \nabla_{\xi} f(\xi_k, \gamma_k)$ 
6:    $\gamma_{k+1} := \gamma_k - \mu_\gamma \nabla_{\gamma} f(\xi_k, \gamma_k)$ 
7:    $\gamma_{k+1} := P_{C_\rho} \gamma_{k+1}$  {Projection on  $C_\rho$ }
8:    $k := k + 1$ 
9: end while

```

Algorithm 1: Non-Convex Blind Calibration by Projected Gradient Descent.

$\gamma_0 = \mathbf{1}_m$, we are allowed to first project the gradient step as $\nabla_{\gamma}^{\perp} f(\xi, \gamma) := P_{\mathbf{1}_m}^{\perp} \nabla_{\gamma} f(\xi, \gamma)$ with $P_{\mathbf{1}_m}^{\perp} := \mathbf{I}_m - \frac{1}{m} \mathbf{1}_m \mathbf{1}_m^{\top}$, then project it on C_ρ (i.e., P_{C_ρ} ; this step is useful for the proofs and not required in all the experiments). The line searches in 3-4: of Algorithm 1 are solved in closed-form and introduced to improve the convergence rate. Below, we obtain the conditions that ensure convergence of this descent algorithm to the exact solution $(\mathbf{x}^*, \mathbf{d}^*)$ for fixed step sizes μ_ξ, μ_γ .

3 Recovery Guarantees

Having assumed that all mp sensing vectors $\mathbf{a}_{i,l}$ are i.i.d. sub-Gaussian, we establish the sample complexity required for the initialisation to lie in $\mathcal{D}_{\kappa,\rho}$ with very high probability. This and all other statements rely on Bernstein-type concentration inequalities [19] and some simple geometry of (2) in $\mathcal{D}_{\kappa,\rho}$.

Proposition 1 (Initialisation Proximity). *Let (ξ_0, γ_0) be as in Algorithm 1. For any $\epsilon \in (0, 1)$, $t > 1$, provided $n \gtrsim t \log(mp)$ and $mp \gtrsim \epsilon^{-2}(n+m) \log(n\epsilon^{-1})$ we have that, with probability exceeding $1 - Ce^{-c\epsilon^2 mp} - (mp)^{-t}$ for some $C, c > 0$, $\|\xi_0 - \mathbf{x}^*\|_2 \leq \epsilon \|\mathbf{x}^*\|_2$. Since $\gamma_0 = \mathbf{1}_m$ we also have $\|\gamma_0 - \mathbf{d}^*\|_\infty \leq \rho < 1$. Thus $(\xi_0, \gamma_0) \in \mathcal{D}_{\kappa,\rho}$ with the same probability and $\kappa := \sqrt{\epsilon^2 + \rho^2}$.*

With analogue tools we are able to state when a single gradient descent step from any (ξ, γ) reduces, with very high probability, the distance w.r.t. the global minimum. This requires establishing a *regularity condition* on $\nabla f(\xi, \gamma)$ holding uniformly for all $(\xi, \gamma) \in \mathcal{D}_{\kappa,\rho}$ (similarly to [15, Condition 7.9]).

Proposition 2 (Regularity condition in $\mathcal{D}_{\kappa,\rho}$). *For any $\delta \in (0, 1)$, $\rho \in [0, 1)$, $t > 1$, provided $\rho < \frac{1-2\delta}{9}$, $n \gtrsim t \log(mp)$, $p \gtrsim \delta^{-2} \log m$ and $\sqrt{mp} \gtrsim \delta^{-2}(n+m) \log(\frac{n}{\delta})$, with probability exceeding $1 - C[me^{-c\delta^2 p} + e^{-c\delta^2 \sqrt{mp}} + (mp)^{-t}]$ for some $C, c > 0$, we have that for all $(\xi, \gamma) \in \mathcal{D}_{\kappa,\rho}$,*

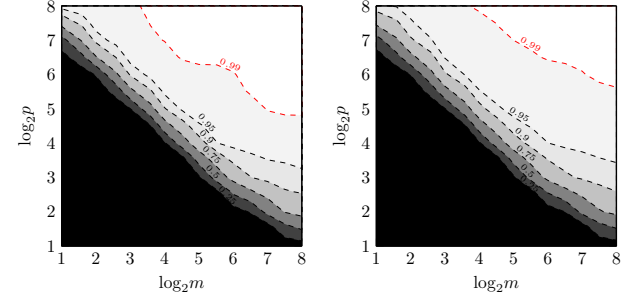
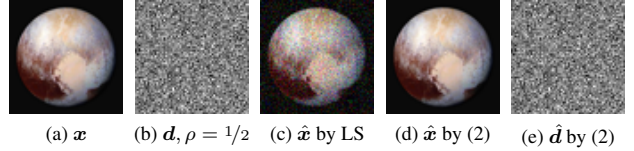
$$\begin{aligned} \left\langle \nabla^{\perp} f(\xi, \gamma), \begin{bmatrix} \xi - \mathbf{x}^* \\ \gamma - \mathbf{d}^* \end{bmatrix} \right\rangle &\geq \frac{1}{2} \eta \Delta(\xi, \gamma) \quad (\text{Bounded curvature}) \\ \|\nabla^{\perp} f(\xi, \gamma)\|_2^2 &\leq L^2 \Delta(\xi, \gamma) \quad (\text{Lipschitz gradient}) \end{aligned}$$

for $\eta := 2(1 - 9\rho - 2\delta) > 0$, $L := 4\sqrt{2}[1 + \rho + (1 + \kappa)\|\mathbf{x}^*\|_2]$.

From Proposition 2 it follows that the neighbourhood $\mathcal{D}_{\kappa,\rho}$ is a basin of attraction to the solution $(\mathbf{x}^*, \mathbf{d}^*)$, i.e., we can show that the update from any $(\xi_k, \gamma_k) \in \mathcal{D}_{\kappa,\rho}$ to $(\xi_{k+1}, \gamma_{k+1})$ is so that the distance $\Delta(\xi, \gamma)$ decreases under an upper bound on μ_ξ, μ_γ specified in the following result.

Theorem 1 (Provable Convergence to the Exact Solution). *Under the conditions of Proposition 1, 2 we have that, with probability exceeding $1 - C[me^{-c\delta^2 p} + e^{-c\delta^2 \sqrt{mp}} + e^{-c\epsilon^2 mp} + (mp)^{-t}]$ for some $C, c > 0$, Algorithm 1 with $\mu_\xi := \mu, \mu_\gamma := \mu \frac{m}{\|\mathbf{x}^*\|_2^2}$ has error decay*

$$\Delta(\xi_k, \gamma_k) \leq (1 - \eta\mu + \frac{L^2}{\tau} \mu^2)^k (\epsilon^2 + \rho^2) \|\mathbf{x}^*\|_2^2, (\xi_k, \gamma_k) \in \mathcal{D}_{\kappa,\rho}$$

Figure 1: Empirical phase transition of (2) for $n = 2^8$, $\rho = 10^{-3}$ (left) and $\rho = 10^{-0.5}$ (right). The probability value P_C is reported on each level set.Figure 2: A practical, high-dimensional example of blind calibration against unknown, unstructured gains \mathbf{d} with $m = n$, $p = 4$ snapshots.

at any iteration $k > 0$ provided $\mu \in (0, \tau\eta/L^2)$, $\tau := \min\{1, \|\mathbf{x}^*\|_2^2/m\}$. Hence, $\Delta(\xi_k, \gamma_k) \xrightarrow[k \rightarrow \infty]{} 0$.

Let us mention finally that if additive measurement noise $\mathbf{N} := (\mathbf{n}_1, \dots, \mathbf{n}_p) \in \mathbb{R}^{m \times p}$ corrupts the p snapshots of (1), then it can be shown that $\Delta(\xi_k, \gamma_k) \rightarrow \sigma^2$ as $k \rightarrow \infty$, with $\sigma^2 \gtrsim \frac{1}{mp} \|\mathbf{N}\|_F^2$. Thus, Algorithm 1 is robust to noise, its solution degrading gracefully with σ^2 .

4 Numerical Experiments

Empirical Phase Transition: To characterise the phase transition of (2) solved by Algorithm 1 we ran some extensive simulations by generating 256 random instances of (2) for each configuration $\log_2 n \times \log_2 m \times \log_2 p \times \log_{10} \rho \in \{1, \dots, 8\}^3 \times \{-3, \dots, 0\}$, drawing $\mathbf{d}^* = \mathbf{1}_m + \boldsymbol{\omega}$ with $\boldsymbol{\omega} \in \mathbf{1}_m^{\perp}$ drawn uniformly at random on the sphere $\rho \mathbb{S}_{\infty}^{m-1}$. Then we evaluated $P_C := \mathbb{P} \left[\max \left\{ \frac{\|\hat{\mathbf{d}} - \mathbf{d}^*\|_2}{\|\mathbf{d}^*\|_2}, \frac{\|\hat{\mathbf{x}} - \mathbf{x}^*\|_2}{\|\mathbf{x}^*\|_2} \right\} < \zeta \right]$ on the trials with $\zeta = 10^{-3}$ chosen according to the stop criterion $f(\xi, \gamma) < 10^{-7}$. Of this large dataset we only report the case $n = 2^8$ in Fig. 1, highlighting the contour levels of P_C for $\rho = \{10^{-3}, 10^{-0.5}\}$ as a function of $\log_2 m$ and $\log_2 p$.

Blind Calibration of an Imaging System: To test (2) in a realistic context, we assume that \mathbf{x} is a $n = 64 \times 64$ pixel image acquired by an imaging system following (1), in which its $m = 64 \times 64$ pixel sensor array suffers from large *pixel response non-uniformity* [20]. This is simulated by generating \mathbf{d} as before with $\rho = 1/2$. We capture $p = 4$ snapshots with $\mathbf{a}_{i,l} \sim \mathcal{N}(\mathbf{0}_n, \mathbf{I}_n)$. By running Algorithm 1, the recovered $(\hat{\mathbf{x}}, \hat{\mathbf{d}}) \equiv (\mathbf{x}, \mathbf{d})$ attains $\max \left\{ \frac{\|\hat{\mathbf{d}} - \mathbf{d}^*\|_2}{\|\mathbf{d}^*\|_2}, \frac{\|\hat{\mathbf{x}} - \mathbf{x}^*\|_2}{\|\mathbf{x}^*\|_2} \right\} \approx -147.38$ dB. Instead, by fixing $\gamma = \mathbf{1}_m$ and solving (2) only in ξ , i.e., finding a least squares (LS) $\hat{\mathbf{x}}$, we obtain $\frac{\|\hat{\mathbf{x}} - \mathbf{x}^*\|_2}{\|\mathbf{x}^*\|_2} \approx -5.50$ dB.

5 Conclusion

We presented and solved a non-convex formulation of the blind calibration problem for a random linear model. The obtained sample complexity could be further improved by exploiting, e.g., a sparse model for \mathbf{x}, \mathbf{d} ; in absence of such priors, the exact solution is achieved at a rate $\sqrt{mp} \gtrsim (n+m) \log(n)$.

References

- [1] M. A. Herman and T. Strohmer, "General deviants: An analysis of perturbations in compressed sensing," *IEEE Journal of Selected Topics in Signal Processing*, vol. 4, no. 2, pp. 342–349, 2010.
- [2] V. Cambareri, M. Mangia, F. Pareschi, R. Rovatti, and G. Setti, "Low-complexity multiclass encryption by compressed sensing," *IEEE Transactions on Signal Processing*, vol. 63, no. 9, pp. 2183–2195, 2015.
- [3] L. Balzano and R. Nowak, "Blind calibration of networks of sensors: Theory and algorithms," in *Networked Sensing Information and Control*. Springer, 2008, pp. 9–37.
- [4] C. Bilen, G. Puy, R. Gribonval, and L. Daudet, "Convex Optimization Approaches for Blind Sensor Calibration Using Sparsity," *IEEE Transactions on Signal Processing*, vol. 62, no. 18, pp. 4847–4856, Sep. 2014.
- [5] J. Romberg, "Compressive sensing by random convolution," *SIAM Journal on Imaging Sciences*, vol. 2, no. 4, pp. 1098–1128, 2009.
- [6] S. Bahmani and J. Romberg, "Compressive deconvolution in random mask imaging," *IEEE Transactions on Computational Imaging*, vol. 1, no. 4, pp. 236–246, 2015.
- [7] T. Bjorklund and E. Magli, "A parallel compressive imaging architecture for one-shot acquisition," in *2013 IEEE Picture Coding Symposium (PCS)*. IEEE, 2013, pp. 65–68.
- [8] K. Degraux, V. Cambareri, B. Geelen, L. Jacques, G. Lafruit, and G. Setti, "Compressive Hyperspectral Imaging by Out-of-Focus Modulations and Fabry-Pérot Spectral Filters," in *International Traveling Workshop on Interactions between Sparse models and Technology (iTWIST)*, 2014.
- [9] B. Friedlander and T. Strohmer, "Bilinear compressed sensing for array self-calibration," in *2014 48th Asilomar Conference on Signals, Systems and Computers*, Nov. 2014, pp. 363–367.
- [10] S. Ling and T. Strohmer, "Self-calibration and biconvex compressive sensing," *Inverse Problems*, vol. 31, no. 11, p. 115002, 2015.
- [11] J. Lipor and L. Balzano, "Robust blind calibration via total least squares," in *2014 IEEE International Conference on Acoustics, Speech and Signal Processing (ICASSP)*. IEEE, 2014, pp. 4244–4248.
- [12] A. Ahmed, B. Recht, and J. Romberg, "Blind deconvolution using convex programming," *IEEE Transactions on Information Theory*, vol. 60, no. 3, pp. 1711–1732, 2014.
- [13] S. Ling and T. Strohmer, "Blind deconvolution meets blind demixing: Algorithms and performance bounds," *arXiv preprint arXiv:1512.07730*, 2015.
- [14] A. Ahmed, A. Cosse, and L. Demanet, "A convex approach to blind deconvolution with diverse inputs," in *2015 IEEE 6th International Workshop on Computational Advances in Multi-Sensor Adaptive Processing (CAMSAP)*, Dec 2015, pp. 5–8.
- [15] E. Candès, X. Li, and M. Soltanolkotabi, "Phase Retrieval via Wirtinger Flow: Theory and Algorithms," *IEEE Transactions on Information Theory*, vol. 61, no. 4, pp. 1985–2007, Apr. 2015.
- [16] C. D. White, S. Sanghavi, and R. Ward, "The local convexity of solving systems of quadratic equations," *arXiv:1506.07868 [math, stat]*, Jun. 2015, arXiv: 1506.07868.
- [17] Y. Chen and E. Candès, "Solving random quadratic systems of equations is nearly as easy as solving linear systems," in *Advances in Neural Information Processing Systems*, 2015, pp. 739–747.
- [18] J. Sun, Q. Qu, and J. Wright, "A geometric analysis of phase retrieval," in *2016 IEEE International Symposium on Information Theory (ISIT)*, July 2016, pp. 2379–2383.
- [19] R. Vershynin, "Introduction to the non-asymptotic analysis of random matrices," in *Compressed Sensing: Theory and Applications*. Cambridge University Press, 2012, pp. 210–268.
- [20] M. M. Hayat, S. N. Torres, E. Armstrong, S. C. Cain, and B. Yasuda, "Statistical algorithm for nonuniformity correction in focal-plane arrays," *Applied Optics*, vol. 38, no. 5, pp. 772–780, 1999.

Sparse Support Recovery with ℓ_∞ Data Fidelity

Kévin Degraux¹, Gabriel Peyré³, Jalal M. Fadili² and Laurent Jacques¹

¹ISPGROUP/ICTEAM, FNRS, Université catholique de Louvain, Belgium. ²Normandie Univ, ENSICAEN, UNICAEN, GREYC, France.

³CNRS, Ceremade, Université Paris-Dauphine, France.

Abstract— This paper investigates non-uniform guarantees of ℓ_1 minimization, subject to an ℓ_∞ data fidelity constraint, to stably recover the support of a sparse vector when solving noisy linear inverse problems. Our main contribution consists in giving a sufficient condition, framed in terms of the notion of dual certificates, to ensure that a solution of the ℓ_1 - ℓ_∞ convex program has a support containing that of the original vector, when the noise level is sufficiently small.

1 Introduction

Problem statement We consider the following forward model

$$y = \Phi x_0 + w,$$

where the unknown vector $x_0 \in \mathbb{R}^n$ is supposed sparse and where the linear measurements $\Phi x_0 \in \mathbb{R}^m$ are corrupted by an additive noise $w \in \mathbb{R}^m$ such that $\|w\|_\alpha \leq \delta$, where $\|\cdot\|_\alpha$ is the ℓ_α -norm, $\alpha \in [1, \infty]$. The sparsity-promoting convex program

$$\min_x \{\|x\|_1 \text{ s.t. } \|\Phi x - y\|_\alpha \leq \tau\}, \quad (\mathcal{P}_\alpha^\tau(y))$$

can be used in order to recover an estimate of x_0 . The support of x_0 is noted $I \stackrel{\text{def}}{=} \text{supp}(x_0)$ where $\text{supp}(u) \stackrel{\text{def}}{=} \{i : |u_i| > 0\}$. Note that in this work, we implicitly assume that the problem is feasible, i.e., $(\text{Im}(\Phi) - y) \cap \tau B_\alpha \neq \emptyset$ where $B_\alpha \stackrel{\text{def}}{=} \{z : \|z\|_\alpha \leq 1\}$ and $\text{Im}(\Phi)$ is the image of Φ . This will be the case, for instance as soon as $\delta \leq \tau$ or if $\text{Im}(\Phi) = \mathbb{R}^m$. More precisely, our chief goal is to analyze the stability of the support of $x_\tau \in \text{Argmin}(\mathcal{P}_\alpha^\tau(y))$, i.e., $\text{supp}(x_\tau)$, to the noise w when δ is small in front of $\underline{x} \stackrel{\text{def}}{=} \min_{i \in I} |x_{0,i}|$, i.e., the signal to noise ratio is sufficiently high, and when τ is chosen appropriately. For the sake of conciseness, we will focus on the case $\alpha = \infty$. The latter is popular for instance to account for quantization noise w such as is the case in quantized compressed sensing (QCS), assuming a uniform and dithered quantizer is applied on Φx_0 [10, 3, 11].

Identifiability An important assumption is that x_0 is a solution of *Basis Pursuit* (BP) [6],

$$\min_x \{\|x\|_1 \text{ s.t. } \Phi x = \Phi x_0\}, \quad (\mathcal{P}^0(\Phi x_0))$$

i.e., $x_0 \in \text{Argmin}(\mathcal{P}^0(\Phi x_0))$. In that case, we say that x_0 is *identifiable*. Note that BP is equivalent to $(\mathcal{P}_\alpha^\tau(\Phi x_0))$ when $\tau = 0$.

Dual certificates A vector $\bar{p} \in \mathbb{R}^m$ is called a *dual certificate* when the pair (\bar{p}, x_0) obeys $\Phi^* \bar{p} \in \partial \|x_0\|_1$, i.e.,

$$\Phi_{\cdot, I}^* \bar{p} = \text{sign}(x_{0, I}) \quad \text{and} \quad \|\Phi^* \bar{p}\|_\infty \leq 1. \quad (1)$$

Note that $\Phi_{\cdot, I}$ is the matrix Φ restricted to the columns indexed by I and the dot indicates that we keep all the rows. Transposition is applied afterwards and we use this convention in the rest of the paper. When moreover, $\|\Phi_{\cdot, I}^* \bar{p}\|_\infty < 1$, the certificate is

called *non degenerate*. Note that as for $(\mathcal{P}^0(\Phi x_0))$, these definitions are independent of the data fidelity term. It can be verified, using the first order optimality conditions of $(\mathcal{P}^0(\Phi x_0))$, that the existence of a dual certificate is equivalent to x_0 being identifiable [8]. Depending on the specific fidelity term used (here the value of α), the support stability of the solution to $(\mathcal{P}_\alpha^\tau(y))$ is governed by a specific choice of \bar{p} .

Minimum norm certificate The certificates of minimum ℓ_β -norm, the Hölder dual of the ℓ_α -norm with $\frac{1}{\alpha} + \frac{1}{\beta} = 1$, play an important role regarding support stability under small noise. They read

$$p_\beta \in \underset{p}{\text{Argmin}} \{ \|p\|_\beta \text{ s.t. } \Phi_{\cdot, I}^* p = \text{sign}(x_{0, I}), \|\Phi^* p\|_\infty \leq 1 \}. \quad (\mathcal{D}_\beta^0(\Phi x_0))$$

Since $\|\cdot\|_\beta$ is coercive, the existence of \bar{p} implies the existence of p_β . Moreover, when $\beta \in]1, \infty[$, $\|\cdot\|_\beta$ is strictly convex and p_β is therefore unique. We also define $J_\beta \stackrel{\text{def}}{=} \text{sat}(\Phi^* p_\beta)$, where $\text{sat}(u) \stackrel{\text{def}}{=} \{i : |u_i| = \|u\|_\infty\}$ is the *saturation support*. Non-degeneracy of p_β is equivalent to $J_\beta = I$. Note that if $\alpha = \infty$ then $\beta = 1$ and p_1 is not necessarily unique so that J_1 actually depends on p_1 .

Contributions Our main contribution is Theorem 1, stated in Section 2. It studies the support stability of a solution of $(\mathcal{P}_\alpha^\tau(y))$ with respect to I , for small τ compared to the smallest entry in magnitude of $x_{0, I}$ and for w satisfying $\|w\|_\infty < c_1 \tau$ for a certain constant $c_1 < 1$. More precisely, it provides a prediction of the support of x_τ which contains the support I of x_0 , hence the name *extended support*. To the best of our knowledge, this is the first non-uniform guarantee on support recovery with non-smooth data-fidelity (see related work hereafter). This paves the way for future similar analyses with other non-smooth data fidelity such as ℓ_1 to account for sparse noise [12, 9]. Finally in Section 3, numerical simulations illustrate our theoretical findings on a compressed sensing scenario, and showcase their ability to evaluate the degree of instability of ℓ_∞ quantized CS recovery as a function of the sparsity. We also provide a comparison with the known case $\alpha = 2$.

Relation to prior work The guarantees, framed in terms of the notion of dual certificates, are *non-uniform*. Unlike coherence-based [4] or RIP-based [5] results for compressed sensing, non-uniform results depend on each instance of x_0 . In particular, for a fixed Φ , they are *not* uniformly valid within the entire class of k -sparse signals. The seminal work of [8] analyses the Lasso $\min_x \{\frac{1}{2} \|y - \Phi x\|_2^2 + \lambda \|x\|_1\}$ and shows that non-degeneracy of p_2 , i.e., $J_2 = I$, is required for stable *exact* support stability under small noise. It also recovers with $(\mathcal{P}_2^\tau(y))$, under appropriate parameter correspondence $\lambda \leftrightarrow \tau$. In [13], a unified framework, has been proposed for consistent model selection under small noise for problems of the form $\min_x \{F(y - \Phi x) + \lambda R(x)\}$, where F is strongly convex and smooth and R is so-called partly smooth relative to a submanifold. This encompasses the Lasso, group Lasso and trace Lasso [1, 2]. In [7], the analysis goes one step further for $R = \|\cdot\|_1$ by introducing the extended support. They show, indeed, that under small noise, the extended support of the solution to $(\mathcal{P}_2^\tau(y))$ is predicted by J_2 .

LJ and KD are funded by the F.R.S.-FNRS. This work has been partly supported by the European Research Council (ERC project SIGMA-Vision). JF was partly supported by Institut Universitaire de France

2 Support stability at small noise

The theorem presented in this section defines the *extended support* and the *residual saturation support* and guarantees their stability under small noise. In order to simplify the notations, in the following we note $J \stackrel{\text{def}}{=} J_1$ and $\tilde{J} \stackrel{\text{def}}{=} J \setminus I$. We also define $S \stackrel{\text{def}}{=} \text{supp}(p_1)$. Since p_1 is not necessarily unique, S and J depend implicitly on the choice of p_1 .

Before stating the theorem, we give two technical assumptions. The first one reads

$$|S| = |J| \quad \text{and} \quad \Phi_{S,J} \text{ is invertible,} \quad (\text{INV}_{p_1})$$

where $\Phi_{S,J}$ is Φ restricted to its rows and columns indexed by S and J , respectively. We can then define $v \in \mathbb{R}^n$ supported on J such that $v_J \stackrel{\text{def}}{=} \Phi_{S,J}^{-1} \text{sign}(p_{1,S})$ (inversion is applied after the restriction) and give the second assumption

$$\mu \stackrel{\text{def}}{=} \|\Phi_{S^c, J} v\|_\infty < 1, \quad (\text{NDD}_{p_1})$$

where (NDD_{p_1}) stands for ‘‘non-degenerate duality’’. It can be shown that by construction, $\mu \leq 1$, and the (NDD_{p_1}) assumption simply strengthens this.

Remark 1. If Φ is randomly drawn from a continuous distribution with i.i.d. entries, e.g., Gaussian, then it can be shown that as soon as x_0 is identifiable, (INV_{p_1}) and (NDD_{p_1}) hold with probability 1 over the distribution of Φ . In fact, (INV_{p_1}) and (NDD_{p_1}) also hold under a weaker hypothesis on Φ but for the sake of brevity, we skip the details here.

Theorem 1. *Suppose that x_0 is solution to $(\mathcal{P}^0(\Phi x_0))$ and that there is a p_1 such that (INV_{p_1}) and (NDD_{p_1}) hold. Then there exist constants $c_1, c_2 > 0$ such that, for any (w, τ) satisfying $\|w\|_\infty < c_1 \tau$ and $\tau \leq c_2 \underline{x}$ we can compute a solution x_τ of $(\mathcal{P}_\infty^\tau(\Phi x_0 + w))$ in closed form as*

$$x_{\tau, J} = x_{0, J} + \Phi_{S, J}^{-1} w_S - \tau v_J. \quad (\text{closed form})$$

In particular, it satisfies

$$\begin{aligned} \text{supp}(x_\tau) &= J \supseteq I, & (\text{extended support}) \\ \text{sat}(y - \Phi x_\tau) &= S & (\text{residual saturation}) \\ \text{sign}(x_{\tau, I}) &= \text{sign}(x_{0, I}), & (\text{correct sign}) \\ \|x_{\tau, I^c}\|_\infty &\leq \tau / c_2 \leq \underline{x}, & (\text{maximum outsider}) \end{aligned}$$

i.e., the largest entry in magnitude outside the support decreases linearly with τ and is not bigger than \underline{x} .

This theorem shows that if the parameter τ is appropriately scaled, i.e., proportionally to \underline{x} and if the ℓ_∞ -noise is smaller than $c_1 \tau$ (where $c_1 < 1$ is small but not 0), then any solution x_τ takes a closed form directly related to w and to a minimal ℓ_1 -norm certificate. We know in advance its support J , its sign on I and a bound on its ‘‘outsider’’ entries on J . Note that the constants c_1 and c_2 are given explicitly in the proof as functions of Φ and p_1 but omitted here for brevity.

The following corollary guarantees support stability under the stronger assumption that $J = I$.

Corollary 1. *Under the same hypotheses, if $J = I$, then $|S| = |I|$ and there exist two constants $c_1, c_2 > 0$ such that, for any (w, τ) satisfying $\|w\|_\infty < c_1 \tau$ and $\tau \leq c_2 \underline{x}$, we can compute a solution x_τ of $(\mathcal{P}_\infty^\tau(y))$ in closed form, knowing that $v_I = \Phi_{S, I}^{-1} \text{sign}(\Phi_{S, I}^* \text{sign}(x_{0, I}))$, as*

$$x_{\tau, I} = x_{0, I} + \Phi_{S, I}^{-1} w_S - \tau v_I,$$

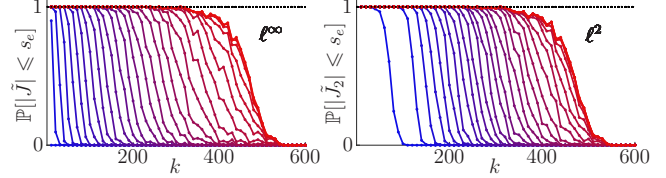


Fig. 1: *Progressive phase transition of the support excess size, i.e., result of a sweep over $s_e \in \{0, 10, 20, \dots\}$ of the empirical probability as a function of the sparsity k that x_0 is identifiable and that $|\tilde{J}| \leq s_e$ (left) or $|\tilde{J}_2| \leq s_e$ (right). The bluest corresponds to $s_e = 0$ and the reddest to the maximal empirical value of $|\tilde{J}|$ and $|\tilde{J}_2|$.*

that satisfies $\text{supp}(x_\tau) = I$, $\text{sign}(x_{\tau, I}) = \text{sign}(x_{0, I})$ and $\text{sat}(y - \Phi x_\tau) = S$.

In this case, p_1 is in fact *non degenerate* and takes the closed form $\Phi_{S, I}^{*-1} \text{sign}(x_{0, I})$. However, we need to solve an ℓ_1 minimization anyway to extract S . In comparison, in the $\alpha = 2$ case, the non-degeneracy of p_2 can easily be established with the so-called Fuchs pre-certificate $p_F \stackrel{\text{def}}{=} \Phi_{S, I}^{*+} \text{sign}(x_{0, I})$ where $\Phi_{S, I}^{*+}$ is the Moore-Penrose pseudo inverse of $\Phi_{S, I}^*$. Indeed, as shown in [8], $\|\Phi_{S, I}^* p_2\|_\infty < 1$ if and only if $\|\Phi_{S, I}^* p_F\|_\infty < 1$. Moreover, we present numerical evidence in Section 3 that $|\tilde{J}| = 0$ when $\alpha = \infty$, i.e., the hypothesis of Corollary 1, seems unlikely compared to the $\alpha = 2$ case.

3 Simulations

In order to illustrate Theorem 1 and in particular support stability, we perform the following simulation. We set $n = 1000$, $m = 900$ and generate 200 times a random sensing matrix $\Phi \sim \mathcal{N}(0, 1)^{m \times n}$. For each sensing matrix, we generate 60 different k -sparse vectors x_0 with support I where $k \stackrel{\text{def}}{=} |I|$ varies from 10 to 600. The non-zero entries of x_0 are randomly picked in $\{\pm 1\}$ with equal probability. For each case, we verify that x_0 is identifiable and we compute a minimum ℓ_1 -norm certificate p_1 , solution to $(\mathcal{D}_1^0(\Phi x_0))$ and in particular, the support excess $\tilde{J} \stackrel{\text{def}}{=} \text{sat}(\Phi^* p_1) \setminus I$. In order to provide a comparison with the well studied $(\mathcal{P}_2^\tau(y))$, we also compute the minimum ℓ_2 -norm certificate p_2 , solution to $(\mathcal{D}_2^0(\Phi x_0))$ and $\tilde{J}_2 \stackrel{\text{def}}{=} \text{sat}(\Phi^* p_2) \setminus I$. We define a threshold $s_e \in \mathbb{N}$ varying from 0 to ∞ . On Figure 1 we plot the probability that x_0 is identifiable and $|\tilde{J}|$ (or $|\tilde{J}_2|$ for p_2), the cardinality of the predicted support excess, is smaller or equal to s_e .

It is interesting to note that the probability that $|\tilde{J}| = 0$ (the bluest horizontal curve on the left plot) is 0, which means that even for extreme sparsity ($k = 10$) and a relatively high m/n rate of 0.9, the support is never predicted as perfectly stable for $\alpha = \infty$ in this experiment. We can observe as a rule of thumb, that a support excess of $|\tilde{J}| \approx k$ is much more likely. In comparison, ℓ_2 recovery provides a much more likely perfect support stability for k not too large and the expected size of \tilde{J}_2 increases slower with k .

4 Take-away messages

Under the small noise assumption, Theorem 1 provides a closed form solution for the convex program $(\mathcal{P}_\infty^\tau(y))$ and notably predicts its support. To our knowledge this is the first guarantee of this type, that may be used to explain the lack of support stability in quantized compressed sensing. This work constitutes a first attempt to apply the framework of dual certificates to provide theoretical stability guarantees for linear inverse problems by solving convex programs where both the data fidelity and the regularizer are convex but non-smooth. It lays foundation for future generalizations, e.g., following the ideas of [13].

References

- [1] Francis Bach. Consistency of the group Lasso and multiple kernel learning. *The Journal of Machine Learning Research*, 9:1179–1225, 2007.
- [2] Francis Bach. Consistency of trace norm minimization. *Journal of Machine Learning Research*, 8:1019–1048, 2008.
- [3] Petros T. Boufounos, Laurent Jacques, Felix Kraher, and Rayan Saab. Quantization and Compressive Sensing. In *Compressed Sensing and its Applications*, pages 193–237. 2015.
- [4] Alfred M. Bruckstein, David L. Donoho, and Michael Elad. From Sparse Solutions of Systems of Equations to Sparse Modeling of Signals and Images. *SIAM Review*, 51(1):34–81, feb 2009.
- [5] Emmanuel J. Candès, Justin K. Romberg, and Terence Tao. Stable signal recovery from incomplete and inaccurate measurements. *Communications on Pure and Applied Mathematics*, 59(8):1207–1223, aug 2006.
- [6] Scott Shaobing Chen, David L. Donoho, and Michael A. Saunders. Atomic Decomposition by Basis Pursuit. *SIAM Journal on Scientific Computing*, 20(1):33–61, jan 1998.
- [7] Vincent Duval and Gabriel Peyré. Exact Support Recovery for Sparse Spikes Deconvolution. *Foundations of Computational Mathematics*, 15(5):1315–1355, oct 2015.
- [8] Jean Jacques Fuchs. On sparse representations in arbitrary redundant bases. *IEEE Transactions on Information Theory*, 50(6):1341–1344, 2004.
- [9] Laurent Jacques. On the optimality of a L1/L1 solver for sparse signal recovery from sparsely corrupted compressive measurements. *arXiv preprint arXiv:1303.5097*, pages 1–4, mar 2013.
- [10] Laurent Jacques, David K. Hammond, and Jalal M. Fadili. Dequantizing Compressed Sensing: When Oversampling and Non-Gaussian Constraints Combine. *IEEE Transactions on Information Theory*, 57(1):559–571, jan 2011.
- [11] Amirafshar Moshtaghpour, Laurent Jacques, Valerio Cambareri, Kévin Degraux, and Christophe De Vleeschouwer. Consistent Basis Pursuit for Signal and Matrix Estimates in Quantized Compressed Sensing. *IEEE Signal Processing Letters*, 23(1):25–29, jan 2016.
- [12] Christoph Studer, Patrick Kuppinger, Graeme Pope, and Helmut Bölcskei. Recovery of Sparsely Corrupted Signals. *IEEE Transactions on Information Theory*, 58(5):3115–3130, may 2012.
- [13] Samuel Vaïter, Gabriel Peyré, and Jalal Fadili. Low Complexity Regularization of Linear Inverse Problems. In *arXiv preprint arXiv:1407.1598*, pages 103–153. jul 2015.

Low Rank and Group-Average Sparsity Driven Convex Optimization for Direct Exoplanets Imaging

Benoît Pairet¹, Laurent Jacques¹, Carlos A. Gomez Gonzalez², Olivier Absil²

¹ISPGROUP/ICTEAM, Université catholique de Louvain, Belgium,

² Institut d'Astrophysique et de Géophysique, Université de Liège, Belgium.

Abstract— Direct exoplanets imaging is a challenging task for two main reasons. First, the host star is several order of magnitude brighter than exoplanets. Second, the great distance between us and the star system makes the exoplanets-star angular distance very small. Furthermore, imperfections on the optics along with atmospheric disturbances create *speckles* that look like planets. Ten years ago, astronomers introduced Angular Differential Imaging (ADI) that uses the rotation of the Earth to add diversity to the data. Signal processing then allows to separate the starlight from the planet's signal. After that, a detection signal to noise ratio (SNR) is computed. We present here a sparsity driven convex optimisation program along with a new SNR map that beat the state of the art methods for small angular separation.

1 Introduction

In the emerging field of Exoplanets survey [8], direct imaging of exoplanets allows astrophysicists to study their properties such as atmosphere composition [11] or trajectories [19]. Only 3%² of all confirmed exoplanets have been directly observed. This is because exoplanets are faint objects located in close vicinity to their host star, Earth-like planets are typically 10^{-10} fainter than their host and have an apparent separation of 0.1 arcsec [18]. Observing them requires (i) high resolution telescope to be able to separate planet's signal from starlight and (ii) a *coronagraph* that "hides" the star either with a physical mask (Lyot coronagraph) or more recently with a phase mask (among which, the vortex coronagraph [16]). Ground based telescopes offer the highest resolution but suffer from the atmosphere perturbation of the wavefront which duplicates the star's psf on several quasi static spots, called *speckles*, that look like planets. Observing at wavelength λ with a pupil of diameter D , Adaptive Optics (AO) allows to reach performances close to diffraction limit ($\approx \lambda/D$) but does not remove all such speckles [7].

Angular Differential Imaging (ADI) leverages the fact that those speckles remain almost constant during a night of observation: astronomers take several snapshots (varying from several tenths to several thousands) of a targeted star without compensating the rotation of the Earth. Thus a potential planets will follow a circular trajectories on the image stack but the star and the speckles will remain quasi static [15]. It is important to note that this trajectory is induced by the rotation of the Earth and is not due to the rotation of the planet around its star. Thus we know the angular difference between two frames. The post processing of ADI sequences is done in two steps (i) the background is estimated and subtracted from the sequence and then (ii) the residual images are rotated and *collapsed*, i.e., summed up, into one final frame, either with temporal mean or temporal median. The idea is that the remaining starlight and speckles will add up incoherently and average close to zero whilst the planet's signal will be aligned and have a (hopefully

large) non-zero value on that final frame. Methods to estimate the background include temporal median [15], LOCI [13] and PCA [20], [2]. More recently, LLSG [10] enforces sparsity on the foreground before collapsing. After this processing, a third step is required to perform the detection. Whatever the method, the separation is never perfect and we still have to perform a detection. Visual detection is sometimes possible but high-contrast imaging astronomers can rely on a SNR map to confirm the detection. It is built as follows: for each pixel, the pixels intensity in the surrounding circle of diameter λ/D is compared to the pixels intensity of all the other such circles at the same radial distance from the center with a two sample t-test [17]. We will refer to it as SNR_t .

We propose here a convex optimisation program to separate the starlight from the planet's signal (steps (i) and (ii)). We promote sparsity on the image obtained *after collapsing*, i.e., *on the final frame*. That is, we promote *group sparsity*, in the same idea of ℓ_{21} -norm penalties [12],[3], with the groups being all possible trajectories. In other words, we seek for a foreground such that only a few trajectories have a non-zero mean.

The enforced sparsity of LLSG and our method can lead to division by zero and thus to infinite SNR if there is only one non-zero pixel on a given radius. Thus we propose another detection map. It is based on the following. Once we remove the background and align residual images, the planet's intensity varies little compared to the residual starlight and speckles intensity. If we compute the squared ℓ_2 -norm and the estimated variance $\hat{\sigma}^2$ of a given trajectory, the ratio between the two is always close to one *unless there is a planet on that trajectory*. That is, the ratio $\hat{\mu}^2/\hat{\sigma}^2$ is large for a given trajectory only if there is a planet on that trajectory, with $\hat{\mu}$ the estimated mean.

The experiments performed on both real and synthetic data show that the proposed optimisation program and the $\hat{\mu}^2/\hat{\sigma}^2$ detection map beat the state of the art when the planet lies in the close vicinity of the star.

2 Proposed method

We consider the following model for $x(\mathbf{p}, t)$, the underlying light intensity of the star and the planet, $\mathbf{p}, \mathbf{p}_* \in \mathbb{R}^2$, $\mathbf{p}_0 : \mathbb{R} \rightarrow \mathbb{R}^2$:

$$x(\mathbf{p}, t) = I_* \delta^{(2)}(\mathbf{p} - \mathbf{p}_*) + I_0 \delta^{(2)}(\mathbf{p} - \mathbf{p}_0(t)), \quad (1)$$

where $I_* > 0$ and $I_0 > 0$ are the intensities of the star and the planet respectively, $\mathbf{p}_* \in \mathbb{R}^2$ the position of the star and $\mathbf{p}_0(t) \in \mathbb{R}^2$ the position of the planet. It is given by $\mathbf{p}_0(t) = \mathbf{p}_* + \mathbf{r}(t)$ with $\mathbf{r}(t) = R(\cos \theta(t), \sin \theta(t))^\top$, where R is the radial distance between the star and the planet and $\theta(t) = \omega t + \phi$, $\omega, \phi \in \mathbb{R}$. We observe

$$y(\mathbf{p}, t) = \mathcal{C}(\varphi * x(\mathbf{p}, t)) \cong (\varphi * x)(\mathbf{p}, t) + n_s(\mathbf{p}, t),$$

where $\mathcal{C}(\cdot)$ is an unknown corruption process, $*$ is the spatial convolution, and φ , the telescope point spread function (psf).

We thank the supercomputing facilities (CISM/UCL) funded by FRS-FNRS, for their computational resources. LJ and BP are funded by the Belgian FNRS. Part of this study is funded by the AlterSense project (MIS-FNRS).

²<http://http://exoplanet.eu/>

And then we discretise spatially and temporally, in a $T \times n \times n$ cube that can be reshaped into a $T \times N$ matrix, $N = n^2$.

LLSG separates the observed signal $\mathbf{Y} \in \mathbb{R}^{T \times N}$ into three parts: a low rank part \mathbf{L} for the star and speckle, a sparse term \mathbf{S} for the planet, and a noise term for the residual. Although the problem is convex, LLSG solves it in a non convex fashion for which convergence is not guaranteed. The method we propose here is based on a similar decomposition. Instead of enforcing sparsity on \mathbf{S} , we enforce that only a small number of trajectories have a non-zero mean. Each pixel in \mathbf{S} belongs to one and only one circular trajectory. An example of such trajectories is displayed on Fig. (1). The symbol \mathcal{G} represents the set of trajectories, $G = |\mathcal{G}|$ is the number of trajectories, and \mathbf{u}_g for $\mathbf{U} \in \mathbb{R}^{T \times N}$, $\mathbf{u}_g \in \mathbb{R}^{|g|}$ is the restriction of \mathbf{U} to the trajectory $g \in \mathcal{G}$. By construction, we have that $g \cap g' = \emptyset$ for $g, g' \in \mathcal{G}$, $g \neq g'$. The proposed convex program is

$$\min_{\mathbf{L}, \mathbf{S} \in \mathbb{R}^{T \times N}} \lambda \|\mathbf{L}\|_* + \|\Phi^\top \text{vec}(\mathbf{S})\|_1 \quad (\mathcal{P})$$

$$\text{s.t.} \quad \mathbf{L} + \mathbf{S} = \mathbf{Y} \quad (\mathcal{C1})$$

$$\|\mathbf{S}\|_2 \leq \tau_s \quad (\mathcal{C2})$$

where $\lambda, \tau_s \in \mathbb{R}$, $\Phi^\top = (\phi_{g_1}, \dots, \phi_{g_G})^\top \in \mathbb{R}^{G \times TN}$, $(\phi_g)_i = 1/\sqrt{|g|}$ if $i \in g$ and 0 otherwise. We introduce $\mathcal{C}_1 = \{\mathbf{L}, \mathbf{S} \mid \mathbf{L} + \mathbf{S} = \mathbf{Y}\}$ and $\mathcal{C}_2 = \{\mathbf{U} \mid \|\mathbf{U}\|_2 \leq \tau_s\}$. The nuclear norm $\|\cdot\|_*$ will enforce a low rank structure, *i.e.*, absorb the static part of the data, while $\|\cdot\|_1$ will enforce sparsity on the number of "active" trajectories. We write \mathcal{P} as an unconstrained problem using the indicator function $i_{\mathcal{C}_j}(\mathbf{U})$ that equals 0 if $\mathbf{U} \in \mathcal{C}_j$ and $+\infty$ otherwise, $j = 1, 2$. Since Φ^\top is semi-orthogonal, *i.e.*, $\Phi^\top \Phi = \nu \mathbf{I}$ (here with $\nu = 1$), we can use the property of the proximal operators and write $\text{prox}_{\|\Phi^\top \cdot\|_1}(v) = x + \Phi(\text{prox}_{\|\cdot\|_1}(\Phi^\top v) - \Phi^\top x)$ [6]. We solve this problem with the PPXA algorithm [5].

For the detection, we have made the following empirical observation: once the low rank structure is removed from the data, the ratio between the squared ℓ_2 -norm and the computed variance for each trajectory is $\frac{\|\mathbf{s}_g\|_2^2}{\|\mathbf{s}_g\|_2^2 - \hat{\mu}_g^2} \approx 1$ unless there is a planet on this trajectory. That can be seen on Fig. (1). That means that, unless there is a planet on trajectory g , $\hat{\sigma}_g^2 \gg \hat{\mu}_g^2$. Based on this, we propose to perform the detection on the $\frac{\hat{\mu}_g^2}{\hat{\sigma}_g^2}$ -map instead of the previously mentioned SNR_t . We note also that the ratio $\frac{\hat{\mu}}{\hat{\sigma}}$ is sometimes used as an SNR measure.

3 Experiments and discussion

The parameters λ and τ_s are to be set by the user. We propose a value for both of them based on their role in the program. The goal of λ is that the two terms in the minimisation are of the same order. For given \mathbf{S}_0 and \mathbf{L}_0 close to optimal, it should be set such that $\lambda \approx \|\Phi^\top \text{vec}(\mathbf{S}_0)\|_1 / \|\mathbf{L}_0\|_*$. The role of τ_s is to keep the amplitude of \mathbf{S} relatively small and is again a matter of order of magnitude, we set $\tau_s = \|\mathbf{S}_0\|_2$. The PCA approach already gives a good hint of what the solution will look like. Thus we propose to take \mathbf{L}_0 and \mathbf{S}_0 as the output of the PCA method. The dependency on the number of principal components (PC's) was tested on real data with a number of PC's ranging from 5 to 25. We compared the peak values of pixels near the planet and the other pixels on the $\hat{\mu}^2/\hat{\sigma}^2$ -map. In all cases, we obtained a ratio above 100.

We consider the observations of the β pic star [14] done at the VLT-NACO telescope in its AGPM coronagraphic mode [1] on January 2013. We first remove the known planet by means

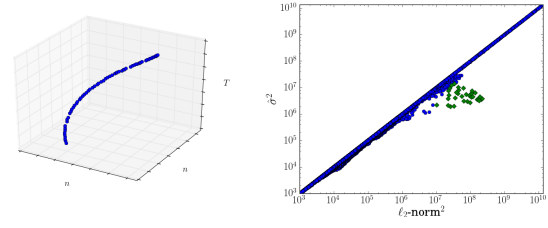


Fig. (1): Left: Example of a group-trajectory. Right: ℓ_2 -norm vs. variance, along trajectories. We can see (green, diamond) a deviation when there is a planet.

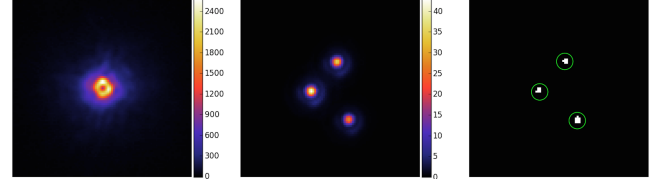


Fig. (2): Results of the proposed method on β pic with multiple fake companions. Left: initial image, containing the star and the fake companions. Center: the ground truth. Right: binary planets detection based on the $\hat{\mu}^2/\hat{\sigma}^2$ -map.

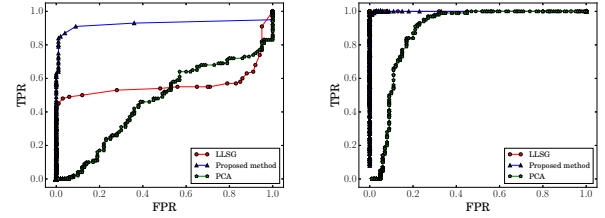


Fig. (3): ROC curves for medium intensity at radius between 2 and 3 λ/D (left) and medium intensity at radius between 3 and 4 λ/D (right).

of the negative companion injection method [4], [1]. Once the data set is planet-free, we can build synthetic data by injecting fake companions at given positions and intensity. The steps above can be done easily with the Vortex Image Processing (VIP) toolbox³ [9]. As in [10], we compare algorithms with a receiver operating characteristic (ROC) curve. Given a detection threshold, we say there is a true positive (TP) if there is one pixel in a λ/D diameter wide area around the planet's position that is above the threshold. If there is one pixel above that threshold outside this area, we say there is a false positive (FP). We repeat 100 times the experiments and compute the true positive rate (TPR) and the false positive rate (FPR) for a given radius and intensity. We compare the proposed method, with the $\frac{\hat{\mu}^2}{\hat{\sigma}^2}$ -map for detection to LLSG with SNR_t .

Then we inject multiple fake companions and applied the proposed method. Fig. (2) shows the initial image, the ground truth and the detection results with the proposed method. Fig. (3) displays the ROC curve for a radial distance between 2 and 5 λ/D and intensity of 10^{-3} of the star's peak intensity (with the coronagraph). We can see that the proposed method improves the detection rate in the close vicinity of the star.

4 Conclusion

We have proposed a convex program to separate planet's signal from starlight and speckle. In addition, we introduced a detection map based on the difference of temporal behaviour between planet's signal and residual noise on the sparse component. The combination of the convex program and the detection map can beat the state of the art method in the case of a small angular separation between the planet and the star.

³<https://github.com/vortex-exoplanet/VIP>

References

- [1] Olivier Absil, Julien Milli, Dimitri Mawet, A-M Lagrange, Julien Girard, Gaël Chauvin, Anthony Boccaletti, Christian Delacroix, and Jean Surdej. Searching for companions down to 2 au from β pictoris using the l-band agpm coronagraph on vlt/naco. *Astronomy & Astrophysics*, 559:L12, 2013.
- [2] Adam Amara and Sascha P Quanz. Pynpoint: an image processing package for finding exoplanets. *Monthly Notices of the Royal Astronomical Society*, 427(2):948–955, 2012.
- [3] Francis Bach, Rodolphe Jenatton, Julien Mairal, Guillaume Obozinski, et al. Convex optimization with sparsity-inducing norms. *Optimization for Machine Learning*, 5, 2011.
- [4] M Bonnefoy, A-M Lagrange, A Boccaletti, G Chauvin, D Apai, F Allard, D Ehrenreich, JHV Girard, D Mouillet, D Rouan, et al. High angular resolution detection of β pictoris b at 2.18 μm . *Astronomy & Astrophysics*, 528:L15, 2011.
- [5] Patrick L Combettes and Jean-Christophe Pesquet. A proximal decomposition method for solving convex variational inverse problems. *Inverse problems*, 24(6):065014, 2008.
- [6] Patrick L Combettes and Jean-Christophe Pesquet. Proximal splitting methods in signal processing. In *Fixed-point algorithms for inverse problems in science and engineering*, pages 185–212. Springer, 2011.
- [7] Gaspard Duchêne. High-angular resolution imaging of disks and planets. *New Astronomy Reviews*, 52(2):117–144, 2008.
- [8] Debra A Fischer, Andrew W Howard, Greg P Laughlin, Bruce Macintosh, Survrath Mahadevan, Johannes Sahlmann, and Jennifer C Yee. Exoplanet detection techniques. *arXiv preprint arXiv:1505.06869*, 2015.
- [9] C. A. Gomez Gonzalez, O. Wertz, V. Christiaens, O. Absil, and D. Mawet. VIP: Vortex Image Processing pipeline for high-contrast direct imaging of exoplanets. Astrophysics Source Code Library, March 2016.
- [10] CA Gomez Gonzalez, O Absil, PA Absil, M Van Droogenbroeck, D Mawet, and J Surdej. Low-rank plus sparse decomposition for exoplanet detection in direct-imaging adi sequences. *A&A*, 2016.
- [11] Quinn M Konopacky, Travis S Barman, Bruce A Macintosh, and Christian Marois. Detection of carbon monoxide and water absorption lines in an exoplanet atmosphere. *Science*, 339(6126):1398–1401, 2013.
- [12] Matthieu Kowalski and Bruno Torrèsani. Sparsity and persistence: mixed norms provide simple signal models with dependent coefficients. *Signal, image and video processing*, 3(3):251–264, 2009.
- [13] David Lafrenière, Christian Marois, René Doyon, Daniel Nadeau, and Étienne Artigau. A new algorithm for point-spread function subtraction in high-contrast imaging: A demonstration with angular differential imaging. *The Astrophysical Journal*, 660(1):770, 2007.
- [14] A-M Lagrange, M Bonnefoy, G Chauvin, D Apai, D Ehrenreich, A Boccaletti, D Gratadour, D Rouan, D Mouillet, S Lacour, et al. A giant planet imaged in the disk of the young star β pictoris. *Science*, 329(5987):57–59, 2010.
- [15] Christian Marois, David Lafreniere, René Doyon, Bruce Macintosh, and Daniel Nadeau. Angular differential imaging: A powerful high-contrast imaging technique. *The Astrophysical Journal*, 641(1):556, 2006.
- [16] D Mawet, Pierre Riaud, Olivier Absil, and Jean Surdej. Annular groove phase mask coronagraph. *The Astrophysical Journal*, 633(2):1191, 2005.
- [17] Dimitri Mawet, Julien Milli, Zahed Wahhaj, Didier Pelat, Olivier Absil, Christian Delacroix, Anthony Boccaletti, Markus Kasper, Matthew Kenworthy, Christian Marois, et al. Fundamental limitations of high contrast imaging set by small sample statistics. *The Astrophysical Journal*, 792(2):97, 2014.
- [18] Dimitri Mawet, Laurent Pueyo, Peter Lawson, Laurent Mugnier, Wesley Traub, Anthony Boccaletti, John T Trauger, Szymon Gladysz, Eugene Serabyn, Julien Milli, et al. Review of small-angle coronagraphic techniques in the wake of ground-based second-generation adaptive optics systems. In *SPIE Astronomical Telescopes+ Instrumentation*, pages 844204–844204. International Society for Optics and Photonics, 2012.
- [19] L Pueyo, R Soummer, J Hoffmann, R Oppenheimer, JR Graham, N Zimmerman, C Zhai, JK Wallace, F Vescelus, A Veicht, et al. Reconnaissance of the hr 8799 exosolar system. ii. astrometry and orbital motion. *The Astrophysical Journal*, 803(1):31, 2015.
- [20] Rémi Soummer, Laurent Pueyo, and James Larkin. Detection and characterization of exoplanets and disks using projections on karhunen-loève eigenimages. *The Astrophysical Journal Letters*, 755(2):L28, 2012.

A fast algorithm for high-order sparse linear prediction

Tobias Lindstrøm Jensen¹, Daniele Giacobello², Toon van Waterschoot³, Mads Græsbøll Christensen⁴

¹Signal and Information Processing, Aalborg Universitet, Denmark

²Codec Technologies R&D, DTS Inc., Calabasas, CA, USA

³Department of Electrical Engineering (ESAT-STADIUS/ETC), KU Leuven, Belgium

⁴Audio Analysis Lab., AD:MT, Aalborg Universitet, Denmark

tlj@es.aau.dk, giacobello@ieee.org, toon.vanwaterschoot@esat.kuleuven.be, mgc@create.aau.dk

Abstract— Using a sparsity promoting convex penalty function on high-order linear prediction coefficients and residuals addresses some inherent limitations of standard linear prediction methods. This formulation, however, is computationally more demanding which may limit its use, in particular for embedded signal processing. We show that the matrix structures associated with an alternating direction method of multipliers algorithm for solving the high-order sparse linear prediction problem are more tractable than the matrix structures for interior-point methods and that a few tens of iterations suffice to achieve similar results, in terms of prediction gain, as an interior-point method.

1 Background

Sparse linear prediction (SLP) [1, 2] revisits the linear prediction (LP) framework [3, 4] in light of the developments that took place in the recent years in the field of convex optimization and sparse representations. SLP has proved to be an interesting alternative to classic LP by allowing better statistical models and more meaningful signal representation finding its way in various applications, e.g., [5–7]. While software packages like CVX+SeDuMi [8, 9] allow to quickly reproduce the SLP algorithm [10, 11], serious efforts to make SLP and other algorithms requiring convex optimization run faster and, possibly, in a real-time platform, is a current matter of research in signal processing [12, 13].

LP provides a compact representation for the signal $x[t]$ as:

$$x[t] = \sum_{n=1}^N \alpha_n x[t-n] + r[t], \quad (1)$$

where $\alpha = [\alpha_n]_{n=1}^N$ are the prediction coefficients and $r[t]$ is the prediction error. A common route for estimation of α is via:

$$\underset{\alpha}{\text{minimize}} \|x - X\alpha\|_p^2 \quad (2)$$

where $\|\cdot\|_p$ is the p -norm and we here are working with a vectorized version of (1) over a certain frame. With $p = 2$, a closed-form solution can be obtained as $\alpha = (X^T X)^{-1} X^T x$.

The LP model finds one of its most successful applications in speech and audio processing [4]. However, particularly in speech processing, traditional LP fails to provide a general framework when signal redundancies are present at different time intervals. This is the case where a given segment x has

short-term and long-term redundancies and cannot be represented by a simple linear prediction model with a limited number of taps. Traditional approaches tend to represent short-term redundancies using traditional LP and represent long-term redundancies by applying a so-called long-term predictor (LTP) with a very limited number of taps clustered around the *pitch period* of the speech or audio signal. Since the combination of these two filters is a high-order sparse predictor, a more effective way to model these types of signal was shown by increasing the order of the predictor and apply a sparsity criterion on its coefficients [14]. In addition, by applying the 1-norm also on the residual, both modeling and coding advantages can be achieved [2]. A SLP formulation then becomes:

$$\underset{\alpha}{\text{minimize}} f(\alpha) = \|x - X\alpha\|_1 + \gamma\|\alpha\|_1. \quad (3)$$

Solving (3) is however more complex than traditional 2-norm based LP and state-of-the-art methods for real-time optimization have, to some extent, focused on code generation based on interior-point (IP) methods [12, 15]. The most significant matrix structure these methods exploit is sparsity, i.e., for example at code-generation exploiting $[A0][x^T y^T]^T = Ax$ such that we avoid computing $0 \cdot y$. However, many applications in signal processing, including the problem (3), are dense. Further, for IP methods the main bulk of work is to solve a linear system of equations in each iteration where additional weighting matrices are introduced and in particular diagonal matrices for linear programming. Such diagonal matrices often do not allow the possibility of faster direct methods for solving a linear system [16]. Specifically, IP methods for the SLP problem (3) would have cubic per iteration time complexity [17]. In particular, the introduction of the diagonal weighting matrix for the SLP problem prohibits the exploration of Toeplitz structure since such matrices do not have a low displacement rank.

Instead of using an IP method we consider an alternating method of multipliers (ADMM) algorithm. The problem in (3) can be recast as the following least absolute deviation problem

$$\underset{\alpha}{\text{minimize}} \left\| \begin{bmatrix} \gamma I \\ -X \end{bmatrix} \alpha - \begin{bmatrix} 0 \\ -x \end{bmatrix} \right\|_1. \quad (4)$$

for which the ADMM algorithm is [18]:

$$\begin{aligned} \alpha^{(k+1)} &= (X^T X + \gamma^2 I)^{-1} [\gamma I \quad -X^T] (y^{(k)} + \begin{bmatrix} 0 \\ -x \end{bmatrix} - u^{(k)}) \\ e^{(k+1)} &= x - X\alpha^{(k+1)} \\ y^{(k+1)} &= S_{1/\rho} \left(\begin{bmatrix} \gamma\alpha^{(k+1)} \\ e^{(k+1)} \end{bmatrix} + u^{(k)} \right) \\ u^{(k+1)} &= u^{(k)} + \begin{bmatrix} \gamma\alpha^{(k+1)} \\ e^{(k+1)} \end{bmatrix} - y^{(k+1)}. \end{aligned}$$

The work of T. L. Jensen is supported by The Danish Council for Independent Research, Technology and Production Sciences, grant number 4005-00122. The work of T. van Waterschoot is supported by the KU Leuven Impulse Fund, grant number IMP/14/037.

Notice that in this ADMM formulation there is no reweighting of X (or $X^T X$) and we may then use fast (and superfast) methods for solving the linear Toeplitz system [19, 20].

2 Numerical Simulations

For the numerical simulations we will focus on the application of SLP in speech processing, however, we will apply a objective measures and the results is then extendable to other application scenarios. In particular, we investigated the prediction gain performance as a function of the number of iterations of the presented ADMM algorithm and the associated computational cost assessed by timing.

We processed the vowel and semivowel phones [21] from the TIMIT database ($f_s = 16\text{kHz}$), belonging to 3696 sentences from 462 speakers. We chose the ones of duration of at least 640 samples (40 ms) for a total of about 40,000 voiced speech frames. In this investigation, we extend the analysis in [22] by investigating the prediction gain from the ADMM solution with a different number of iterations and compare with the IP solution obtained through the CVX+SeDuMi interface and solver. The regularization parameter $\gamma = 0.12$ was obtained through a modified L-curve analysis [23] by using all except 50 frames picked randomly that will be used as a test set. We chose $N = 250$ such that it is possible to cover the pitch lag range $T_p \in [34, 231]$ as done in commercial speech codecs like the wideband version of the Adaptive Multi-Rate codec (AMR-WB [24]). The results for the test set is shown in Figure 1. We can see that at 30 iterations the mean value of the IP solution falls within the 95% confidence interval of the ADMM solution, proving that the two algorithms exhibit statistically the same performance.

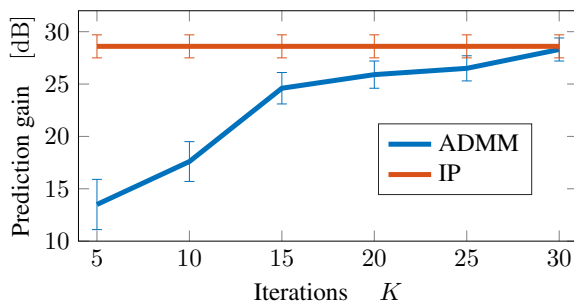


Figure 1: Average prediction gains for a fixed number of iterations for the ADMM solution. A 95% confidence interval is shown. The IP solutions as returned by CVX+SeDuMi is independent of the fixed number of iterations K but shown for the ease of comparison.

Using a C++ implementation, we can run $k = 30$ iterations on a standard laptop in approximately 1.7ms in double precision. This is an indication that an ADMM algorithm for the SLP problem may be viable for real-time and embedded optimization but further algorithm design investigations are necessary to address this possibility. We note that we are applying the ADMM algorithm in its straightforward form but several variants and extensions may be useful for solving the sparse linear prediction problem efficiently and should be considered for further investigations. On particular choice is a preconditioned ADMM where the algorithm does not involve solving a linear system of equation [25].

References

- [1] D. Giacobello, M. G. Christensen, J. Dahl, S. H. Jensen, and M. Moonen, "Sparse linear predictors for speech processing," in *Proc. INTERSPEECH*, pp. 1353–1356, 2008.
- [2] D. Giacobello, M. G. Christensen, M. N. Murthi, S. H. Jensen, and M. Moonen, "Sparse linear prediction and its applications to speech processing," *IEEE Trans. Audio, Speech, Language Process.*, vol. 20, no. 5, pp. 1644–1657, 2012.
- [3] J. Makhoul, "Linear prediction: A tutorial review," *Proc. IEEE*, vol. 63, no. 4, pp. 561–580, 1975.
- [4] T. Bäckström, *Linear predictive modeling of speech: constraints and line spectrum pair decomposition*, Helsinki University of Technology, 2004.
- [5] D. Angelosante, "Sparse regressions for joint segmentation and linear prediction," in *Proc. ICASSP*, pp. 335–339, 2014.
- [6] A. Jukic, T. van Waterschoot, T. Gerkmann, and S. Doclo, "Multi-channel linear prediction-based speech dereverberation with sparse priors," *IEEE/ACM Trans. Audio, Speech, Language Process.*, vol. 23, no. 9, pp. 1509–1520, 2015.
- [7] J. Koloda, J. Østergaard, S.H. Jensen, V. Sanchez, and A.M. Peinado, "Sequential error concealment for video/images by sparse linear prediction," *IEEE Trans. Multimedia*, vol. 15, no. 4, pp. 957–969, 2013.
- [8] M. Grant and S. Boyd, "CVX: Matlab software for disciplined convex programming, v. 1.21," <http://cvxr.com/cvx/>, 2011.
- [9] J. F. Sturm, "Using SeDuMi 1.02, a MATLAB toolbox for optimization over symmetric cones," *Optim. Methods Software*, vol. 11-12, pp. 625–653, 1999.
- [10] D. Giacobello, M. G. Christensen, M. N. Murthi, S. H. Jensen, and M. Moonen, "Speech coding based on sparse linear prediction," in *Proc. EUSIPCO*, pp. 2524–2528, 2009.
- [11] D. Giacobello, T. van Waterschoot, M. G. Christensen, S. H. Jensen, and M. Moonen, "High-order sparse linear predictors for audio processing," in *Proc. EUSIPCO*, pp. 234–238, 2010.
- [12] J. Mattingley and S. Boyd, "Real-time convex optimization in signal processing," *IEEE Signal Process. Magazine*, vol. 27, no. 3, pp. 50–61, 2010.
- [13] B. Defraene, T. van Waterschoot, H. J. Ferreau, M. Diehl, and M. Moonen, "Real-time perception-based clipping of audio signals using convex optimization," *IEEE Trans. Audio, Speech, Language Process.*, vol. 20, no. 10, pp. 2657–2671, 2012.
- [14] D. Giacobello, M. G. Christensen, J. Dahl, S. H. Jensen, and M. Moonen, "Joint estimation of short-term and long-term predictors in speech coders," in *Proc. ICASSP*, pp. 4109–4112, 2009.
- [15] A. Domahidi, E. Chu, and S. Boyd, "ECOS: An SOCP solver for embedded systems," in *Proc. EUSIPCO*, pp. 3071–3076, 2013.
- [16] D. O'Connor and L. Vandenberghe, "Primal-dual decomposition by operator splitting and applications to image deblurring," *SIAM J. Imag. Sci.*, vol. 7, pp. 1724–1754, 2014.
- [17] T. L. Jensen, D. Giacobello, M. G. Christensen, S. H. Jensen, and M. Moonen, "Real-time implementations of sparse linear prediction for speech processing," in *Proc. ICASSP*, pp. 8184–8188, 2013.

- [18] T. L. Jensen, D. Giacobello, T. van Waterschoot, and M. G. Christensen, "Computation analysis of a fast algorithm for high-order sparse linear prediction," in *Proc. EUSIPCO*, 2016.
- [19] R. R. Bitmead and B. D.O. Anderson, "Asymptotically fast solution of Toeplitz and related systems of linear equations," *Linear Algebra Appl.*, vol. 34, pp. 103–116, 1980.
- [20] G. S. Ammar and W. B. Gragg, "Superfast solution of real positive definite Toeplitz systems," *SIAM J. Matrix Analysis. Appl.*, vol. 9, no. 1, pp. 61–76, 1988.
- [21] A. K. Halberstadt and J. R. Glass, "Heterogeneous acoustic measurements for phonetic classification," in *EUROSPEECH*, 1997.
- [22] T. L. Jensen, D. Giacobello, T. van Waterschoot, and M. G. Christensen, "Fast algorithms for high-order sparse linear prediction with applications to speech processing," *Speech Comm.*, vol. 76, pp. 143–156, 2016.
- [23] P. C. Hansen and D. P. O'Leary, "The use of the L-curve in the regularization of discrete ill-posed problems," *SIAM J. Sci. Comput.*, vol. 14, no. 6, pp. 1487–1503, 1993.
- [24] B. Bessette, R. Salami, R. Lefebvre, M. Jelinek, J. Rotola-Pukkila, J. Vainio, H. Mikkola, and K. Jarvinen, "The adaptive multirate wideband speech codec (AMR-WB)," *IEEE Trans. Speech Audio Process.*, vol. 10, no. 8, pp. 620–636, 2002.
- [25] A. Chambolle and T. Pock, "A first-order primal-dual algorithm for convex problems with applications to imaging," *J. Math. Imag. Vis.*, vol. 40, no. 1, pp. 120–145, 2011.

Compressive Hyperspectral Imaging with Fourier Transform Interferometry

A. Moshtaghpour¹, K. Degraux¹, V. Cambareri¹, A. Gonzalez¹, M. Roblin², L. Jacques¹, and P. Antoine².

¹ ICTEAM, Université catholique de Louvain, Louvain-la-Neuve, Belgium.

² Lambda-X SA, Rue de l'Industrie 37, Nivelles, Belgium.

Abstract— This paper studies the fast acquisition of Hyper-Spectral (HS) data using Fourier transform interferometry (FTI). FTI has emerged as a promising alternative to capture, at a very high resolution, the wavelength coordinate as well as the spatial domain of the HS volume. A drawback of the conventional FTI devices is a typically slow acquisition process. In this paper we develop a compressive sensing (CS) framework for FTI. By exploiting the sparsity of the target HS data in a 3-D wavelet basis we show how the actual HS data can be retrieved from partial FTI measurements. Furthermore, we develop an alternative sampling strategy, *i.e.*, a variable density rather than uniform sampling scheme to boost the acquisition accuracy. Extensive simulations show that (i) the proposed method is applicable to realistic FTI and (ii) the variable density sampling scheme is more accurate than conventional uniform sampling.

1 Introduction

Nowadays, many scientific disciplines increasingly rely on the analysis of Hyper-Spectral (HS) data volumes, *i.e.*, the description of a scene (*e.g.*, a biological sample) both by its spatial and spectral content, thus describing the light intensity in its spatial and wavelength domains. In particular, HS imaging has been recognized as a possibility to distinguish specific biological elements, *e.g.*, in fluorescence spectroscopy [1].

A key step for studying an (high-dimensional) HS data is to achieve an accurate acquisition in the first place. HS acquisition methods typically operate by either spatial or spectral scanning¹. We here focus on spectral scanning methods, most of which are based on direct observation, *e.g.*, by using spectral filters on the incoming light. However, direct spectral scanning methods often result in imaging artifacts due to the change of the material in the observed scene and, due to the filtering elements, suffer from low light transmittance and therefore limited signal-to-noise (SNR) ratio. On the other hands, indirect methods such as Fourier transform interferometers (FTI) [3] avoid such issues: since FTI acquires indirect Fourier-domain measurements of HS data, it can achieve higher spectral resolution without reducing the SNR, conversely to direct methods.

However, inspired by the need of biological applications, *i.e.*, fast and high-resolution HS image, conventional FTI devices are not completely reliable. One way to cope with this drawback is to record the FTI measurement at a few coordinates in the Fourier domain, *i.e.*, partial Fourier sampling, and resorting to the theory of compressed sensing (CS) which makes the reconstruction of the target HS data feasible, if they follow a low-complexity model [4, 5, 6]. To this end, we adopt a sparse model for the HS data in the joint spatial-spectral domain by using the Kronecker product of two Haar wavelet bases [7]. As for the sampling scheme, we start with a uniform sampling strategy where the Fourier-domain coordinates, corresponding to mirror positions in the optical setup, are selected uniformly at random. Nevertheless, since low-scale wavelets and low-frequency components are highly coherent, it is well-

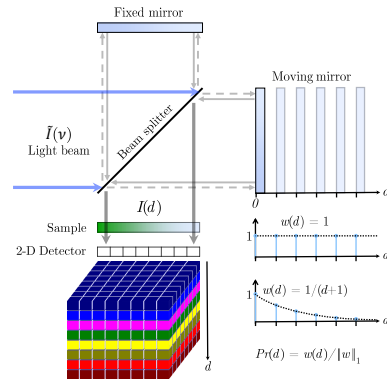


Figure 1: Operating principle of FTI.

investigated in [8, 9, 10] that variable density sampling strategies result in superior reconstruction. Inspired by these results, we also validate the performances of variable density sampling. Finally, to recover the true HS data we develop a convex minimization problem which is solved by the Douglas-Rachford proximal algorithm introduced in [11].

2 Fourier Transform Interferometry

Conventional FTI, we call it here *Nyquist FTI*, works on the principle of a Michelson interferometer with a moving mirror. As shown in Fig. 1, a parallel beam of coherent light is divided into two equal intensity beams by a beam-splitter. The two beams are reflected back by the respective mirrors, and interfere after being recombined by the beam-splitter. The resulting beam, or *interferogram*, is later recorded (in intensity) by a standard imaging sensor, which captures one image per mirror position. In biological applications, the interferogram illuminates a biological sample placed between the beam splitter and the detector.

It can be shown that the recorded interferogram $I(d)$, *i.e.*, as a function of the mirror position d , is the Fourier transform of the light source $\tilde{I}(\nu)$ (which is modulated by the absorption spectrum of a cell) as a function of the wavenumber ν , *i.e.*, $I(d) = \int_{-\infty}^{+\infty} \tilde{I}(\nu) e^{-j2\pi d\nu} d\nu$ (see [3, Ch. 1] for the details).

This recorded interferogram is discretized into the rows of a matrix $\mathbf{Y}^{\text{Nyq}} = \{\mathbf{y}_i\}_{i=1}^{N_p}$, where $\mathbf{y}_i \in \mathbb{R}^{N_d}$ is the collection of interferogram intensities recorded at the pixel i , $1 \leq i \leq N_p$. N_d is the maximum number of mirror positions, *i.e.*, in the conventional FTI $N_d = N_\nu$. In other words, each row of $\mathbf{Y}^{\text{Nyq}} \in \mathbb{R}^{N_p \times N_p}$ represents the recorded spatial map for one mirror position, *i.e.*, the signal $I(d)$ mentioned before. The relation between the acquired interferogram \mathbf{Y}^{Nyq} and the target HS data $\mathbf{X} \in \mathbb{R}^{N_\nu \times N_p}$ can be modeled as $\mathbf{Y}^{\text{Nyq}} = \mathbf{F}\mathbf{X}$, where $\mathbf{F} \in \mathbb{C}^{N_\nu \times N_\nu}$ is the discrete Fourier matrix.

3 Compressive Sensing-FTI

The above mentioned FTI is used in a Nyquist regime, *i.e.*, with a sufficiently dense set of uniformly spaced mirror positions,

¹For a comprehensive classification of different HS acquisition methods we refer the reader to [2].

that allows perfect recovery of the HS data with an inverse discrete Fourier transform. However, we here show that it is possible to recover the HS data, *i.e.*, the collection of all $\tilde{I}(\nu)$ for all pixels, from the interferogram signals acquired only at a few mirror positions, *i.e.*, at a sub-Nyquist rate. In fact, this strategy meets the fast acquisition requirements of biological applications. Mathematically, this amounts to reconstruct the HS data \mathbf{X} from only M rows of \mathbf{Y}^{Nyq} , with $M \leq N_\nu$. Thus, we target a compressive sensing setup modeled as $\mathbf{Y} = \mathbf{D}\mathbf{F}\mathbf{X}$, where $\mathbf{D} \in \mathbb{R}^{M \times N_\nu}$ is a selection matrix whose rows are selected at random from the identity matrix \mathbf{I}_{N_ν} .

To enable its reconstruction, we assume that \mathbf{X} is sparse in a suitable wavelet basis for both its spectral and spatial dimensions. This is a reasonable assumption as biological FTI targets the recording of the samples dyed with fluorochromes that have smooth spectra and well-organized spatial configuration (*e.g.*, cells). Thus, the matrix \mathbf{X} has a sparse representation \mathbf{S} in the Kronecker product of two wavelet bases, *i.e.*, $\mathbf{X} = \mathbf{W}_{1D}\mathbf{S}\mathbf{W}_{2D}^T$ or equivalently $\text{vec}(\mathbf{X}) = (\mathbf{W}_{2D} \otimes \mathbf{W}_{1D})\text{vec}(\mathbf{S})$. The matrices $\mathbf{W}_{1D} \in \mathbb{R}^{N_\nu \times N_\nu}$ and $\mathbf{W}_{2D} \in \mathbb{R}^{N_p \times N_p}$ are respectively the wavelet bases, that can be non-orthogonal, corresponding to the columns and rows of the matrix \mathbf{S} ; the operator $\text{vec}(\cdot)$ stacks up the columns of the given matrix. Therefore, by promoting the sparsity model for HS data, given the partial observation $\mathbf{Y} = \mathbf{D}\mathbf{F}\mathbf{X}$, the HS recovery problem is formulated as this convex inverse problem:

$$\hat{\mathbf{X}} = \underset{\mathbf{U} \in \mathbb{R}^{N_\nu \times N_p}}{\text{argmin}} \|\text{vec}(\mathbf{W}_{1D}^T \mathbf{U} \mathbf{W}_{2D})\|_1 \quad \text{s.t.} \quad \mathbf{Y} = \mathbf{D}\mathbf{F}\mathbf{U}. \quad (1)$$

Uniform versus Variable density sampling:

A typical way to generate the selection matrix \mathbf{D} is to uniformly pick the rows of identity matrix \mathbf{I}_{N_ν} at random. In contrast, we also study the case where the probability of selecting a row respects a non-uniform distribution. In [8] it is shown that for typical images, sub-sampling the two dimensional Fourier domain by the probability distribution corresponding to the inverse distance from zero frequency can outperform the uniform sub-sampling scheme. We aim to apply the philosophy of this work but on the one-dimensional interferogram signal. In practice, we observe that the amplitude of the interferogram signal decays with respect to the distance of the mirror from the point $d = 0$, where two mirrors are equally distanced from the beam-splitter. Thus, by capturing more samples at the points close to $d = 0$, the amount of useful acquired information will be boosted. As the work in [8], we establish one-dimensional variable density sampling with probability distribution corresponding to inverse distance from point $d = 0$, *i.e.*, the chance of choosing the i^{th} row of the Fourier matrix is set $\frac{1}{|i-c|^{\alpha+1}}$, where the constant c is set according to the index of the $d = 0$, and $\alpha > 0$ controls the exponential decay of sampling chance. An example of uniform and variable density sampling is illustrated at the bottom-right of the Fig. 1, where $w(d)$ is the chance of recording the interferogram at point d .

4 Experiments

In this section we test several numerical simulations in order to assess the performance of compressive sensing-FTI (CS-FTI) in terms of the reconstruction SNR computed as $10 \log \frac{\|\mathbf{X}\|_F^2}{\|\mathbf{X} - \hat{\mathbf{X}}\|_F^2}$ (in dB). Since the problem in (1) is a convex optimization problem containing two non-differentiable convex functions, it is solved using Douglas-Rachford proximal algorithm. We considered an HS data of size $(N_\nu, N_x, N_y) = (64, 128, 128)$ for our experiments. Fig. 2 tiles nine (out of 64)

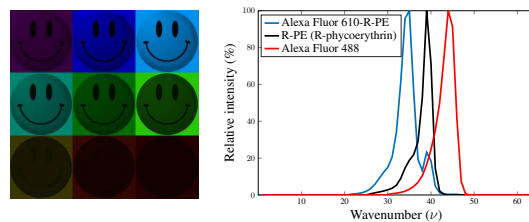


Figure 2: Illustration of nine spectral bands of the HS data (left) and the fluorochrome signatures used for generation of the HS data (right).

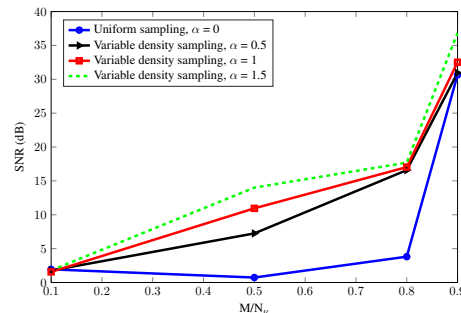


Figure 3: Reconstruction performance of uniform ($\alpha = 0$) and variable density sampling ($\alpha \in \{0.5, 1, 1.5\}$).

spectral bands of “smile face” image. This HS data is generated by multiplication of the spectrum signatures of three fluorochrome dyes with the RGB coefficients of the source image. Note that these dyes (*i.e.*, “Alexa Fluor 488”, “Alexa Fluor 610-R-PE”, and “R-PE (R-phycoerythrin)”), are used in actual biomedical experiments using the FTI device. The emission signatures of these dyes are shown in Fig. 2.

For our experiments, we tested two different sampling strategies, *i.e.*, uniform sampling and variable density sampling. To this end, the i^{th} row of \mathbf{F} is selected with a probability weighted by $\frac{1}{(i-1)^{\alpha+1}}$, for $\alpha \geq 0$. In fact we have tested $\alpha \in \{0, 0.5, 1, 1.5\}$, with $\alpha = 0$ corresponding to uniform sampling. For each type of sampling strategy we set $M/N_\nu \in \{0.1, 0.5, 0.8, 0.9\}$. Each point of the curves shown in Fig. 3 is achieved for one realization of random sampling. As depicted, in the compressive sensing regime, variable density sampling schemes have superior reconstruction performances in comparison to uniform sampling, up to 10 dB gain at $M/N_\nu = 0.5$ and $\alpha = 1.5$. This confirms that, on this setting, the performance of CS-FTI can be even improved by increasing the sampling decay rate α , *i.e.*, equivalent to a denser sampling of the mirror positions close to the point $d = 0$. Note that the reconstruction SNR for full sampling (*i.e.*, $M = N_\nu$) is achieved as 114 dB.

5 Conclusion

In this paper we presented a proof of concept for turning a conventional FTI into a fast CS-FTI. Our framework is adaptable with the actual FTI device. The goal is achieved by considering the Kronecker product of two wavelet bases as sparsity basis and also sub-sampling the Fourier coefficients that is equivalent to sub-sampling the mirror positions in the device. Two sampling strategies (uniform and variable density sampling with different decay rate) were tested. Since the amplitude of the interferogram signal decays as the mirror moves further, it is observed that variable density sampling leads to higher reconstruction quality. However, due to the physical interaction between mirror motion and 2-D detector, we may need to address the notion of physically feasible variable density sampling introduced in [12]. This hypothesis as well as the effect of disturbances, *e.g.*, instrument response convolution, and noise corruption are the scope of future research on CS-FTI.

References

- [1] C. Leonard, A. Errachid, J. Daubie, D. Beghuin, P. Courtois, M. Mingeot-Leclercq, and D. Tyteca, "Hyperspectral analysis of laurdan emission spectra in red blood cells and giant unilamellar vesicles," *Biophysical Journal*, vol. 108, no. 2, p. 622a, 2015.
- [2] R. G. Sellar and G. D. Boreman, "Comparison of relative signal-to-noise ratios of different classes of imaging spectrometer," *Applied optics*, vol. 44, no. 9, pp. 1614–1624, 2005.
- [3] R. J. Bell, *Introductory Fourier Transform Spectroscopy*. New York: Academic Press, 1972.
- [4] D. L. Donoho, "Compressed sensing," *IEEE Transactions on Information Theory*, vol. 52, no. 4, pp. 1289–1306, 2006.
- [5] E. J. Candes, J. K. Romberg, and T. Tao, "Stable signal recovery from incomplete and inaccurate measurements," *Communications on pure and applied mathematics*, vol. 59, no. 8, pp. 1207–1223, 2006.
- [6] M. Rudelson and R. Vershynin, "On sparse reconstruction from Fourier and Gaussian measurements," *Communications on pure and applied mathematics*, vol. 61, no. 8, pp. 1025–1045, 2008.
- [7] M. F. Duarte and R. G. Baraniuk, "Kronecker compressive sensing," *IEEE Transactions on Image Processing*, vol. 21, no. 2, pp. 494–504, 2012.
- [8] F. Krahmer and R. Ward, "Stable and robust sampling strategies for compressive imaging," *IEEE Transactions on Image Processing*, vol. 23, no. 2, pp. 612–622, 2013.
- [9] B. Adcock, A. C. Hansen, C. Poon, and B. Roman, "Breaking the coherence barrier: A new theory for compressed sensing," *arXiv preprint arXiv:1302.0561*, 2013.
- [10] M. Lustig, D. Donoho, and J. M. Pauly, "Sparse MRI: The application of compressed sensing for rapid MR imaging," *Magnetic resonance in medicine*, vol. 58, no. 6, pp. 1182–1195, 2007.
- [11] P. L. Combettes and J. C. Pesquet, "A Douglas–Rachford splitting approach to nonsmooth convex variational signal recovery," *IEEE Journal of Selected Topics in Signal Processing*, vol. 1, no. 4, pp. 564–574, 2007.
- [12] N. Chauffert, P. Ciuciu, J. Kahn, and P. Weiss, "Variable density sampling with continuous trajectories," *SIAM Journal on Imaging Science*, vol. 7, no. 4, pp. 1962–1992, 2014.

Inferring Sparsity: Compressed Sensing using Generalized Restricted Boltzmann Machines

Eric W. Tramel[†], Andre Manoel[†], Francesco Caltagirone[‡], Marylou Gabrié[†] and Florent Krzakala^{†§}

[†]Laboratoire de Physique Statistique (CNRS UMR-8550),

École Normale Supérieure, PSL Research University, 24 rue Lhomond, 75005 Paris, France

[§]Université Pierre et Marie Curie, Sorbonne Universités, 75005 Paris, France

[‡]INRIA Paris, 2 rue Simone Iff, 75012 Paris, France

Abstract—In this work, we consider compressed sensing reconstruction from M measurements of K -sparse structured signals which do not possess a writable correlation model. Assuming that a generative statistical model, such as a Boltzmann machine, can be trained in an unsupervised manner on example signals, we demonstrate how this signal model can be used within a Bayesian framework of signal reconstruction. By deriving a message-passing inference for general distribution restricted Boltzmann machines, we are able to integrate these inferred signal models into approximate message passing for compressed sensing reconstruction. Finally, we show for the MNIST dataset that this approach can be very effective, even for $M < K$.

Over the past decade, the study of compressed sensing (CS) [1–3] has lead to many significant developments in the field of signal processing including novel sub-Nyquist sampling strategies [4, 5] and a veritable explosion of work in sparse approximation and representation [6]. The core problem in CS is the reconstruction of a sparse signal of dimensionality N from a set of M noisy observations for $M \ll N$. Here, a *sparse* signal is defined as one which possesses many fewer non-zero coefficients, K , than its ambient dimensionality, $K \ll N$. In [7], it was shown that using sum-product belief propagation (BP) in conjunction with a two-mode Gauss-Bernoulli sparse signal prior provided a much more favorable phase transition, as compared to ℓ_1 minimization, for K -sparse signal reconstruction. This technique was further refined in [8, 9] as a fully Bayesian perspective of the approximate message passing (AMP) of [10]. The works [11, 12] sought to model support correlation directly by leveraging the abstraction power of latent variable models via Boltzmann machines trained on examples of signal support. While these techniques demonstrated significant improvements in recovery performance for sparse signals, they are still fundamentally bound by the $M = K$ transition.

In this work, we investigate the possibility of modeling both signal and support, as in [13, 14], using a trained latent variable model as prior for the AMP reconstruction. For this, we turn to real-valued restricted Boltzmann machines (RBMs). In order to utilize real-valued RBMs within the AMP framework, we propose an extended mean-field approximation similar in nature to [12, 15]. However, we extend this approximation to the case of *general distributions* on both hidden and visible units of the RBM, allowing us to model sparse signals directly. Given this trained RBM, we propose a CS reconstruction algorithm which amounts to two nested inference problems, one on the CS observation-matching problem, and the other on the RBM model. In our results, we show that this technique can provide good reconstructions even for $M < K$, as the RBM signal prior not only models the support correlation structure, but the joint distribution of the on-support values, as well.

PROPOSED APPROACH

We wish to recover some unknown K -sparse signal $\mathbf{x} \in \mathbb{R}^N$ given a set of observations $\mathbf{y} \in \mathbb{R}^M$, $M \ll N$, generated by

$\mathbf{y} = \mathbf{F}\mathbf{x} + \mathbf{w}$ where $\mathbf{w} \sim \mathcal{N}(\mathbf{0}, \Delta\mathbf{I})$ and the matrix $\mathbf{F} \in \mathbb{R}^{M \times N}$ is a projection operator, usually random, which satisfies some restricted isometry [16]. While a number of different output channels of the form $\mathbf{y} = g(\mathbf{F}\mathbf{x})$ could be conceived [8], for clarity we focus on the case of an additive white Gaussian noise (AWGN) channel.

Following the Bayesian approach to signal reconstruction, we will focus on estimation techniques involving the posterior distribution

$$P(\mathbf{x}|\mathbf{F}, \mathbf{y}) = \frac{e^{-\frac{1}{2\Delta}\|\mathbf{y}-\mathbf{F}\mathbf{x}\|_2^2} P_0(\mathbf{x})}{\int d\mathbf{x} e^{-\frac{1}{2\Delta}\|\mathbf{y}-\mathbf{F}\mathbf{x}\|_2^2} P_0(\mathbf{x})}. \quad (1)$$

Even if computing the moments of (1) is intractable for some $P_0(\mathbf{x})$, [9, 10] show that the minimum mean-square-error (MMSE) estimator, $\hat{\mathbf{x}}_{\text{MMSE}}(\mathbf{F}, \mathbf{y}) = \int d\mathbf{x} \mathbf{x} P(\mathbf{x}|\mathbf{F}, \mathbf{y})$, can be computed extremely efficiently using loopy BP or AMP whenever $P_0(\mathbf{x})$ is fully factorized.

The AMP algorithm [8–10] provides, at each step of its iteration, an approximation to the posterior of the form

$$Q(\mathbf{x}|\mathbf{A}, \mathbf{B}) = \frac{1}{\mathcal{Z}(\mathbf{A}, \mathbf{B})} P_0(\mathbf{x}) e^{-\frac{1}{2}\sum_i A_i x_i^2 + \sum_i B_i x_i}, \quad (2)$$

where $\mathcal{Z}(\mathbf{A}, \mathbf{B})$ is a normalization, and \mathbf{A} and \mathbf{B} are quantities obtained by iterating the AMP equations. Given a computable $\mathcal{Z}(\mathbf{A}, \mathbf{B}) = \int d\mathbf{x} P_0(\mathbf{x}) e^{-\frac{1}{2}\sum_i A_i x_i^2 + \sum_i B_i x_i}$, the moments of Q are easily obtainable from

$$a_i \triangleq \frac{\partial \ln \mathcal{Z}(\mathbf{A}, \mathbf{B})}{\partial B_i}, \quad c_i \triangleq \frac{\partial^2 \ln \mathcal{Z}(\mathbf{A}, \mathbf{B})}{\partial B_i^2}. \quad (3)$$

In particular, whenever the prior distribution is fully factorized, $P_0(\mathbf{x}) = \prod_i P_0(x_i)$, evaluating $\mathcal{Z}(\mathbf{A}, \mathbf{B})$ amounts to solving N independent one-dimensional integrals.

In what follows, we use an RBM [17] to model the signal's prior distribution jointly with a set of latent, or *hidden*, variables \mathbf{h} ,

$$P_0(\mathbf{x}, \mathbf{h}|\boldsymbol{\theta}) = \frac{1}{Z(\boldsymbol{\theta})} e^{\mathbf{x}^T \mathbf{w} \mathbf{h}} \prod_i P_0(x_i|\boldsymbol{\theta}_x) \prod_\mu P_0(h_\mu|\boldsymbol{\theta}_h), \quad (4)$$

and the parameters $\boldsymbol{\theta} = \{\mathbf{W}, \boldsymbol{\theta}_x, \boldsymbol{\theta}_h\}$ can be obtained by training the RBM over a set of examples [15, 18]. This construction defines a *generalized* RBM (GRBM), in the sense that the visible and hidden variables are not strictly binary and may possess any distribution. Using a GRBM as a signal prior, the normalization of (2) is no longer factorized or tractable, thus requiring some approximation to calculate the necessary moments of Q .

To approximate the moments, we construct a message-passing scheme between the factors and the hidden and visible variables of the RBM in a general setting with arbitrary distributions on both the hidden and visible variables. Message-passing inference on the edges of the factor graph can be

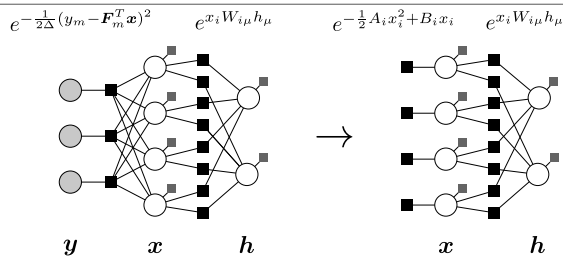


Fig. 1. *Left*: Factor graph representation of the posterior (1) given the RBM signal prior (4). Circles and squares represent variables and factors, respectively. Light gray circles are the observed signal measurements. Black factors are the factors induced by linear operators \mathbf{F} and \mathbf{W} . Light gray factors represent prior distributions influencing their adjoining variables. *Right*: Factor graph for the approximating posterior (2). Factors on the left represent local effective potentials provided by AMP at each of its iterations.

quite memory and computationally intensive, especially if this inference occurs nested as an inner loop of AMP. If we assume that the entries of \mathbf{W} are small and weakly correlated, we can construct an algorithm which operates entirely on the beliefs, the nodes of the factor graph, rather than the messages, the edges. Such an algorithm is similar in spirit to AMP and also to the Thouless-Anderson-Palmer (TAP) equations from statistical physics. We now write these TAP self-consistency equations closed on the parameters of the marginal beliefs alone,

$$A_\mu^h = - \sum_{i \in V} W_{i\mu}^2 c_i^v, \quad B_\mu^h = a_\mu^h A_\mu^h + \sum_{i \in V} W_{i\mu} a_i^v, \quad (5)$$

$$a_\mu^h = f_a^h(A_\mu^h, B_\mu^h), \quad c_\mu^h = f_c^h(A_\mu^h, B_\mu^h), \quad (6)$$

$$A_i^v = - \sum_{\mu \in H} W_{i\mu}^2 c_\mu^h, \quad B_i^v = a_i^v A_i^v + \sum_{\mu \in H} W_{i\mu} a_\mu^h, \quad (7)$$

$$a_i^v = f_a^v(A_i^v, B_i^v), \quad (8)$$

$$c_i^v = f_c^v(A_i^v, B_i^v), \quad (9)$$

where the prior-dependent functions for the visible and hidden variables, (f_a^v, f_c^v) and (f_a^h, f_c^h) , are defined in a fashion similar to (3), i.e. as the moments of an approximating distribution similar to (2), but using the desired hidden and visible distributions in place of P_0 . Using the equations detailed in (5)–(9), we can construct a fixed-point iteration (FPI) which, given some arbitrary starting condition, can be run until convergence in order to obtain the GRBM-inferred distribution on the signal variables defined by \mathbf{a} , \mathbf{c} . These distributions are then passed back to the CS observational factors to complete the AMP iteration for CS reconstruction.

We now present the results of our numerical studies of GRBM-AMP performance for the AWGN CS reconstruction task. For all reconstruction tasks, an AWGN noise variance $\Delta = 10^{-8}$ was used. Additionally, all elements of the sampling matrices \mathbf{F} were drawn from a zero-mean Gaussian distribution of variance $1/\sqrt{N}$. The results we present are based on the MNIST handwritten digit dataset [19]. We test three different approaches for this dataset. The first, termed non-i.i.d. AMP, consists of empirically estimating the per-coefficient prior hyper-parameters from the training data. This approach assumes a fully factorized model of the data, neglecting any covariance structure between the coefficients. The second approach is that of [12], here termed binary-support RBM (BRBM-AMP), which uses a binary RBM to model the correlation structure of the support, alone. Finally, we test the proposed GRBM-AMP, using a general RBM trained with binary hidden units

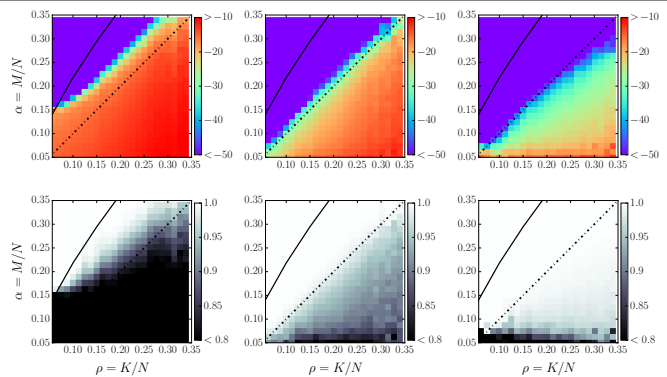


Fig. 2. **(Left)** CS reconstruction performance over first 1,000 digit images from the MNIST test partition. Results for non-i.i.d. AMP, support-based BRBM-AMP, and GRBM-AMP are on the left, center, and right, respectively. The $M = K$ oracle support transition is indicated by the black dotted line, and the spinodal transition [9] by the solid one. *Top*: Average reconstruction accuracy in MSE measured in dB. *Bottom*: Average reconstruction correlation with original digit image.

and Gauss-Bernoulli visible units, which models the data in its ambient domain.

To train the GRBM parameters, we use a GRBM with 784 binary hidden units. The RBM can be trained using either contrastive divergence, sampling the visible units from a truncated GB prior, or using the GRBM TAP iteration shown here in conjunction with the EMF strategy of [15], a strategy which we detail in a forthcoming work. For the specific GRBM model we use for these CS experiments, we train a GRBM using the EMF approach. In the case of the BRBM, a model with 784 hidden units was trained using the EMF approach.

We present the results of the three approaches in Fig. 2, where we evaluate reconstruction performance over the test set in terms of both MSE, measured in decibels, and correlation between the reconstructed and original images, where correlation is measured as $(\mathbf{x} - \bar{\mathbf{x}})^T (\mathbf{a} - \bar{\mathbf{a}}) / \sigma_{\mathbf{x}} \sigma_{\mathbf{a}}$. In both of these comparisons, we show performance over the phase diagram, where α refers to the number of CS measurements observed and ρ refers to the overall sparsity for each digit image, K/N , where K is the number of non-zero pixels in the digit image. As many of the tested images possess few non-zeros, the test dataset is skewed towards small ρ , hence the increased variability at $\rho > 0.3$ for Fig. 2. From these results, we can see a clear progression of reconstruction performance as we move from an empirical factorized model, to a model of the support alone, to a model of the signal itself.

In this work, we derived an AMP-based algorithm using an RBM to model the signal class in its ambient domain. To accomplish this modeling, we developed a model for a class of general RBMs, allowing for arbitrary distributions on the hidden and visible units. To allow the use of such a model within AMP, we proposed a TAP-based approximation of the RBM which we derived from belief propagation. By performing inference on the RBM under the influence of the outer AMP inference, we have developed a novel algorithm for CS reconstruction of sparse structured data. The proposed approach can be of great use in signal reconstruction contexts where there exists an abundance of data which lack known correlation models.

This research was funded by European Research Council under the European Unions 7th Framework Programme (FP/2007-2013/ERC Grant Agreement 307087-SPARCS).

REFERENCES

- [1] E. J. Candès and M. B. Wakin, "An introduction to compressive sampling," *IEEE Signal Processing Magazine*, vol. 25, no. 2, pp. 21–30, 2008.
- [2] E. Candès and J. Romberg, "Signal recovery from random projections," in *Computational Imaging III*. Proc. SPIE 5674, Mar. 2005, pp. 76–86.
- [3] D. L. Donoho, "Compressed sensing," *IEEE Trans. on Information Theory*, vol. 52, no. 4, pp. 1289–1306, Apr. 2006.
- [4] D. Takhar, J. N. Laska, M. B. Wakin, M. F. Duarte, D. Baron, S. Sarvotham, K. F. Kelly, and R. G. Baraniuk, "A new compressive imaging camera architecture using optical-domain compression," in *Computational Imaging IV*. Proc. SPIE 6065, 2006, p. 606509.
- [5] M. Mishali, Y. C. Eldar, O. Dounaevsky, and E. Shoshan, "Xampling: Analog to digital at sub-Nyquist rates," *IET Circuits, Devices and Systems*, vol. 5, no. 1, pp. 8–20, January 2011.
- [6] Z. Zhang, Y. Xu, J. Yang, X. Li, and D. Zhang, "A survey of sparse representation: Algorithms and applications," *IEEE Access*, vol. 3, pp. 290–530, 2015.
- [7] S. Rangan, "Estimation with random linear mixing, belief propagation and compressed sensing," in *Proc. Annual Conf. on Information Sciences and Systems*, 2010, pp. 1–6.
- [8] —, "Generalized approximate message passing for estimation with random linear mixing," in *Proc. IEEE Intl. Symp. on Info. Theory*, 2011, p. 2168.
- [9] F. Krzakala, M. Mézard, F. Sausset, Y. Sun, and L. Zdeborová, "Probabilistic reconstruction in compressed sensing: Algorithms, phase diagrams, and threshold achieving matrices," *Journal of Statistical Mechanics: Theory and Experiment*, vol. 2012, no. 8, p. P08009, 2012.
- [10] D. L. Donoho, A. Maleki, and A. Montanari, "Message-passing algorithms for compressed sensing," *Proc. National Academy of Sciences of the U.S.A.*, vol. 106, no. 45, p. 18914, 2009.
- [11] A. Drémeau, C. Herzet, and L. Daudet, "Boltzmann machine and mean-field approximation for structured sparse decompositions," *IEEE Trans. on Signal Processing*, vol. 60, no. 7, pp. 3425–3438, 2012.
- [12] E. W. Tramel, A. Drémeau, and F. Krzakala, "Approximate message passing with restricted Boltzmann machine priors," *Journal of Statistical Mechanics: Theory and Experiment*, 2016, to appear.
- [13] P. Schniter, "Turbo reconstruction of structured sparse signals," in *Proc. Conf. on Info. Sciences and Systems*, 2010, pp. 1–6.
- [14] S. Rangan, A. K. Fletcher, V. K. Goyal, and P. Schniter, "Hybrid approximate message passing with applications to structured sparsity," November 2011, arXiv Preprint, [cs.IT]:1111.2581.
- [15] M. Gabrié, E. W. Tramel, and F. Krzakala, "Training restricted Boltzmann machines via the Thouless-Anderson-Palmer free energy," in *Advances in Neural Information Processing System*, vol. 28, Montreal, Canada, June 2015, pp. 640–648.
- [16] E. J. Candès and T. Tao, "Decoding by linear programming," vol. 51, no. 12, pp. 4203–4215, Dec. 2005.
- [17] P. Smolensky, *Information Processing in Dynamical Systems: Foundations of Harmony Theory*, ser. Parallel Distributed Processing: Explorations in the Microstructure of Cognition. MIT Press, 1986, ch. 6, pp. 194–281.
- [18] G. E. Hinton, "Training products of experts by minimizing contrastive divergence," *Neural Computation*, vol. 14, no. 8, pp. 1771–1800, 2002.
- [19] Y. LeCun, L. Bottu, Y. Bengio, and P. Haffner, "Gradient-based learning applied to document recognition," *Proc. of the IEEE*, vol. 86, no. 11, pp. 2278–2324, November 1998.

Interpolation on manifolds using Bézier functions

Pierre-Yves Gousenbourger¹, P.-A. Absil¹, Benedikt Wirth² and Laurent Jacques¹.

¹ Université catholique de Louvain - ICTEAM Institute, B-1348 Louvain-la-Neuve, Belgium

² University of Münster - Institute for Numerical and Applied Mathematics, Einsteinstraße 62, D-48149 Münster, Germany

Abstract – Given a set of data points lying on a smooth manifold, we present methods to interpolate those with piecewise Bézier splines. The spline is composed of Bézier curves (resp. surfaces) patched together such that the spline is continuous and differentiable at any point of its domain. The spline is optimized such that its mean square acceleration is minimized when the manifold is the Euclidean space. We show examples on the sphere S^2 and on the special orthogonal group $SO(3)$.

1 Introduction

Given a set of data points (p_k) in a manifold \mathcal{M} associated to nodes $(k) \in \mathbb{Z}^s$ of a Cartesian grid in \mathbb{R}^s , we seek a C^1 function $\mathfrak{B} : \mathbb{R}^s \rightarrow \mathcal{M}$ such that $\mathfrak{B}(k) = p_k$. In this paper, we consider the cases where $s \in \{1, 2\}$, i.e. curves and surfaces.

This interpolation problem is motivated by several applications, as more and more acquired data tends to be constrained to smooth manifolds. In Pennec *et al.* [8], diffusion tensor images are assumed to lie on the manifold of positive definite matrices. Bergmann and Weinmann [4] propose inpainting models for images whose color pixels lie on the 2-sphere.

Manifold modeling appears in many other different fields including image modeling and processing [9] or optimization [1]. Its advantages are that (i) problem solutions are searched on spaces of much lower dimensionality compared to the ambient domain, with a direct and positive impact on algorithm performances in computational time, memory and accuracy; (ii) complex objects are represented by vectors of small size; and (iii) close formulas can be found for problems on manifolds while complex iterative procedures are required on Euclidean spaces.

Interpolation on manifold does not appear much in the literature. Popiel and Noakes [10] propose a manifold version of Bézier curves based on the work on \mathbb{R}^r of Farin [6]. Boumal *et al.* proposed optimization algorithms for curve fitting on manifolds with the toolbox Manopt [5]. More recently, Solomon *et al.* [11] developed a Wasserstein distance-based method to interpolate probability distributions evaluated on manifolds.

In this paper, we summarize different techniques to interpolate data points on manifolds by means of a C^1 piecewise-cubic Bézier spline [7, 3, 2], as illustrated in Figure 1. In Sec. 2, we define Bézier splines on manifolds and give continuity and differentiability conditions. We show in Sec. 3 how these splines can be optimized to have a small global energy. We present numerical examples in Sec. 4.

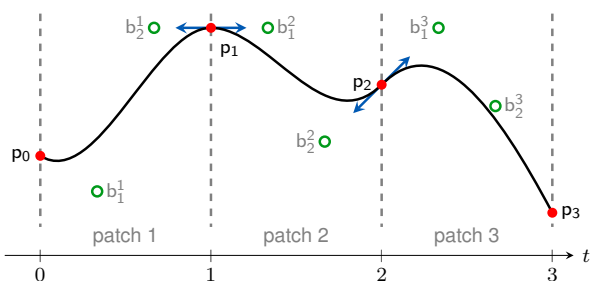


Figure 1: 1-D schematic representation of a three-pieces cubic Bézier spline with its continuity and differentiability constraints.

2 Bézier curves and surfaces

We first recall the definitions of Bézier curves and surfaces on the Euclidean space and we generalize them to manifolds. Then, we give conditions to achieve interpolation, continuity and derivability of the spline.

Curves and surfaces on the Euclidean space \mathbb{R}^r . Let $B_{k3}(t)$ be Bernstein polynomials and $\mathbf{b} = (b_0, \dots, b_3) \subset \mathbb{R}^r$ be a set of *control points*. Cubic Bézier curves are functions $\beta_3(\cdot, \mathbf{b}) : [0, 1] \rightarrow \mathbb{R}^r$ of the form

$$\beta_3(t; \mathbf{b}) \mapsto \sum_{i=0}^3 b_i B_{i3}(t). \quad (1)$$

Cubic Bézier surfaces $\beta_3(\cdot, \mathbf{b}) : [0, 1]^2 \rightarrow \mathbb{R}^r$ are their bivariate extensions with $\mathbf{b} = (b_{ij})_{i,j=0,\dots,3} \subset \mathbb{R}^r$

$$\beta_3(t_1, t_2; \mathbf{b}) = \sum_{i,j=0}^3 b_{ij} B_{i3}(t_1) B_{j3}(t_2), \quad (2)$$

Control points b_{ij} are interpolated when $i, j \in \{0, 1\}$.

Curves on a manifolds. We generalize (1) to a smooth, connected, finite-dimensional Riemannian manifold \mathcal{M} (where $\mathcal{M} = \mathbb{R}^r$ is included) in two different ways. First, since Bernstein polynomials form a partition of unity, one remarks that the Bézier curves are a weighted average of the control points

$$\beta_3(\cdot; \mathbf{b}) : [0, 1] \rightarrow \mathcal{M}, t \mapsto \text{av}[(b_i)_{i=0,\dots,3}, (B_{i3}(t))_{i=0,\dots,3}], \quad (3)$$

where $\text{av}[(y_0, \dots, y_n), (w_0, \dots, w_n)]$ is the weighted geodesic average $x = \text{argmin}_y \sum_{i=0}^n w_i d^2(y_i, y)$ with the geodesic distance d . Necesserally, when d is the Euclidean distance, definition (3) reduces to equation (1). This model is introduced in Absil *et al.* [2].

The second generalization of (1) to the manifold setting is based on the De Casteljaou algorithm (see Farin [6] for details in \mathbb{R}^r) where the Euclidean straight line is replaced by geodesics. Popiel and Noakes [10] proposed a manifold version of the algorithm and Arnould *et al.* [3] applied it to shape analysis.

Surfaces on manifolds. Similarly, we generalize (2) to \mathcal{M} in three different ways. First, Bézier surfaces can be interpreted as a one-parameter family of Bézier curves

$$\begin{aligned} \beta_3(t_1, t_2; \mathbf{b}) &= \sum_{j=0}^3 \left(\sum_{i=0}^3 b_{ij} B_{i3}(t_1) \right) B_{j3}(t_2) \\ &= \beta_3(t_2; (\beta_3(t_1; \mathbf{b}_j))_{j=0,\dots,3}), \end{aligned}$$

where $\mathbf{b}_j = (b_{ij})_{i=0,\dots,3}$. That formulation allows an evaluation based on curves as stated above.

A second interpretation of surfaces extends equation (3) as Bézier surfaces are convex combinations of their control points

$$\beta_3(t_1, t_2; \mathbf{b}) = \text{av}[(b_{ij})_{i,j=0,\dots,3}, (B_{i3} B_{j3})_{i,j=0,\dots,3}]. \quad (4)$$

Here again, the Euclidean Bézier surface is recovered with the classical Euclidean averaging.

The last generalization is also based on a geodesic extension of the De Casteljaou algorithm (Farin [6]). All these methods are developed in Absil *et al.* [2].

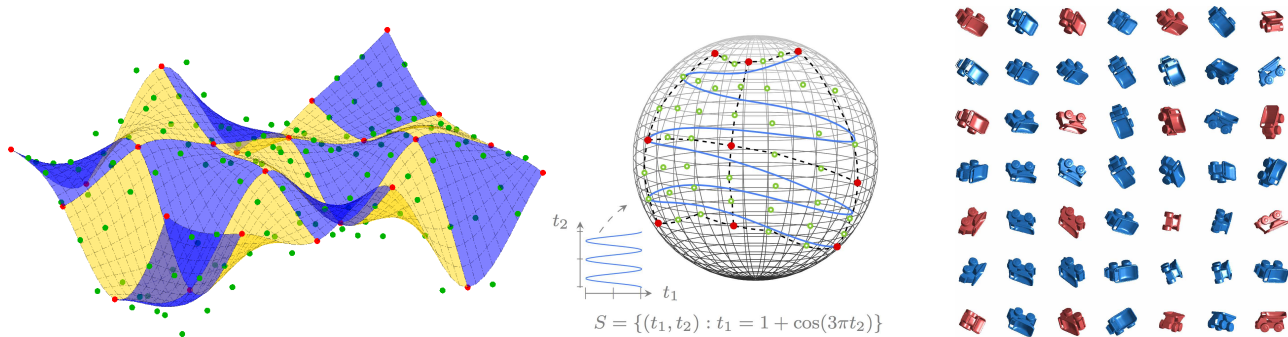


Figure 2: Differentiable piecewise-cubic Bézier surfaces. *Left*: $\mathcal{M} = \mathbb{R}^3$. The Bézier spline is composed of different Bézier surfaces (blue and yellow). It interpolates the (red) data points and is parametrized by the (green) control points. *Middle*: $\mathcal{M} = S^2$. Data points (red) are interpolated on the 2-sphere by a cubic Bézier spline. The (blue) curve is a smooth 1D-path on the surface. *Right*: $\mathcal{M} = SO(3)$. Data points (red) are orientations of a rigid body, represented as points on the special orthogonal group. The (blue) surface interpolates them.

Smooth splines on manifolds. A Bézier spline corresponds to several Bézier curves $(\beta_3^m)_{m=0,\dots,M}$ (or surfaces $(\beta_3^{mn})_{m,n \in \{0,\dots,M\} \times \{0,\dots,N\}}$) patched together (see Figure 1 for an example). For curves, the spline is continuous and interpolates the data points if $b_3^m = b_0^{m+1} = p_{m+1}$ for $m = 1, \dots, M-1$. Surfaces are continuously patched if their control points are the same at the shared border. Data points p_{mn} are interpolated if $b_{00}^{m,n} = p_{m,n}$.

Differentiability of curves is achieved by constraining p_m to be in the middle of the geodesic between b_2^m and b_1^{m+1} . For surface, an equivalent bidimensional constraint exists on the Euclidean space, but its manifold version does not hold for surfaces: Absil *et al.* [2] hence introduced a modified definition of the Bézier surfaces such that \mathcal{C}^1 splines can be computed on any Riemannian manifold. Setting $\mathbf{b} = (b_{ij})_{i,j \in \mathcal{I}}$ and $\mathcal{I} = \{-1, 1, 2, 4\}$, one redefines

$$\beta_3(t_1, t_2; \mathbf{b}) = \text{av}[\mathbf{b}, (w_i(t_1)w_j(t_2))_{i,j \in \mathcal{I}}] \quad (5)$$

with slightly modified weights

$$w_i(t) = \begin{cases} \frac{1}{2}B_{03}(t) & \text{if } i = -1, \\ B_{13}(t) + \frac{1}{2}B_{03}(t) & \text{if } i = 1, \\ B_{23}(t) + \frac{1}{2}B_{33}(t) & \text{if } i = 2, \\ \frac{1}{2}B_{33}(t) & \text{if } i = 4. \end{cases}$$

3 Optimal splines

In Section 2, we showed that Bézier splines offer the possibility to interpolate a set of data points. In this section, we show how the control points of the Bézier curves (resp. surfaces) can be optimally chosen to obtain a “good-looking” spline.

To do so, we first optimize the control points of the spline in $\mathcal{M} = \mathbb{R}^r$ such that (i) the energy of the spline is minimum (*i.e.* the sum among all patches of the mean square acceleration of Bézier functions $\int_{[0,1]^2} \|\dot{\beta}_3^m(\mathbf{t}, \mathbf{b})\|^2 dt$) and (ii) the spline is continuous, differentiable and interpolates the data points. The solution of this optimization problem reduces to a linear system. We then generalize this solution to manifolds.

In Gousenbourger *et al.* [7], the control points minimize

$$f[\mathbf{b}^m] = \hat{F}[\beta_2^0] + \sum_{m=1}^{M-2} \hat{F}[\beta_3^m] + \hat{F}[\beta_2^{M-1}].$$

The points b_2^m , p_m and b_1^{m+1} , $m = 1, \dots, M-1$, are aligned on a geodesic whose direction is arbitrarily fixed. The length of these geodesics, however, are not specified and can be optimized.

In Arnould *et al.* [3], the constraint are relaxed and rewritten in terms of the control points only. In other words, on \mathbb{R}^r , we set $b_1^m = 2p_m - b_2^{m-1}$. After optimization, b_2^{m-1} appears to be a weighted sum of the data points. Due to translation invariance, we generalize the result to manifolds using the inverse exponential map. The exponential map and its inverse are operators of differential geometry. Examples of those are available in [1].

In Absil *et al.* [2], we propose a method minimizing the energy of a bivariate manifold valued Bézier spline

$$f[\mathbf{b}^{mn}] = \sum_{m=0}^{M-1} \sum_{n=0}^{N-1} \hat{F}[\beta_3^{mn}].$$

In \mathbb{R}^r , the optimal control points can be expressed as affine combinations of the data points because the problem is invariant to translations. On manifolds, we express the problem on a product of (Euclidean) tangents spaces using a technique close to the one proposed in Arnould *et al.* [3].

4 Examples

On Figure 2, we show results on (*left*) the Euclidean space, (*middle*) the sphere and (*right*) the space of orthogonal orientations $SO(3)$ also named special orthogonal group. All results represent a Bézier surface computed by geodesic averaging of the control points. The control points are generated with the method proposed in Absil *et al.* [2]. On the special orthogonal group $SO(3)$ for instance (Figure 2, right) we are able to smoothly interpolate different orientations of the truck (red) by a Bézier surface (blue). The continuity and derivability of the curve is easy to see on the left and middle figures.

5 Conclusion

We summarized different interpolative methods on manifolds. These methods are generalizations of piecewise-Bézier splines in the Euclidean space to general manifolds. We showed that data points are interpolated continuously and differentially with a minimal knowledge of the geometry of the manifold. We also showed a way to choose the control points to obtain a good-looking (*i.e.* as flat as possible) spline.

References

- [1] P.-A. Absil, R. Mahony and R. Sepulchre. “Optimization algorithms on Matrix Manifolds”. Princeton University Press, Princeton, NJ, 2008.
- [2] P.-A. Absil, P.-Y. Gouzenbourger, P. Striewski, B. Wirth. “Differentiable piecewise-Bézier surfaces on Riemannian manifolds”, Technical report UCL-INMA-2015.10-v1, Université catholique de Louvain, 2016. Accepted with minor changes in SIIMS (SIAM).
- [3] A. Arnould, P.-Y. Gouzenbourger, C. Samir, P.-A. Absil, M. Canis. “Fitting Smooth Paths on Riemannian Manifolds: Endometrial Surface Reconstruction and Pre-operative MRI-Based Navigation”, In F.Nielsen and F.Barbaresco, editors, GSI2015, Springer International Publishing, 491–498, 2015.
- [4] R. Bergmann and A Weinmann. “A Second Order TV-type Approach for Inpainting and Denoising Higher Dimensional Combined Cyclic and Vector Space Data”, arXiv 1501.02684v1, 2015.
- [5] N. Boumal, B. Mishra, P.-A. Absil and R Sepulchre. “Manopt, a Matlab toolbox for optimization on manifolds”, Journal of Machine Learning Research, 15, 1455–1459, 2014.
- [6] G.E. Farin, “Curves and Surfaces for CAGD”, Morgan Kaufmann editor, Academic Press, fifth edition, 2002.
- [7] P.-Y. Gouzenbourger, C. Samir and P.-A. Absil. “Piecewise-Bézier C^1 interpolation on Riemannian manifolds with application to 2D shape morphing”, International Conference on Pattern Recognition (ICPR), 4086–4091, 2014.
- [8] X. Pennec, P. Fillard and N Ayache. “A Riemannian framework for tensor computing”, International Journal of Computer Vision, **66**(1):41–66, 2006.
- [9] G. Peyré. “Manifold models for signals and images”, Computer Vision and Image Understanding, **113**(2):249–260, 2009.
- [10] T. Popiel and L. Noakes, “Bézier curves and C^2 interpolation in Riemannian manifolds”, “J. Approx. Theory, **148**(2):111–127, 2007.
- [11] J. Solomon, F. De Goes, G. Peyré, *et al.* “Convolutional wasserstein distances”, ACM Transactions on Graphics, Association for Computing Machinery, **34**(4), 66:1–66:11, 2015.

Reliable recovery of hierarchically sparse signals

Ingo Roth, Martin Kliesch, Gerhard Wunder, and Jens Eisert

Freie Universität Berlin, Germany.

Abstract— We examine and propose a solution to the compressed sensing problem of recovering a block sparse signal with sparse blocks from linear measurements. Such problems naturally emerge in the context of mobile communication, in settings motivated by desiderata of a 5G framework. We introduce a new variant of the Hard Thresholding Pursuit (HTP) algorithm [1] referred to as HiHTP. For the specific class of sparsity structures, HiHTP performs significantly better in numerical experiments compared to HTP. We provide both a proof of convergence and a recovery guarantee for noisy Gaussian measurements that exhibits an improved asymptotic scaling in terms of the sampling complexity in comparison with the usual HTP algorithm.

1 Introduction

In the general recovery of signals the task is to approximately reconstruct a vector $\mathbf{x} \in \mathbb{C}^d$ from m noisy linear measurements

$$\mathbf{y} = \mathbf{A}\mathbf{x} + \mathbf{e} \in \mathbb{C}^m, \quad (1)$$

where $\mathbf{A} \in \mathbb{C}^{m \times d}$ is the measurement map and $\mathbf{e} \in \mathbb{C}^m$ denotes additive noise. Such problems arise in many applications, e.g. in image processing, acoustics, radar, machine learning, and mobile communication. Particularly interesting is the case where the number of measurements m is much smaller than the dimension of the signal space and where \mathbf{x} has some known structure. The machinery of compressed sensing provides powerful tools for an efficient, stable, and unique reconstruction of \mathbf{x} from \mathbf{y} and \mathbf{A} . For many instances, this idea works extraordinarily well and is most prominently investigated for the case where \mathbf{x} is sparse, see [2] and references therein.

1.1 Problem formulation

In this work, we investigate a structured setting in which even superior performance of reconstruction is to be expected: This is the situation in which $\mathbf{x} \in \mathbb{C}^{nN}$ is partitioned into N blocks each of size n , where at most $\sigma \leq n$ many elements in $s \leq N$ blocks are non-zero. We call vectors of such a sparsity pattern (s, σ) -sparse. This structure can be regarded as a simple instance of a larger class of hierarchical sparsity structures which have certain sparsities for nested levels of groupings. It can further be seen as a combination of block sparsity [3, 4] and level sparsity [5, 6].

This study is motivated by the desire to identify model-based sparsity structures [7] that (i) allow for efficient, stable and reliable recovery algorithms and (ii) are relevant in concrete technological applications. In fact, our algorithm is designed for compressive random access in machine-type communications [8], in which problems precisely of this form emerge.

1.2 Machine-type communications

Motivated by the desiderata of a 5G market for mobile phone communication, a “one shot” random access procedure has been proposed in which users can send messages without a priori synchronising with a network [8, 9, 10]. In this approach a common overloaded control channel is made use of to jointly detect sparse user activity and sparse channel profiles. Indeed, it turns out that the problem to be tackled gives rise to a sparsity structure of exactly the above form.

2 The algorithm: HiHTP

Established thresholding and greedy compressed sensing algorithms, e.g. CoSaMP [11] and Hard Thresholding Pursuit (HTP) [1], follow a common strategy: In each iteration, first, a proxy to the signal \mathbf{x} is computed from the previous approximation to the signal and from the measurement vector \mathbf{y} . From this proxy a guess for the support of \mathbf{x} is inferred by applying a thresholding operation. As second step of the iteration, the best ℓ_2 -norm approximation to the measurements compatible with this support is calculated.

In HTP the s -sparse thresholding operator (TO) is given by

$$L_s(\mathbf{z}) := \{\text{indices of } s \text{ largest absolute entries of } \mathbf{z} \in \mathbb{C}^n\}.$$

This operator returns the support of the best s -sparse approximation to \mathbf{z} . The basic idea of model-based compressed sensing [7] is to adapt this TO to the model in order to improve the performance of the algorithm. We denote the TO that yields the support of the best (s, σ) -sparse approximation to $\mathbf{z} \in \mathbb{C}^{nN}$ by $L_{s,\sigma}$. Importantly, in this case, $L_{s,\sigma}(\mathbf{z})$ can be easily calculated: We apply the σ -sparse TO to each block separately, select the s active blocks as the largest truncated blocks in ℓ_2 -norm, and collect the remaining $s \cdot \sigma$ indices in the set $L_{s,\sigma}(\mathbf{z})$.

Using $L_{s,\sigma}$ instead of L_s in the HTP yields Algorithm 1, which we call HiHTP as it is designed to recover a hierarchically structured sparsity. As in the original HTP proposal, a natural stopping criterion is that two subsequent supports coincide, i.e. $\Omega^{k+1} = \Omega^k$.

A similar modification employing $L_{s,\sigma}$ can also be applied to other compressed sensing algorithms including Itera-

Algorithm 1 (HiHTP)

Input: measurement matrix \mathbf{A} , measurement vector \mathbf{y} , block column sparsity (s, σ)

- 1: $x^0 = 0$
- 2: **repeat**
- 3: $\Omega^{k+1} = L_{s,\sigma}(\mathbf{x}^k + \mathbf{A}^*(\mathbf{y} - \mathbf{A}\mathbf{x}^k))$
- 4: $\mathbf{x}^{k+1} = \arg \min_{\mathbf{z} \in \mathbb{C}^{nN}} \{\|\mathbf{y} - \mathbf{A}\mathbf{z}\|, \text{supp}(\mathbf{z}) \subset \Omega^{k+1}\}$
- 5: **until** stopping criterion is met at $k = k$

Output: (s, σ) -sparse vector x^k

tive Hard Thresholding [12], Subspace Pursuit [13] or Orthogonal Matching Pursuit, e.g. [14] and references therein.

3 Analytical results

For the analysis of (s, σ) -sparse recovery schemes, we use a special version of the general restricted isometry property (RIP) for unions of linear subspaces [15].

Definition 1 (RIP). Given a matrix $\mathbf{A} \in \mathbb{C}^{m, nN}$, we denote by $\delta_{s, \sigma}$ the smallest $\delta \geq 0$ such that $(1 - \delta)\|\mathbf{x}\|^2 \leq \|\mathbf{A}\mathbf{x}\|^2 \leq (1 + \delta)\|\mathbf{x}\|^2$ for all (s, σ) -sparse vectors $\mathbf{x} \in \mathbb{C}^{nN}$.

One main technical insight of model-based compressed sensing [7] is that the generalised RIP of [15] allows for the same proof techniques as the standard RIP [16] and leads to improved recovery guarantees.

For Gaussian measurements the standard RIP analysis of HTP in our setting yields recovery guarantees for a number of samples $m \geq \tilde{m}$ with parametric scaling $\tilde{m} \in \mathcal{O}(s\sigma \log(Nn/(s\sigma)))$, see e.g. [2]. Making use of the custom tailored RIP constants $\delta_{s, \sigma}$, we arrive at an improved condition for HiHTP. Denoting by \mathbf{x}_Ω the projection of \mathbf{x} to the subspace of support Ω , the precise statement for the recovery of approximately (s, σ) -sparse vectors from noisy measurements is the following:

Theorem 1 (Recovery guarantee). *Suppose that the following RIP condition holds:*

$$\max\{\delta_{3s, \sigma}, \delta_{2s, 2\sigma}\} < \frac{1}{\sqrt{3}}. \quad (2)$$

Then, for any $\mathbf{x} \in \mathbb{C}^{nN}$, $\mathbf{e} \in \mathbb{C}^m$, and $\Omega \subset [nN]$ an (s, σ) -sparse support set, the sequence (\mathbf{x}^k) defined by HiHTP with $\mathbf{y} = \mathbf{A}\mathbf{x}_\Omega + \mathbf{e}$ satisfies, for any $k \geq 0$,

$$\|\mathbf{x}^k - \mathbf{x}_\Omega\| \leq \rho^k \|\mathbf{x}^0 - \mathbf{x}_\Omega\| + \tau \|\mathbf{e}\|, \quad (3)$$

where $\tau \leq 5.15/(1 - \rho)$ and

$$\rho = \left(\frac{2 \max\{\delta_{3s, \sigma}, \delta_{2s, 2\sigma}\}}{1 - \max\{\delta_{2s, \sigma}, \delta_{s, 2\sigma}\}^2} \right)^{1/2} < 1. \quad (4)$$

Well-known derivations of bounds on RIP constants for typical random matrices, e.g. Gaussian matrices or matrices with sub-Gaussian rows, proceed in two steps, see e.g. [2, 15]. From the properties of the random measurement matrix they provide a probabilistic bound on $|\|\mathbf{A}\mathbf{x}_\Omega\|^2 - \|\mathbf{x}_\Omega\|^2|$ for all normalised \mathbf{x} in \mathbb{C}^{nN} and a fixed support set Ω . With such a bound the RIP constant can be upper bounded by taking the union bound over all relevant support sets Ω [15].

Since the space of (s, σ) -sparse vectors is a proper subset of the set of all $s\sigma$ -sparse vectors, one can provide tighter probabilistic bounds for $\delta_{s, \sigma}$ compared to the standard RIP constants. In this way, we establish the successful recovery of (s, σ) -sparse vectors from Gaussian measurements provided that $m \geq \tilde{m}$ with

$$\tilde{m} \in \mathcal{O}(s \log(N/s) + s\sigma \log(n/\sigma)). \quad (5)$$

Compared to the usual HTP recovery guarantee (see above), the scaling of HiHTP is improved by the additive term $s(\sigma - 1) \log(N/s)$.

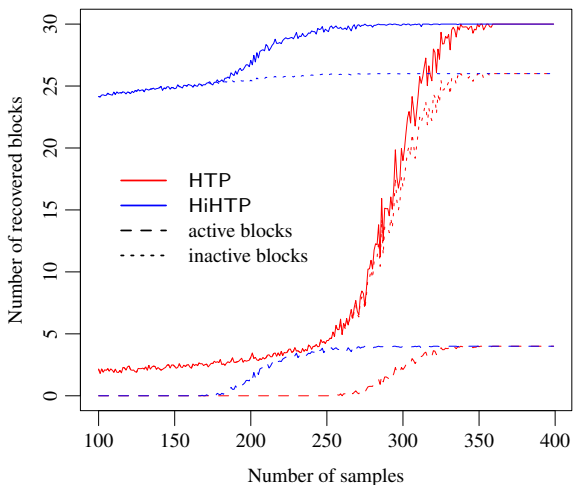


Figure 1: Number of recovered blocks over the number of measurements m for HTP and HiHTP. The dashed and dotted lines indicate the average number of correctly recovered zero and non-zero blocks, respectively. The solid lines show the total average number of recovered blocks.

4 Numerical experiments

In this section, we compare the performance of HTP and HiHTP in numerical experiments. We consider $(s = 4, \sigma = 20)$ -sparse signals consisting of $N = 30$ blocks of dimension $n = 100$. For each instance of the signal the supports are randomly drawn from a uniform distribution. The entries are i.i.d. real numbers drawn from a standard normal distribution.

We subsequently run HTP and HiHTP on Gaussian measurements of each signal. For different numbers of measurements, we count the number of successfully recovered blocks. A block is successfully recovered if it deviates by less than 10^{-8} in Euclidean norm from the corresponding block of the original signal. For each number of measurements we average over 100 runs.

Figure 1 shows the resulting recovery rates. While for HTP the number of recovered blocks quickly decays for small numbers of samples, HiHTP performs significantly better in this regime. The number of successfully recovered blocks is the relevant benchmark for a wide range of applications that do not require to always reconstruct the entire signal.

5 Conclusion and Outlook

We introduce a new model-based thresholding algorithm that is adapted to the sparsity structure of having only s non-zero blocks which itself are σ -sparse. The algorithm proves itself to be numerically more successful in the recovery of blocks from a small number of measurements. We also have a recovery guarantee supporting this claim. The results can be generalised to hierarchically structured groupings with specific group sizes and sparsities on each level. We expect the strategy of HiHTP to apply to this broader class giving rise to a variety of different applications.

Acknowledgements

We thank A. Steffens and C. Riofrío for helpful discussions. The research of IR, MK, JE has been supported by the EU (SIQS, AQuS, RAQUEL), the BMBF (Q.com), the DFG projects EI 519/9-1 (SPP1798 CoSIP) and EI 519/7-1, and the ERC (TAQ). The work of GW was carried out within DFG grants WU 598/7-1 and WU 598/8-1 (DFG Priority Program on Compressed Sensing), and the 5GNOW project, supported by the EU under grant 318555.

References

- [1] S. Foucart, “Hard Thresholding Pursuit: An Algorithm for Compressive Sensing,” *SIAM Journal on Numerical Analysis*, vol. 49, no. 6, pp. 2543–2563, 2011.
- [2] S. Foucart and H. Rauhut, *A mathematical introduction to compressive sensing*. Springer, 2013.
- [3] Y. C. Eldar and M. Mishali, “Robust recovery of signals from a structured union of subspaces,” *IEEE Transactions on Information Theory*, vol. 55, no. 11, pp. 5302–5316, Nov 2009.
- [4] —, “Block sparsity and sampling over a union of subspaces,” in *Digital Signal Processing, 2009 16th International Conference on*, July 2009, pp. 1–8.
- [5] B. Adcock, A. C. Hansen, C. Poon, and B. Roman, “Breaking the coherence barrier: A new theory for compressed sensing,” *arXiv preprint arXiv:1302.0561*, 2013.
- [6] C. Li and B. Adcock, “Compressed sensing with local structure: uniform recovery guarantees for the sparsity in levels class,” *arXiv preprint arXiv:1601.01988*, 2016.
- [7] R. G. Baraniuk, V. Cevher, M. F. Duarte, and C. Hegde, “Model-based compressive sensing,” *IEEE Transactions on Information Theory*, vol. 56, no. 4, pp. 1982–2001, April 2010.
- [8] G. Wunder, P. Jung, and M. Ramadan, “Compressive Random Access Using A Common Overloaded Control Channel,” in *IEEE Global Communications Conference (Globecom'14) – Workshop on 5G & Beyond*, San Diego, USA, December 2015.
- [9] G. Wunder, H. Boche, T. Strohmer, and P. Jung, “Sparse signal processing concepts for efficient 5g system design,” *IEEE Access*, vol. 3, pp. 195–208, 2015.
- [10] G. Wunder, P. Jung, and C. Wang, “Compressive Random Access for Post-LTE Systems,” in *IEEE International Conf. on Commun. (ICC'14) – Workshop MASSAP*, Sydney, Australia, May 2014.
- [11] D. Needell and J. A. Tropp, “CoSaMP: Iterative signal recovery from incomplete and inaccurate samples,” *Appl. Comp. Harmonic Anal.*, 2008.
- [12] T. Blumensath and M. E. Davies, “Iterative thresholding for sparse approximations,” *Journal of Fourier Analysis and Applications*, vol. 14, no. 5, pp. 629–654, 2008.
- [13] W. Dai and O. Milenkovic, “Subspace pursuit for compressive sensing signal reconstruction,” *IEEE Transactions on Information Theory*, vol. 55, no. 5, pp. 2230–2249, May 2009.
- [14] J. A. Tropp, “Greed is good: algorithmic results for sparse approximation,” *IEEE Transactions on Information Theory*, vol. 50, no. 10, pp. 2231–2242, Oct 2004.
- [15] T. Blumensath and M. E. Davies, “Sampling theorems for signals from the union of finite-dimensional linear subspaces,” *IEEE Trans. Inf. Theory*, vol. 55, no. 4, pp. 1872–1882, April 2009.
- [16] E. J. Candes and T. Tao, “Decoding by linear programming,” *IEEE Trans. Inf. Th.*, vol. 51, no. 12, pp. 4203–4215, December 2005.

Minimizing Isotropic Total Variation without Subiterations

Ulugbek S. Kamilov

Mitsubishi Electric Research Laboratories (MERL)
201 Broadway, Cambridge, MA 02139, USA
email: kamilov@merl.com.

Abstract— Total variation (TV) is one of the most popular regularizers in the context of ill-posed image reconstruction problems. Due to its particular structure, minimization of a TV-regularized function with a fast iterative shrinkage/thresholding algorithm (FISTA) requires additional sub-iterations, which may lead to a prohibitively slow reconstruction when dealing with very large scale imaging problems. In this work, we introduce a novel variant of FISTA for isotropic TV that circumvents the need for sub-iterations. Specifically, our algorithm replaces the exact TV proximal with a componentwise thresholding of the image gradient in a way that ensures the convergence of the algorithm to the true TV solution with arbitrarily high precision.

1 Introduction

Consider a linear inverse problem $\mathbf{y} = \mathbf{H}\mathbf{x} + \mathbf{e}$, where the goal is to computationally reconstruct an unknown, vectorized image $\mathbf{x} \in \mathbb{R}^N$ from the noisy measurements $\mathbf{y} \in \mathbb{R}^M$ given the known matrix $\mathbf{H} \in \mathbb{R}^{M \times N}$. The matrix \mathbf{H} models the response of the acquisition device, while the unknown vector $\mathbf{e} \in \mathbb{R}^M$ represents the measurement noise. Practical inverse problems are typically ill-posed and the standard approach to reconstruct the image often relies on the regularized least-squares estimator

$$\hat{\mathbf{x}} = \arg \min_{\mathbf{x} \in \mathbb{R}^N} \{\mathcal{C}(\mathbf{x})\} \quad (1a)$$

$$= \arg \min_{\mathbf{x} \in \mathbb{R}^N} \left\{ \frac{1}{2} \|\mathbf{y} - \mathbf{H}\mathbf{x}\|_{\ell_2}^2 + \mathcal{R}(\mathbf{x}) \right\}, \quad (1b)$$

where \mathcal{R} is a regularizer promoting solutions with desirable properties such as positivity or transform-domain sparsity.

One of the most popular regularizers for images is the *isotropic total-variation (TV)*

$$\mathcal{R}(\mathbf{x}) \triangleq \lambda \sum_{n=1}^N \|\mathbf{D}\mathbf{x}\|_{\ell_2} = \lambda \sum_{n=1}^N \sqrt{\sum_{d=1}^D ([\mathbf{D}_d\mathbf{x}]_n)^2}, \quad (2)$$

where $\lambda > 0$ is a parameter controlling the amount of the regularization, D is the number of dimensions of the signal, and $\mathbf{D} : \mathbb{R}^N \rightarrow \mathbb{R}^{N \times D}$ is the discrete gradient operator that computes finite differences along each dimension of the signal. The TV penalty has been originally introduced by Rudin *et al.* [1] as regularization approach capable of removing noise, while preserving image edges. It is often interpreted as a sparsity-promoting ℓ_1 -penalty on the magnitudes of the image gradient. TV regularization has proved to be successful in a wide range of applications in the context of sparse recovery of images from incomplete or corrupted measurements [2–6].

The minimization problem (1) with the TV regularizer (2) is a non-trivial optimization task. Two challenging aspects are the

non-smooth nature of the regularization term and the large size of typical vectors that need to be processed. The large-scale nature of the problem makes the direct, non-iterative reconstruction computationally unfeasible; it also restricts the iterative algorithms to the so-called first-order methods that perform reconstruction by successive applications of \mathbf{H} and \mathbf{H}^T . On the other hand, non-smoothness of the regularization term complicates direct application of the gradient methods. Accordingly, proximal minimization methods [7] such as *iterative shrinkage/thresholding algorithm (ISTA)* [8–10] and its accelerated variants [11, 12] are the standard first-order approaches to circumvent the non-smoothness of TV and are among the methods of choice for solving large-scale linear inverse problems.

For the general minimization problem (1), both standard and fast ISTA (often called *FISTA*) can be expressed as

$$\mathbf{x}^t \leftarrow \text{prox}_{\gamma\mathcal{R}}(\mathbf{s}^{t-1} - \gamma\mathbf{H}^T(\mathbf{H}\mathbf{s}^{t-1} - \mathbf{y})) \quad (3a)$$

$$\mathbf{s}^t \leftarrow \mathbf{x}^t + ((q_{t-1} - 1)/q_t)(\mathbf{x}^t - \mathbf{x}^{t-1}) \quad (3b)$$

with $q_0 = 1$ and $\mathbf{x}^0 = \mathbf{s}^0 = \mathbf{x}_{\text{init}} \in \mathbb{R}^N$. Here, $\gamma > 0$ a step-size that can be set to $\gamma = 1/L$ with $L \triangleq \lambda_{\max}(\mathbf{H}^T\mathbf{H})$ to ensure convergence and $\{q_t\}_{t \in [0,1,2,\dots]}$ are relaxation parameters [13]. For a fixed $q_t = 1$, the guaranteed global rate of convergence of (3) is $O(1/t)$, however, an appropriate choice of $\{q_t\}_{t \in [1,2,\dots]}$ leads to a faster $O(1/t^2)$ convergence, which is crucial for larger scale problems, where one tries to reduce the amount of matrix-vector products with \mathbf{H} and \mathbf{H}^T . Iteration (3) combines the gradient-descent step with respect to the quadratic data fidelity term with a proximal operator

$$\text{prox}_{\gamma\mathcal{R}}(\mathbf{z}) \triangleq \arg \min_{\mathbf{x} \in \mathbb{R}^N} \left\{ \frac{1}{2} \|\mathbf{x} - \mathbf{z}\|_{\ell_2}^2 + \gamma\mathcal{R}(\mathbf{x}) \right\}. \quad (4)$$

While application of ISTA is straightforward for regularizers such as ℓ_1 -penalty that admit closed form proximal operators, many other popular regularizers including TV do not have closed form proximals. This results in the need for an additional iterative algorithm for solving the corresponding minimization problem (4), which adds a significant computational overhead to the reconstruction process. For example, the original TV-FISTA by Beck and Teboulle [4] relies on an additional fast proximal-gradient algorithm for evaluating the TV proximal, which leads to sub-iterations.

In the rest of this manuscript, we describe a new variant of FISTA for solving TV regularized reconstruction problems. The algorithm builds on the traditional TV-FISTA in [4], but avoids sub-iterations by exploiting a specific approximation of the proximal as a sequence of simpler proximals. Theoretical analysis of the proposed method shows that it achieves the true TV solution with arbitrarily high precision at a global convergence rate of $O(1/t^2)$. This makes the proposed algorithm ideal for solving very large-scale reconstruction problems, where sub-iterations are undesirable.

2 Main Results

We consider the following iteration

$$\begin{aligned} \mathbf{x}^t &\leftarrow \mathbf{W}^T \mathcal{T} \left(\mathbf{W}(\mathbf{s}^{t-1} - \gamma \mathbf{H}^T (\mathbf{H} \mathbf{s}^{t-1} - \mathbf{y})); 2\gamma \lambda \sqrt{D} \right) \\ \mathbf{s}^t &\leftarrow \mathbf{x}^t + ((q_{t-1} - 1)/q_t)(\mathbf{x}^t - \mathbf{x}^{t-1}). \end{aligned} \quad (5)$$

Here, the linear transform $\mathbf{W} : \mathbb{R}^N \rightarrow \mathbb{R}^{N \times D \times 2}$ consists of two sub-operators: the averaging operator $\mathbf{A} : \mathbb{R}^N \rightarrow \mathbb{R}^{N \times D}$ and the discrete gradient \mathbf{D} as in (2), both normalized by $1/(2\sqrt{D})$. Thus, \mathbf{W} is a union of scaled and shifted discrete Haar wavelet and scaling functions along each dimension [14]. Since the transform can be interpreted as a union of $K = 2D$, scaled, orthogonal transforms, it satisfies $\mathbf{W}^T \mathbf{W} = \mathbf{I}$; however, note that $\mathbf{W} \mathbf{W}^T \neq \mathbf{I}$ due to redundancy [15]. The non-linear function

$$\mathcal{T}(\mathbf{z}; \tau) \triangleq \max(\|\mathbf{z}\|_{\ell_2} - \tau, 0) \frac{\mathbf{z}}{\|\mathbf{z}\|_{\ell_2}}, \quad (6)$$

with $\mathbf{z} \in \mathbb{R}^D$, is a component-wise shrinkage function that is applied to each scaled difference $[\mathbf{D}\mathbf{s}]_n \in \mathbb{R}^D$, with $n \in [1, \dots, N]$. The algorithm (5) is closely related to a technique called *cycle spinning* [16] that is commonly used for improving the performance of wavelet-domain denoising. In particular, when $\mathbf{H} = \mathbf{I}$, $\gamma = 1$, and $q_t = 1$, the algorithm yields the direct solution

$$\hat{\mathbf{x}} \leftarrow \mathbf{W}^T \mathcal{T}(\mathbf{W}\mathbf{y}; 2\lambda\sqrt{D}), \quad (7)$$

which can be interpreted as the isotropic version of the traditional cycle spinning algorithm restricted to the Haar wavelet-transforms. Additionally, (5) is an extension of the parallel proximal algorithm in [17] to the isotropic TV implemented with FISTA.

To establish convergence of the method (5), one remarks the following equivalence (see also the relevant discussion in [18])

$$\begin{aligned} \min_{\mathbf{x} \in \mathbb{R}^N} &\left\{ \frac{1}{2} \|\mathbf{y} - \mathbf{H}\mathbf{x}\|_{\ell_2}^2 + \lambda \sum_{n=1}^N \|[D\mathbf{x}]_n\|_{\ell_2} \right\} \\ &= \min_{\mathbf{u} \in \mathbb{R}^{KN}} \left\{ \frac{1}{2} \|\mathbf{y} - \mathbf{H}\mathbf{W}^T \mathbf{u}\|_{\ell_2}^2 + \mathcal{R}_1(\mathbf{u}) + \mathcal{R}_2(\mathbf{u}) \right\}, \end{aligned} \quad (8)$$

where the regularizers are defined as

$$\mathcal{R}_1(\mathbf{u}) \triangleq 2\lambda\sqrt{D} \sum_{n=1}^N \|[u^{\text{dif}}]_n\|_{\ell_2} \text{ and } \mathcal{R}_2(\mathbf{u}) \triangleq \mathbb{1}_{\mathcal{U}}(\mathbf{u}). \quad (9)$$

Here, \mathbf{u}^{dif} denotes difference coefficients of $\mathbf{u} = \mathbf{W}\mathbf{x}$, and $\mathbb{1}_{\mathcal{U}}$ is the indicator function for the set

$$\mathcal{U} \triangleq \{\mathbf{u} \in \mathbb{R}^{KN} : \mathbf{u} = \mathbf{W}\mathbf{W}^T \mathbf{u}\}. \quad (10)$$

Thus, the algorithm (5) can be interpreted as a simple *incremental proximal-gradient algorithm* [19] that approximates the proximal of \mathcal{R} in (2) with the successive evaluation of two proximals of \mathcal{R}_1 and \mathcal{R}_2 in (9). Then, by assuming that the gradient of the data-term and subgradients of \mathcal{R}_1 and \mathcal{R}_2 are bounded for every iterate, one can establish the following proposition.

Proposition 1. Denote with \mathbf{x}^* the solution of (1) with the TV regularizer (2). Then, for an appropriate choice of $\{q_t\}_t$, the iterates generated by the proposed method in (5) satisfies

$$(\mathcal{C}(\mathbf{x}^t) - \mathcal{C}(\mathbf{x}^*)) \leq \frac{2}{\gamma(t+1)^2} \|\mathbf{x}^0 - \mathbf{x}^*\|_{\ell_2}^2 + \gamma G^2, \quad (11)$$

where $G > 0$ is a fixed constant proportional to the bound on the gradients.

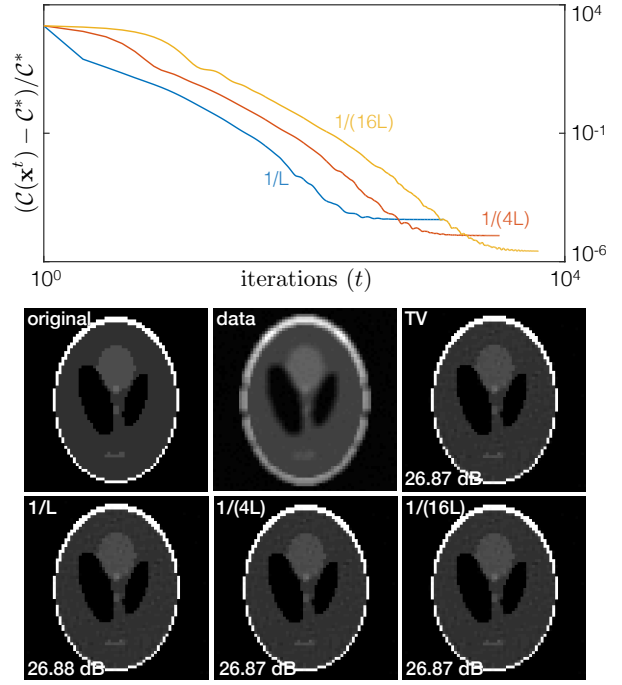


Figure 1: Recovery of the *Shepp-Logan* phantom from blurry and noisy measurements. Top: We plot the relative gap $(\mathcal{C}(\mathbf{x}^t) - \mathcal{C}(\mathbf{x}^*)) / \mathcal{C}(\mathbf{x}^*)$ against the iteration number for 3 distinct step-sizes γ . Bottom: Visual illustration of the convergence of the proposed method to the minimizer of the TV cost functional. Even for $\gamma = 1/L$ the solution of the proposed method is visually and quantitatively close to the true TV result.

Note that appropriate choice of $\{q_t\}_{t \in [1, 2, \dots]}$, simply refers to the choice of relaxation parameters used in the standard FISTA. The proof of the proposition can be established by extending the original proof of FISTA in [12] to sums of proximals as was done, for example, in [17] and [20].

Proposition 1 states that for a constant step-size, convergence can be established to a neighborhood of the optimum, which can be made arbitrarily close to 0 by letting $\gamma \rightarrow 0$. Additionally, the global convergence rate of the method equals that of the original TV-FISTA.

In Fig. 1, we illustrate the results of a simple image deblurring problem, where a 3×3 Gaussian blur of variance 2 was applied to the *Shepp-Logan* phantom. The blurry image was further contaminated with additive white Gaussian noise (AWGN) of 35 dB SNR. We plot the per-iteration gap $(\mathcal{C}(\mathbf{x}^t) - \mathcal{C}(\mathbf{x}^*)) / \mathcal{C}(\mathbf{x}^*)$, where \mathbf{x}^t is computed with the proposed algorithm and \mathbf{x}^* is the actual TV result. The regularization parameter λ was manually selected for the optimal SNR performance of TV. We compare 3 different step-sizes $\gamma = 1/L$, $\gamma = 1/(4L)$, and $\gamma = 1/(16L)$, where $L = \lambda_{\max}(\mathbf{H}^T \mathbf{H})$ is the Lipschitz constant. The figure illustrates that the theoretical results in Proposition 1 hold in practice, and that even for $\gamma = 1/L$ the solution of the proposed method is very close to the true TV result, both qualitatively and quantitatively. For this experiment, it takes about 4 times less time (in seconds) to compute the TV solution with the proposed method compared to the standard TV-FISTA.

To conclude, we proposed to use the method summarized in eq. (5) as a fast alternative to the original TV-FISTA. The time gains of the method come from the fact that it has $O(1/t^2)$ global rate of convergence and that it uses a closed form proximal instead of solving an inner minimization problem.

References

- [1] L. I. Rudin, S. Osher, and E. Fatemi, "Nonlinear total variation based noise removal algorithms," *Physica D*, vol. 60, no. 1–4, pp. 259–268, November 1992.
- [2] M. M. Bronstein, A. M. Bronstein, M. Zibulevsky, and H. Azhari, "Reconstruction in diffraction ultrasound tomography using nonuniform FFT," *IEEE Trans. Med. Imag.*, vol. 21, no. 11, pp. 1395–1401, November 2002.
- [3] M. Lustig, D. L. Donoho, and J. M. Pauly, "Sparse MRI: The application of compressed sensing for rapid MR imaging," *Magn. Reson. Med.*, vol. 58, no. 6, pp. 1182–1195, December 2007.
- [4] A. Beck and M. Teboulle, "Fast gradient-based algorithm for constrained total variation image denoising and deblurring problems," *IEEE Trans. Image Process.*, vol. 18, no. 11, pp. 2419–2434, November 2009.
- [5] D. Liu, U. S. Kamilov, and P. T. Boufounos, "Sparsity-driven distributed array imaging," in *Proc. 6th Int. Workshop on Computational Advances in Multi-Sensor Adaptive Process. (CAMSAP 2015)*, Cancun, Mexico, December 13–16, 2015, pp. 441–444.
- [6] U. S. Kamilov, I. N. Papadopoulos, M. H. Shoreh, A. Goy, C. Vonesch, M. Unser, and D. Psaltis, "Optical tomographic image reconstruction based on beam propagation and sparse regularization," *IEEE Trans. Comp. Imag.*, vol. 2, no. 1, pp. 59–70, March 2016.
- [7] H. H. Bauschke and P. L. Combettes, *Convex Analysis and Monotone Operator Theory in Hilbert Spaces*. Springer, 2010.
- [8] M. A. T. Figueiredo and R. D. Nowak, "An EM algorithm for wavelet-based image restoration," *IEEE Trans. Image Process.*, vol. 12, no. 8, pp. 906–916, August 2003.
- [9] J. Bect, L. Blanc-Feraud, G. Aubert, and A. Chambolle, "A ℓ_1 -unified variational framework for image restoration," in *Proc. ECCV*, Springer, Ed., vol. 3024, New York, 2004, pp. 1–13.
- [10] I. Daubechies, M. Defrise, and C. D. Mol, "An iterative thresholding algorithm for linear inverse problems with a sparsity constraint," *Commun. Pure Appl. Math.*, vol. 57, no. 11, pp. 1413–1457, November 2004.
- [11] J. M. Bioucas-Dias and M. A. T. Figueiredo, "A new TwIST: Two-step iterative shrinkage/thresholding algorithms for image restoration," *IEEE Trans. Image Process.*, vol. 16, no. 12, pp. 2992–3004, December 2007.
- [12] A. Beck and M. Teboulle, "A fast iterative shrinkage-thresholding algorithm for linear inverse problems," *SIAM J. Imaging Sciences*, vol. 2, no. 1, pp. 183–202, 2009.
- [13] ———, *Convex Optimization in Signal Processing and Communications*. Cambridge, 2009, ch. Gradient-Based Algorithms with Applications to Signal Recovery Problems, pp. 42–88.
- [14] S. Mallat, *A Wavelet Tool of Signal Processing: The Sparse Way*, 3rd ed. San Diego: Academic Press, 2009.
- [15] M. Elad, P. Milanfar, and R. Rubinstein, "Analysis versus synthesis in signal priors," *Inverse Problems*, vol. 23, no. 3, pp. 947–968, 2007.
- [16] R. R. Coifman and D. L. Donoho, *Springer Lecture Notes in Statistics*. Springer-Verlag, 1995, ch. Translation-invariant denoising, pp. 125–150.
- [17] U. S. Kamilov, "Parallel proximal methods for total variation minimization," in *IEEE Int. Conf. Acoustics, Speech and Signal Process. (ICASSP 2016)*, Shanghai, China, March 19–25, 2015, pp. 4697–4701.
- [18] U. S. Kamilov, E. Bostan, and M. Unser, "Wavelet shrinkage with consistent cycle spinning generalizes total variation denoising," *IEEE Signal Process. Lett.*, vol. 19, no. 4, pp. 187–190, April 2012.
- [19] D. P. Bertsekas, "Incremental proximal methods for large scale convex optimization," *Math. Program. Ser. B*, vol. 129, pp. 163–195, 2011.
- [20] H. H. Bauschke, R. Goebel, Y. Lucet, and X. Wang, "The proximal average: Basic theory," *SIAM J. Optim.*, vol. 19, no. 2, pp. 766–785, 2008.

Learning MMSE Optimal Thresholds for FISTA

Ulugbek S. Kamilov and Hassan Mansour.

Mitsubishi Electric Research Laboratories (MERL)

201 Broadway, Cambridge, MA 02139, USA

email: {kamilov, mansour}@merl.com.

Abstract— Fast iterative shrinkage/thresholding algorithm (FISTA) is one of the most commonly used methods for solving linear inverse problems. In this work, we present a scheme that enables learning of optimal thresholding functions for FISTA from a set of training data. In particular, by relating iterations of FISTA to a deep neural network (DNN), we use the error backpropagation algorithm to find thresholding functions that minimize mean squared error (MSE) of the reconstruction for a given statistical distribution of data. Accordingly, the scheme can be used to computationally obtain an MSE optimal variant of FISTA for performing statistical estimation.

1 Introduction

We consider a linear inverse problem $\mathbf{y} = \mathbf{H}\mathbf{x} + \mathbf{e}$, where the goal is to recover the unknown signal $\mathbf{x} \in \mathbb{R}^N$ from the noisy measurements $\mathbf{y} \in \mathbb{R}^M$. The matrix $\mathbf{H} \in \mathbb{R}^{M \times N}$ is known and models the response of the acquisition device, while the vector $\mathbf{e} \in \mathbb{R}^M$ represents unknown errors in the measurements.

Many practical inverse problems are ill-posed, which means that measurements \mathbf{y} cannot explain the signal \mathbf{x} uniquely. One standard approach for solving such problems is the regularized least-squares estimator

$$\hat{\mathbf{x}} = \arg \min_{\mathbf{x} \in \mathbb{R}^N} \left\{ \frac{1}{2} \|\mathbf{y} - \mathbf{H}\mathbf{x}\|_{\ell_2}^2 + \mathcal{R}(\mathbf{x}) \right\}, \quad (1)$$

where \mathcal{R} is a regularizer that imposes prior structure in order to promote more meaningful solutions.

Two common approaches for solving problem (1) is the *iterative shrinkage/thresholding algorithm (ISTA)* [1–3] and its accelerated variant called *fast ISTA (FISTA)* [4]. Both algorithms can be expressed as

$$\mathbf{s}^t \leftarrow \mathbf{x}^{t-1} + ((q_t - 1)/q_t) (\mathbf{x}^{t-1} - \mathbf{x}^{t-2}) \quad (2a)$$

$$\mathbf{x}^t \leftarrow \text{prox}_{\gamma\mathcal{R}} (\mathbf{s}^t - \gamma\mathbf{H}^T(\mathbf{H}\mathbf{s}^t - \mathbf{y})), \quad (2b)$$

with the initial condition $\mathbf{x}^0 = \mathbf{x}^{-1} = \mathbf{x}_{\text{init}} \in \mathbb{R}^N$. The parameter $\gamma > 0$ is a step-size that is often set to $\gamma = 1/L$ with $L \triangleq \lambda_{\max}(\mathbf{H}^T\mathbf{H})$ to ensure convergence, and parameters $\{q_t\}_{t \in [0, 1, \dots]}$ are called relaxation parameters [4]. For a fixed $q_t = 1$, iteration (2) corresponds to ISTA, which has $O(1/t)$ global rate of convergence; however, for an appropriate selection of $\{q_t\}_{t \in [0, 1, \dots]}$ as in [4] one obtains FISTA, which has a faster $O(1/t^2)$ convergence rate. When the regularizer \mathcal{R} is separable and acts in an identical manner in every data dimension, the proximal operator in (2b) reduces to a scalar nonlinearity

$$\mathcal{T}_\gamma(z) = \text{prox}_{\gamma\mathcal{R}}(z) \quad (3a)$$

$$\triangleq \arg \min_{x \in \mathbb{R}} \left\{ \frac{1}{2} (x - z)^2 + \gamma\mathcal{R}(x) \right\}, \quad (3b)$$

applied individually to each component z of the input vector.

Traditionally, the regularizer \mathcal{R} and the corresponding proximal operator (3) are manually designed to preserve or promote certain properties in the solution. For example, ℓ_1 -norm penalty $\mathcal{R}(\mathbf{x}) \triangleq \|\mathbf{x}\|_{\ell_1}$ is known to promote sparse solutions in (1), and has proved to be successful in a wide range of applications where signals are naturally sparse [5, 6]. One popular approach for designing regularizers comes from Bayesian theory, where \mathcal{R} is selected according to the prior statistical distribution $p_{\mathbf{x}}$ of \mathbf{x} as $\mathcal{R}(\mathbf{x}) = -\log(p_{\mathbf{x}}(\mathbf{x}))$, with the resulting estimator called the *maximum a posteriori probability (MAP)* estimator. From this statistical perspective, the ℓ_1 -norm penalty is often interpreted as a MAP estimator corresponding to the Laplace distribution. However, it has been shown that the MAP-based approach for designing proximals is suboptimal due to surprisingly poor performance of the resulting estimators in terms of mean squared error (MSE) [7, 8]. On the other hand, recent results have also shown that the minimum MSE (MMSE) statistical estimator can also be expressed as a solution of (1), where \mathcal{R} does not necessarily correspond to the negative logarithm of $p_{\mathbf{x}}$ [9–11].

In this work, we propose a data-driven scheme for computationally learning MSE optimal nonlinearities \mathcal{T} for FISTA from a set of L training examples of true signals $\{\mathbf{x}_\ell\}_{\ell \in [1, \dots, L]}$ and measurements $\{\mathbf{y}_\ell\}_{\ell \in [1, \dots, L]}$. Specifically, we interpret iterations of FISTA as layers of a simple deep neural network (DNN) [12] and develop an efficient error backpropagation algorithm that allows to recover the optimal \mathcal{T} directly from data. Thus, for a large number of independent and identically distributed (i.i.d.) realizations of $\{\mathbf{x}_\ell, \mathbf{y}_\ell\}_{\ell \in [1, \dots, L]}$, the trained algorithm can be interpreted as an MMSE variant of FISTA for a given statistical distribution of the signal and measurements.

Several other works have considered relating iterative algorithms to deep neural networks. For example, the learning scheme presented here extends the one in our recent paper [13] to FISTA, and thus improves the convergence properties of the trained algorithm. In the context of sparse coding, Gregor and LeCun [14] proposed to accelerate ISTA by learning the matrix \mathbf{H} from data. The idea was further refined by Sprechmann *et al.* [15] who considered an unsupervised learning approach and incorporated a structural sparsity model for the signal. In the context of image deconvolution, Schmidt and Roth [16] proposed a scheme to jointly learn iteration dependent dictionaries and thresholds for ADMM. Similarly, Chen *et al.* [17] proposed to parametrize nonlinear diffusion models, which are related to the gradient descent method, and learned the parameters given a set of training images. One distinction of our work is that we optimize for the same nonlinearity across iterations, which in turn allows us to interpret the algorithm as the MSE optimal FISTA for a given distribution of the data.

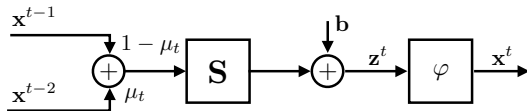


Figure 1: Visual representation of a single layer of the feedforward neural network, which also corresponds to a single iteration of FISTA. We use such layered representation of FISTA to obtain an error backpropagation algorithm for optimizing the scalar nonlinearity φ by comparing the outputs \mathbf{x}^T after T iterations against the true signal \mathbf{x} from a set of training examples.

2 Main Results

By defining a matrix $\mathbf{S} \triangleq \mathbf{I} - \gamma \mathbf{H}^T \mathbf{H}$, a vector $\mathbf{b} \triangleq \gamma \mathbf{H}^T$, parameters $\mu_t \triangleq (1 - q_{t-1})/q_t$, as well as the nonlinearity $\varphi(\cdot) \triangleq \mathcal{T}_\gamma(\cdot)$, we can re-write FISTA in (2) as follows

$$\mathbf{z}^t \leftarrow \mathbf{S} \left((1 - \mu_t) \mathbf{x}^{t-1} + \mu_t \mathbf{x}^{t-2} \right) + \mathbf{b} \quad (4a)$$

$$\mathbf{x}^t \leftarrow \varphi(\mathbf{z}^t). \quad (4b)$$

Fig. 1 visually represents a single iteration of (4), and by stacking several of such iterations one can represent (4) as a feedforward neural network (see also [13]) whose adaptable parameters correspond to the nonlinearity φ . Our objective is then to adapt the function φ by designing an efficient algorithm, given a set of L training examples $\{\mathbf{x}_\ell, \mathbf{y}_\ell\}_{\ell \in [1, \dots, L]}$, as well as a fixed number of FISTA iterations T . In order to devise a computational approach for tuning φ , we adopt the following parametric representation for nonlinearities

$$\varphi(z) \triangleq \sum_{k=-K}^K c_k \phi\left(\frac{z}{\Delta} - k\right), \quad (5)$$

where $\mathbf{c} \triangleq \{c_k\}_{k \in [-K, \dots, K]}$ are the coefficients of the representation, ϕ are basis functions positioned on the grid $\Delta[-K, -K+1, \dots, K] \subseteq \Delta\mathbb{Z}$. We can formulate the learning process in terms of the coefficients \mathbf{c} as follows

$$\hat{\mathbf{c}} = \arg \min_{\mathbf{c} \in \mathcal{C}} \left\{ \frac{1}{L} \sum_{\ell=1}^L \mathcal{E}_\ell(\mathbf{c}) \right\}, \quad (6)$$

where $\mathcal{C} \subseteq \mathbb{R}^{2K+1}$ is a set that incorporates prior constraints on the coefficients such as symmetry, monotonicity, and non-negativity on \mathbb{R}_+ [18, 19], and \mathcal{E} is a cost functional that guides the learning. The cost functional that interests us in this work is the MSE defined as

$$\mathcal{E}_\ell(\mathbf{c}) \triangleq \frac{1}{2} \|\mathbf{x}_\ell - \mathbf{x}^T(\mathbf{c}, \mathbf{y}_\ell)\|_{\ell_2}^2, \quad (7)$$

where \mathbf{x}^T is the solution of FISTA at iteration T , which depends on both coefficients \mathbf{c} and the given data vector \mathbf{y}_ℓ . Given a large number of i.i.d. realizations of the signals $\{\mathbf{x}_\ell, \mathbf{y}_\ell\}$, the empirical MSE is expected to approach the true MSE of FISTA for nonlinearities of type (5).

We optimize the coefficients \mathbf{c} in an online fashion using projected gradient iterations

$$\mathbf{c}^i \leftarrow \text{proj}_{\mathcal{C}}(\mathbf{c}^{i-1} - \alpha \nabla \mathcal{E}_\ell(\mathbf{c}^{i-1})), \quad (8)$$

where $i = 1, 2, 3, \dots$, denotes the iteration number of the training process, $\alpha > 0$ is the learning rate, and $\text{proj}_{\mathcal{C}}$ is an orthogonal projection operator on the set \mathcal{C} . Note that at each iteration i , we select a training pair $(\mathbf{x}_\ell, \mathbf{y}_\ell)$ uniformly at random.

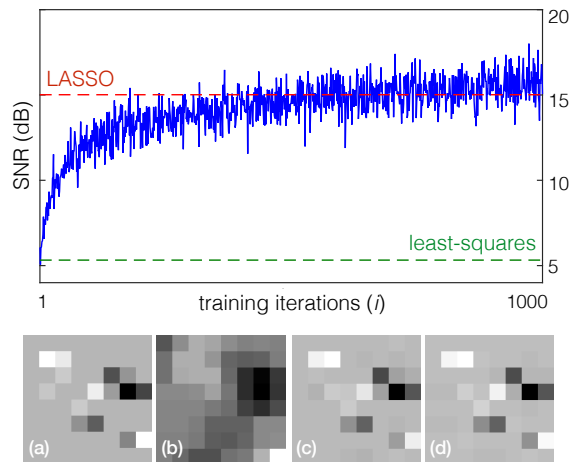


Figure 2: Illustration of the learning process for the sparse image deconvolution problem. Top: SNR of training is plotted for each training iteration. Bottom: Top 8×8 pixels of (a) original image; (b) blurry and noisy (SNR = 0.86 dB); (c) LASSO (SNR = 13.36 dB); (d) Proposed (SNR = 14.48 dB).

Let Φ^t be the matrix whose entries $\Phi_{mk}^t = \phi(z_m^t/\Delta - k)$ at row m and column k . The gradient $\nabla \mathcal{E}_\ell(\mathbf{c})$ is given by

$$\nabla \mathcal{E}_\ell(\mathbf{c}) = \mathbf{g}^1 + [\Phi^1]^T \mathbf{r}_1^1, \quad (9)$$

where \mathbf{g}^1 and \mathbf{r}_1^1 are computed using the following error backpropagation algorithm for $t = T, T-1, \dots, 2$,

$$\mathbf{g}^{t-1} \leftarrow \mathbf{g}^t + [\Phi^t]^T \mathbf{r}_1^t \quad (10a)$$

$$\mathbf{r}^{t-1} \leftarrow [\mathbf{S}^T \text{diag}(\varphi'(z^t))] \mathbf{r}_1^t \quad (10b)$$

$$\mathbf{r}_1^{t-1} \leftarrow \mathbf{r}_2^t + (1 - \mu_t) \mathbf{r}^{t-1} \quad (10c)$$

$$\mathbf{r}_2^{t-1} \leftarrow \mu_t \mathbf{r}^{t-1}, \quad (10d)$$

with $\mathbf{g}^T = 0$, $\mathbf{r}_1^T = \mathbf{r}^T = \mathbf{x}^T(\mathbf{c}, \mathbf{y}_\ell) - \mathbf{x}_\ell$, and $\mathbf{r}_2^T = 0$. Note that (10) is backward compatible with the scheme in [13]; in particular, when $\mu_t = 0$ for all t , we recover the error backpropagation algorithm for the standard ISTA.

In Fig. 2, we illustrate results of a simple image deblurring problem, where a 3×3 Gaussian blur of variance 2 was applied to a 32×32 Bernoulli-Gaussian (BG) image with sparsity ratio 0.2. The mean and variance of the Gaussian component of BG were set to 0 and 1, respectively. The blurry image was further contaminated with additive white Gaussian noise (AWGN) corresponding to 20 dB SNR. We plot per-training-iteration SNR of the reconstruction where training samples were generated in i.i.d. fashion. In all cases, FISTA was initialized with zero and run for 100 iterations. The nonlinearity φ was represented with 201 B-Spline basis functions ϕ on the interval $[-6, 6]$, and initialized with an identity operator, which means that initially the algorithm acted like a simple least-squares estimator. The plot illustrates that the learning procedure in (10) deviates the shape of φ from identity, which leads to a significant increase in the SNR of the solution until it eventually surpasses that of the ℓ_1 -based FISTA estimator denoted with LASSO. In the bottom of Fig. 2, we give an example reconstructed image by showing its top 8×8 corner.

To conclude, we proposed a scheme, summarized in eq. (10), to computationally learn shrinkage functions for FISTA. By using this scheme, it is possible to benchmark the best possible reconstruction achievable by FISTA in terms of MSE and for i.i.d. signals. Since the shrinkage functions are kept constant across the layers of our network, the number of parameters the algorithm needs to learn is small, which means that the scheme can be implemented on a simple desktop machine without extensive computations.

References

- [1] M. A. T. Figueiredo and R. D. Nowak, "An EM algorithm for wavelet-based image restoration," *IEEE Trans. Image Process.*, vol. 12, no. 8, pp. 906–916, August 2003.
- [2] J. Bect, L. Blanc-Feraud, G. Aubert, and A. Chambolle, "A ℓ_1 -unified variational framework for image restoration," in *Proc. ECCV*, Springer, Ed., vol. 3024, New York, 2004, pp. 1–13.
- [3] I. Daubechies, M. Defrise, and C. D. Mol, "An iterative thresholding algorithm for linear inverse problems with a sparsity constraint," *Commun. Pure Appl. Math.*, vol. 57, no. 11, pp. 1413–1457, November 2004.
- [4] A. Beck and M. Teboulle, "A fast iterative shrinkage-thresholding algorithm for linear inverse problems," *SIAM J. Imaging Sciences*, vol. 2, no. 1, pp. 183–202, 2009.
- [5] E. J. Candès, J. Romberg, and T. Tao, "Robust uncertainty principles: Exact signal reconstruction from highly incomplete frequency information," *IEEE Trans. Inf. Theory*, vol. 52, no. 2, pp. 489–509, February 2006.
- [6] D. L. Donoho, "Compressed sensing," *IEEE Trans. Inf. Theory*, vol. 52, no. 4, pp. 1289–1306, April 2006.
- [7] R. Gribonval, V. Cevher, and M. E. Davies, "Compressible distributions for high-dimensional statistics," *IEEE Trans. Inf. Theory*, vol. 58, no. 8, pp. 5016–5034, August 2012.
- [8] U. S. Kamilov, P. Pad, A. Amini, and M. Unser, "MMSE estimation of sparse Lévy processes," *IEEE Trans. Signal Process.*, vol. 61, no. 1, pp. 137–147, January 2013.
- [9] R. Gribonval, "Should penalized least squares regression be interpreted as maximum a posteriori estimation?" *IEEE Trans. Signal Process.*, vol. 59, no. 5, pp. 2405–2410, May 2011.
- [10] A. Kazerouni, U. S. Kamilov, E. Bostan, and M. Unser, "Bayesian denoising: From MAP to MMSE using consistent cycle spinning," *IEEE Signal Process. Lett.*, vol. 20, no. 3, pp. 249–252, March 2013.
- [11] R. Gribonval and P. Machart, "Reconciling "priors" & "priors" without prejudice?" in *Proc. Advances in Neural Information Processing Systems 26*, Lake Tahoe, NV, USA, December 5-10, 2013, pp. 2193–2201.
- [12] C. M. Bishop, *Neural Networks for Pattern Recognition*. Oxford, 1995.
- [13] U. S. Kamilov and H. Mansour, "Learning optimal nonlinearities for iterative thresholding algorithms," *IEEE Signal Process. Lett.*, vol. 23, no. 5, pp. 747–751, May 2016.
- [14] K. Gregor and Y. LeCun, "Learning fast approximation of sparse coding," in *Proc. 27th Int. Conf. Machine Learning (ICML)*, Haifa, Israel, June 21-24, 2010, pp. 399–406.
- [15] P. Sprechmann, P. Bronstein, and G. Sapiro, "Learning efficient structured sparse models," in *Proc. 29th Int. Conf. Machine Learning (ICML)*, Edinburgh, Scotland, June 26-July 1, 2012, pp. 615–622.
- [16] U. Schmidt and S. Roth, "Shrinkage fields for effective image restoration," in *Proc. IEEE Conf. Computer Vision and Pattern Recognition (CVPR)*, Columbus, OH, USA, June 23-28, 2014, pp. 2774–2781.
- [17] Y. Chen, W. Yu, and T. Pock, "On learning optimized reaction diffusion processes for effective image restoration," in *Proc. IEEE Conf. Computer Vision and Pattern Recognition (CVPR)*, Boston, MA, USA, June 8-10, 2015, pp. 5261–5269.
- [18] A. Antoniadis, "Wavelet methods in statistics: Some recent developments and their applications," *Statistical Surveys*, vol. 1, pp. 16–55, 2007.
- [19] M. Kowalski, "Thresholding rules and iterative shrinkage/thresholding algorithm: A convergence study," in *Proc. IEEE Int. Conf. Image Process (ICIP 2014)*, Paris, France, October 27-30, 2014, pp. 4151–4155.

The best of both worlds: synthesis-based acceleration for physics-driven cosparsity regularization

Srđan Kitić¹, Nancy Bertin² and Rémi Gribonval³.

¹Technicolor R&D, ²CNRS - UMR 6074, ³Inria, France. *

Abstract— Recently, a regularization framework for ill-posed inverse problems governed by linear partial differential equations has been proposed. Despite nominal equivalence between sparse synthesis and sparse analysis regularization in this context, it was argued that the latter is preferable from computational point of view (especially for huge scale optimization problems arising in physics-driven settings). However, the synthesis-based optimization benefits from simple, but effective all-zero initialization, which is not straightforwardly applicable in the analysis case. In this work we propose a multiscale strategy that aims at exploiting computational advantages of both regularization approaches.

1 Introduction

Linear partial differential equations (pde) are ubiquitous in mathematical models of physical laws. Hence, whether in implicit or explicit form, they appear in various signal processing inverse problems (ranging from, *e.g.* sound source localization to brain imaging). Inspired by impressive results in sparse signal recovery and compressed sensing [1], several works *e.g.* [2, 3, 4, 5, 6] have proposed an explicit use of such physical models in regularization of some highly ill-posed inverse problems (baptized “*physics-driven*” regularization methods).

Generally, a linear pde models the relation among two physical quantities (x, z) as $Ax = z$, where the linear operator A encapsulates the pde with appropriate initial and/or boundary conditions. Analogously, one can write $x = Dz$, where D is a linear operator acting as an “inverse” to A . Particularly, D is the integral operator encoding the so-called Green’s functions, *i.e.* impulse responses of the operator A . One is interested in inferring the quantity z , which is often characterized by a small number of free parameters (representing, for instance, dominant sources of brain activity in an EEG application). On the other hand, we are only given a few measurements y of the quantity x (*e.g.* voltage measurements at the surface of the head). The measurements are, therefore, acquired by applying a subsampling operator M to the signal x . This problem is severely ill-posed, and one way of addressing it is by asking for an estimate \hat{z} (analogously, $A\hat{x}$) having the lowest complexity, *i.e.* the fewest degrees of freedom possible.

Analytical solutions of pdes are available only in certain restricted regimes. In other cases, one approaches the problem numerically and *discretizes* the involved quantities and operators ($A \rightarrow \mathbf{A} \in \mathbb{R}^{n \times n}$, $x \rightarrow \mathbf{x} \in \mathbb{R}^n$, $D \rightarrow \mathbf{D} \in \mathbb{R}^{n \times n}$, $z \rightarrow \mathbf{z} \in \mathbb{R}^n$, $M \rightarrow \mathbf{M} \in \mathbb{R}^{m \times n}$, $y \rightarrow \mathbf{y} \in \mathbb{R}^m$). It should be clear that $\mathbf{D} = \mathbf{A}^{-1}$, which is identical to computing the response of a linear system defined by \mathbf{A} for an impulse placed at every point of a discrete n -dimensional domain.

Low complexity can be promoted through *sparsity* [1] of \mathbf{z} (minimizing $\|\mathbf{z}\|_0$) or *cosparsity* [7] of \mathbf{x} (minimizing $\|\mathbf{Ax}\|_0$). A common relaxation to these problems is the constrained ℓ_1 norm minimization (*a.k.a.* *basis pursuit*), either in the *sparse analysis*

$$\underset{\mathbf{x}}{\text{minimize}} \|\mathbf{Ax}\|_1 \text{ subject to } \mathbf{Mx} = \mathbf{y}, \quad (1)$$

or *sparse synthesis* flavor

$$\underset{\mathbf{z}}{\text{minimize}} \|\mathbf{z}\|_1 \text{ subject to } \mathbf{MDz} = \mathbf{y}. \quad (2)$$

The pde-encoding matrix \mathbf{A} thus represents the *analysis operator*, while the row-reduced Green’s function-encoding matrix \mathbf{MD} represents the (synthesis) *dictionary*.

2 The Chambolle-Pock algorithm

A popular method for solving large scale nonsmooth problems such as (1) and (2) is the so-called *Chambolle-Pock* or *preconditioned ADMM* algorithm [8]. It is a primal-dual approach based on the *saddle point* interpretation of the original constrained problem. Iteratively solving intermediate primal and dual problems avoids matrix inversion, hence its per-iteration cost is dominated by the cost of evaluating matrix-vector products and proximal operators. To make the latter efficient, one needs to appropriately customize the saddle-point problem to leverage all available structures.

Particularly, in the analysis case, we exploit the fact that \mathbf{M} is a row-reduced identity matrix. This allows for cheap projection to a set $\Theta = \{\mathbf{x} \mid \mathbf{Mx} = \mathbf{y}\}$, leading to the following saddle point formulation:

$$\underset{\mathbf{x}}{\text{minimize}} \underset{\boldsymbol{\lambda}}{\text{maximize}} \langle \mathbf{Ax}, \boldsymbol{\lambda} \rangle + \chi_{\Theta}(\mathbf{x}) - \ell_1^*(\boldsymbol{\lambda}), \quad (3)$$

where χ_{Θ} is the indicator function of the set Θ and ℓ_1^* is the convex conjugate [9, 11] of the ℓ_1 norm function (*i.e.* an indicator function of the ℓ_{∞} ball). In the synthesis case, we exploit the separability of the $\|\mathbf{z}\|_1$ objective, which yields the standard Lagrangian problem:

$$\underset{\mathbf{z}}{\text{minimize}} \underset{\boldsymbol{\lambda}}{\text{maximize}} \langle \mathbf{MDz} - \mathbf{y}, \boldsymbol{\lambda} \rangle + \ell_1(\mathbf{z}). \quad (4)$$

In both cases, $\boldsymbol{\lambda}$ represents the corresponding dual variable.

The Chambolle-Pock algorithm essentially evaluates two proximal operators per iteration, each assigned to primal and dual variable, respectively. For the presented problems, the algorithm is actually (asymptotically) first-order optimal, since it obtains $\mathcal{O}(1/k)$ convergence rate¹ [8, 10] when all penalties are non-smooth, but structured [11]. More precisely, decrease of the primal-dual gap is proportional to $\|\mathbf{A}\|_2^2/k$, in the analysis, and to $\|\mathbf{MD}\|_2^2/k$, in the synthesis case ($\|\cdot\|_2$ denotes the induced 2-norm of a matrix).

*This work was supported in part by the European Research Council, PLEASE project (ERC-StG-2011-277906).

¹Where k denotes the iteration count.

3 Computational differences

Assuming that the regularization indeed yields well-posed problems, solving (1) or (2) is equivalent, in the sense that using the solution of one problem, we can easily recover the solution of another (since $\mathbf{Ax} = \mathbf{z}$). However, as demonstrated in [12], the two optimization problems significantly differ from computational point of view. In fact, if the applied discretization is locally supported (which is often the case with, e.g., finite difference or finite element discretization methods), the analysis operator \mathbf{A} is extremely sparse (with $\mathcal{O}(n)$ nonzero entries), while the dictionary \mathbf{MD} is most often a dense matrix ($\mathcal{O}(mn)$). But the differences do not end there: as widely recognized [13], physical problems are often unstable, since small changes in \mathbf{z} can induce large fluctuations of \mathbf{x} . In line with that, discretization usually leads to increasingly ill-conditioned systems: the condition number $\kappa = \sigma_{\max}/\sigma_{\min}$ of \mathbf{A} (eq. \mathbf{D}) grows fast with n . However, one can often factorize the analysis operator (with abuse of notation) as $\tau\mathbf{A}$, where the scale factor τ depends only on the discretization stepsize and the entries of \mathbf{A} remain constant (this will be validated on the actual example in the following section). Notice that, in the basis pursuit problem (1), the scale τ does not affect the solution, and can be neglected. Now, the growth of κ is due to decrease of the smallest singular value of \mathbf{A} (i.e. increase of the largest singular value of $\mathbf{D} = \mathbf{A}^{-1}$), hence $\sigma_{\max}(\mathbf{A}) = \|\mathbf{A}\|_2$ is stable.

The consequence for the primal-dual algorithm discussed previously, is that (at worst) the synthesis approach will require orders of magnitude more iterations to converge, in addition to high computational cost per iteration. Given these arguments, one may conclude that it should be completely avoided in the physics-driven context. However, it has an important advantage over the analysis-based optimization: since the expected solution is sparse, a simple all-zero initial estimate is already close to the optimal point. In order to exploit this feature, we propose a simple scheme: i) apply *crude* (low-resolution) discretization, and solve the problem (4) to obtain the crude estimate $\tilde{\mathbf{x}} = \mathbf{D}\tilde{\mathbf{z}}$; ii) interpolate $\tilde{\mathbf{x}}$ to a target high-resolution discretization and use it as an initial point $\hat{\mathbf{x}}^{(0)}$ for the problem (3).

4 An example: 1D Laplacian

We will demonstrate the idea on a simple one-dimensional problem. Assume that on a domain $r \in [0, \phi]$, a physical process is modeled as

$$\frac{d^2x(r)}{dr^2} = z(r), \quad (5)$$

with $x(0) = x(\phi) = 0$ (e.g. modeling a potential distribution of a grounded thin rod, with sparse “charges” $z(r)$).

By applying the second order finite difference discretization to this problem, we end up with a well-known symmetric tridiagonal Toeplitz matrix \mathbf{A} (i.e. 1D discrete Laplacian), with a “stencil” defined as $\tau[-1, 2, -1]$ (henceforth, we neglect τ). This simple matrix allows for fast computation of $\mathbf{A}^{-1}\mathbf{z}$ using the Thomas algorithm [14]. In addition, it admits simple analytical expressions for extremal singular values [15], namely $\sigma_{\max} = 2 - 2\cos(\frac{n\pi}{n+1})$, and $\sigma_{\min} = 2 - 2\cos(\frac{\pi}{n+1})$. The ill-conditioning with regards to the size n is obvious, but the true value of $\|\mathbf{MD}\|_2$ is somewhat lower than $1/\sigma_{\min}$, since it also depends on the number of measurements m and the realization of the presumed random sampling. In general, one expects $\|\mathbf{MD}\|_2 \rightarrow 1/\sigma_{\min}$ as $m \rightarrow n$.

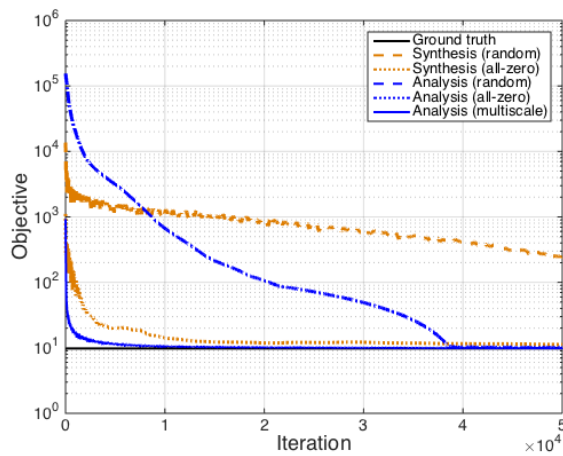


Figure 1: “Objective” := $\|\mathbf{s}\|_1 + \|\mathbf{r}\|_2^2$, where \mathbf{s} is a sparse estimate (e.g. \mathbf{Ax}) and \mathbf{r} is a residual vector (e.g. $\mathbf{Mx} - \mathbf{y}$).

To verify our claims, we simulated the problem of size $n = 10^3$, with the size of the support set being $\|\mathbf{z}\|_0 = 10$ (chosen uniformly at random from the set $[1, n]$, with coefficients iid distributed as $\mathcal{N}(0, 1)$). The measurement vector \mathbf{y} contains (selected uniformly at random) $m = 250$ samples of the signal $\mathbf{x} = \mathbf{A}^{-1}\mathbf{z}$. The iteration threshold is set to $k_{\max} = 5 \times 10^4$.

We first solve both problems (1) and (2) (using the appropriate versions of the Chambolle-Pock algorithm), by generating the initial points $\hat{\mathbf{x}}^{(0)}$ and $\hat{\mathbf{z}}^{(0)}$ randomly (iid sampled from $\mathcal{N}(0, 1)$), and then re-running both versions with all-zero initialization. Objective function decrease graphs in Figure 1 confirm our findings: when both algorithms are randomly initialized, the analysis one exhibits considerably faster convergence (moreover, the synthesis version does not reach the ground truth value). However, when the synthesis algorithm is initialized with an all-zero vector, it converges rapidly, outperforming the analysis approach in both cases (for which, interestingly, the two initializations yield the same convergence curve).

Unfortunately, in practice we are rarely capable of efficiently applying the synthesis approach, since cheap computation of $\mathbf{A}^{-1}\mathbf{z}$ is possible only in specific cases. Otherwise, \mathbf{MD} needs to be explicitly computed and stored, leading to memory bottlenecks and high per-iteration cost. To alleviate this issue, we exploit the aforementioned multiscale strategy. First, the synthesis version is appropriately initialized (with an all-zero vector) and solved on a crude, $n_{\text{low}} = 500$ grid. Then its spline-interpolated (cf. [15]) estimate is used to initialize the full resolution analysis-based solver. The “analysis (multiscale)” graph presented in Figure 1 verifies that this scheme is indeed very efficient, in this case converging the fastest among all considered algorithms and initializations.

5 Conclusion

We have presented a simple, yet effective acceleration of the analysis-based optimization, in the physics-driven setting. Leveraging the synthesis-based initialization enables orders of magnitude faster convergence compared to the naive case. Even though only a simple 1D Laplacian case was discussed and justified, we feel that the same methodology holds in more involved scenarios, comprising different multidimensional pdes with complicated boundary conditions.

References

- [1] S. Foucart and H. Rauhut, “A mathematical introduction to compressive sensing”, Springer, **1**(3), 2013.
- [2] D. Malioutov, M. Çetin and A. S. Willsky, “A sparse signal reconstruction perspective for source localization with sensor arrays”, *IEEE Transactions on Signal Processing*, **53**(8):3010–3022, 2005.
- [3] L. Stenbacka, S. Vanni, K. Uutela and R. Hari, “Comparison of minimum current estimate and dipole modeling in the analysis of simulated activity in the human visual cortices”, *NeuroImage*, **16**(4): 936–943, 2002.
- [4] I. Dokmanić and M. Vetterli, “Room helps: Acoustic localization with finite elements”, *IEEE International Conference on Acoustics, Speech and Signal Processing (ICASSP)*: 2617–2620, 2012.
- [5] S. Nam and R. Gribonval, “Physics-driven structured cospase modeling for source localization”, *IEEE International Conference on Acoustics, Speech and Signal Processing (ICASSP)*: 5397–5400, 2012.
- [6] J. Murray-Bruce and P. L. Dragotti, “Spatio-temporal sampling and reconstruction of diffusion fields induced by point sources”, *IEEE International Conference on Acoustics, Speech and Signal Processing (ICASSP)*: 31–35, 2014.
- [7] S. Nam, M. E. Davies, M. Elad and R. Gribonval, “The cospase analysis model and algorithms”, *Applied and Computational Harmonic Analysis*, **34**(1):30–56, 2013.
- [8] A. Chambolle and T. Pock, “A first-order primal-dual algorithm for convex problems with applications to imaging”, *Journal of Mathematical Imaging and Vision*, **40**(1): 120–145, 2011.
- [9] S. Boyd and L. Vandenberghe, “Convex optimization”, Cambridge university press, 2004.
- [10] A. Chambolle and T. Pock, “On the ergodic convergence rates of a first-order primal–dual algorithm”, *Mathematical Programming (Springer)*: 1–35, 2015.
- [11] Y. Nesterov, “Introductory lectures on convex optimization: A basic course”, Springer Science & Business Media, **87**, 2013.
- [12] S. Kitić, L. Albera, N. Bertin and R. Gribonval, “Physics-driven inverse problems made tractable with cospase regularization”, *IEEE Transactions on Signal Processing*, **64**(2): 335–348, 2016.
- [13] V. Isakov, “Inverse problems for partial differential equations”, Springer Science & Business Media, **127**, 2006.
- [14] L. H. Thomas, “Using a computer to solve problems in physics”, *Applications of Digital Computers (Boston: Ginn and Company)*: 44–45, 1963.
- [15] G. Strang, “Computational science and engineering”, Wellesley-Cambridge Press Wellesley, **1**, 2007.

A Student-t based sparsity enforcing hierarchical prior for linear inverse problems and its efficient Bayesian computation for 2D and 3D Computed Tomography

Ali Mohammad-Djafari¹, Li Wang¹, Nicolas Gac¹ and Folkert Bleichrodt².

¹ Laboratoire des signaux et systèmes, CNRS, Centralesupélec-Univ Paris Saclay, Gif-sur-Yvette, France

² Centrum Wiskunde & Informatica (CWI), Amsterdam, The Netherlands

Abstract— In many imaging systems and in particular in X ray Computed Tomography (CT) the reconstruction problem can be written as a linear inverse problem. In these problems, one property which can often be exploited is sparsity of the solution in an appropriate basis. In this work we consider the Student-t model in its hierarchical Normal-Inverse Gamma with an appropriate dictionary based coefficient. Then, thanks to the hierarchical generative model of the observation, we derive the expression of the joint posterior law of all the unknowns and an alternate optimisation algorithm for obtaining the joint MAP solution. We then detail the implementation issues of this algorithms for parallel computation and show the results on real size 2D and 3D phantoms.

1 Introduction

In many imaging systems, very often the reconstruction problem can be written as a linear inverse problem. This is the case in X ray Computed Tomography (CT) [1, 2]. In these problems, the solution often has a sparse representation in a suitable basis. This sparsity property can be exploited in the reconstruction algorithm. For example, for a piecewise continuous or constant image, using Haar Transform (HT) gives rise to very sparse coefficients. To impose sparsity, three great categories of priors have been used: i) Generalized Gaussian (GG), ii) mixture of two Gaussian and iii) the heavy tailed probability density functions such as Cauchy and its generalisation a Student-t [3, 4, 5, 6].

In this work we consider Student-t model in its hierarchical Normal-Inverse Gamma with an appropriate dictionary based coefficient. Then, thanks to the hierarchical generative model of the observation, we derive the expression of the joint posterior law of all the unknowns and an alternate optimisation algorithm for obtaining the joint MAP solution.

We then detail the implementation issues of this algorithms for parallel computation and show the results on real size 2D and 3D phantoms.

2 Proposed model

We consider a linear model

$$\mathbf{g} = \mathbf{H}\mathbf{f} + \boldsymbol{\epsilon} \quad (1)$$

where \mathbf{f} is the object to be reconstructed, \mathbf{H} is the forward model, \mathbf{g} the observed quantities and $\boldsymbol{\epsilon}$ represents the errors. We choose an appropriate basis or dictionary \mathbf{D} for the object \mathbf{f} in such a way that we can write

$$\mathbf{f} = \mathbf{D}\mathbf{z} + \boldsymbol{\xi} \quad (2)$$

and such that \mathbf{z} is sparse. For imposing the sparsity of \mathbf{z} we propose to use the generalized Student-t prior for its elements z_j :

$$St(z_j|\alpha, \beta) = \int_0^\infty \mathcal{N}(z_j|0, v_{z_j}) \mathcal{IG}(v_{z_j}|\alpha, \beta) dv_{z_j} \quad (3)$$

which gives us the possibility to write

$$\begin{cases} p(z_j|v_{z_j}) = \mathcal{N}(z_j|0, v_{z_j}) \propto v_{z_j}^{-1/2} \exp\left[-\frac{1}{2} \sum_j \frac{z_j^2}{v_{z_j}}\right] \\ p(v_{z_j}) = \mathcal{IG}(v_{z_j}|\alpha_{z_0}, \beta_{z_0}) \propto v_{z_j}^{-(\alpha_{z_0}+1)} \exp\left[-\frac{\beta_{z_0}}{v_{z_j}}\right] \end{cases} \quad (4)$$

and where

$$p(\mathbf{z}|\mathbf{v}_z) = \prod_j p(z_j|v_{z_j}), \quad p(\mathbf{v}_z|\alpha_{z_0}, \beta_{z_0}) = \prod_j p(v_{z_j}|\alpha_{z_0}, \beta_{z_0})$$

and $p(\mathbf{z}, \mathbf{v}_z|\alpha_{z_0}, \beta_{z_0}) = p(\mathbf{z}|\mathbf{v}_z)p(\mathbf{v}_z|\alpha_{z_0}, \beta_{z_0})$.

In the forward model (1) and the prior model (2) we also use Student-t for the elements of $\boldsymbol{\epsilon}_i$ and ξ_j which give rise to the following relations:

$$\begin{cases} p(\mathbf{g}|\mathbf{f}, \mathbf{v}_\epsilon) = \mathcal{N}(\mathbf{g}|\mathbf{H}\mathbf{f}, \mathbf{V}_\epsilon) \text{ with } \mathbf{V}_\epsilon = \text{diag}[\mathbf{v}_\epsilon] \\ p(\mathbf{v}_\epsilon) = \prod_i \mathcal{IG}(v_{\epsilon_i}|\alpha_{\epsilon_0}, \beta_{\epsilon_0}) \end{cases} \quad (5)$$

and

$$\begin{cases} p(\mathbf{f}|\mathbf{z}, \mathbf{v}_\xi) = \mathcal{N}(\mathbf{f}|\mathbf{D}\mathbf{z}, \mathbf{V}_\xi) \text{ with } \mathbf{V}_\xi = \text{diag}[\mathbf{v}_\xi] \\ p(\mathbf{v}_\xi) = \prod_j \mathcal{IG}(v_{\xi_j}|\alpha_{\xi_0}, \beta_{\xi_0}) \end{cases} \quad (6)$$

With these prior models, we can show the graphical generative model of the data as follows:

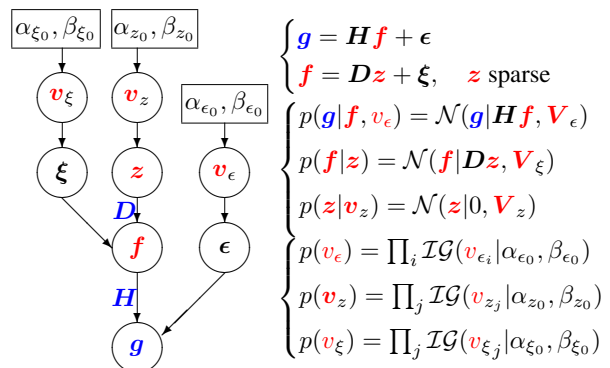


Figure 1: The graphical model of the generative forward model for linear inverse problems and hierarchical sparsity enforcing model.

With these relations and equations, the expression of the posterior law of all the unknowns writes:

$$p(\mathbf{f}, \mathbf{z}, \mathbf{v}_\epsilon, \mathbf{v}_z, \mathbf{v}_\xi|\mathbf{g}) \propto p(\mathbf{g}|\mathbf{f}, \mathbf{v}_\epsilon) p(\mathbf{f}|\mathbf{z}, \mathbf{v}_\xi) p(\mathbf{z}|\mathbf{v}_z) p(\mathbf{v}_\epsilon) p(\mathbf{v}_z) p(\mathbf{v}_\xi) \quad (7)$$

We can then use it for inferring these unknowns. Classically, there are two major estimators: JMAP and Posterior Means (PM). The JMAP writes:

$$(\hat{\mathbf{f}}, \hat{\mathbf{z}}, \hat{\mathbf{v}}_\epsilon, \hat{\mathbf{v}}_z, \hat{\mathbf{v}}_\xi) = \arg \max_{(\mathbf{f}, \mathbf{z}, \mathbf{v}_\epsilon, \mathbf{v}_z, \mathbf{v}_\xi)} \{p(\mathbf{f}, \mathbf{z}, \mathbf{v}_\epsilon, \mathbf{v}_z, \mathbf{v}_\xi | \mathbf{g})\} \quad (8)$$

for which, the easiest optimisation is alternate optimisation. Hopefully, with the proposed hierarchical structure and conjugate priors, in any of these steps we have analytical solutions:

$$\begin{cases} \mathbf{f} \leftarrow \arg \min_{\mathbf{f}} \left\{ J(\mathbf{f}) = \|\mathbf{g} - \mathbf{H}\mathbf{f}\|_{\mathbf{V}_\epsilon}^2 + \|\mathbf{f} - \mathbf{D}\mathbf{z}\|_{\mathbf{V}_\xi}^2 \right\} \\ \mathbf{z} \leftarrow \arg \min_{\mathbf{z}} \left\{ J(\mathbf{z}) = \|\mathbf{f} - \mathbf{D}\mathbf{z}\|_{\mathbf{V}_\xi}^2 + \|\mathbf{z}\|_{\mathbf{V}_z}^2 \right\} \\ v_{\epsilon_i} \leftarrow (\beta_{\epsilon_0} + \frac{1}{2}(g_i - [\mathbf{H}\mathbf{f}]_i)^2) / (\alpha_{\epsilon_0} + 3/2) \\ v_{\xi_j} \leftarrow (\beta_{\xi_0} + \frac{1}{2}(f_j - [\mathbf{D}\mathbf{z}]_j)^2) / (\alpha_{\xi_0} + 3/2) \\ v_{z_j} \leftarrow (\beta_{z_0} + \frac{1}{2}|z_j|^2) / (\alpha_{z_0} + 3/2) \end{cases} \quad (9)$$

As we can see, the main part of the algorithm is two optimizations of quadratic criteria which can also be written as

$$\begin{cases} J(\mathbf{f}) = \|\mathbf{g} - \mathbf{H}\mathbf{f}\|_{\mathbf{V}_\epsilon}^2 + \|\mathbf{f} - \mathbf{D}\mathbf{z}\|_{\mathbf{V}_\xi}^2 \\ = \|\mathbf{V}_\epsilon^{-1/2}(\mathbf{g} - \mathbf{H}\mathbf{f})\|_2^2 + \|\mathbf{V}_\xi^{-1/2}(\mathbf{f} - \mathbf{D}\mathbf{z})\|_2^2 \\ J(\mathbf{z}) = \|\mathbf{f} - \mathbf{D}\mathbf{z}\|_{\mathbf{V}_\xi}^2 + \|\mathbf{z}\|_{\mathbf{V}_z}^2 \\ = \|\mathbf{V}_\xi^{-1/2}(\mathbf{f} - \mathbf{D}\mathbf{z})\|_2^2 + \|\mathbf{V}_z^{-1/2}\mathbf{z}\|_2^2 \end{cases} \quad (10)$$

For implementation of the gradient based optimisation algorithms we need their gradients:

$$\begin{cases} \nabla J(\mathbf{f}) = -2\mathbf{H}'\mathbf{V}_\epsilon^{-1}(\mathbf{g} - \mathbf{H}\mathbf{f}) + 2\mathbf{V}_\xi^{-1}(\mathbf{f} - \mathbf{D}\mathbf{z}) \\ \nabla J(\mathbf{z}) = -2\mathbf{D}'\mathbf{V}_\xi^{-1}(\mathbf{f} - \mathbf{D}\mathbf{z}) + 2\mathbf{V}_z^{-1}\mathbf{z} \end{cases} \quad (11)$$

The algorithm we propose here which can be implemented efficiently and scale up for real applications and Big Data is as follows

$$\begin{cases} \mathbf{f} \leftarrow \mathbf{f} - \gamma_f \nabla J(\mathbf{f}) \\ \mathbf{z} \leftarrow \mathbf{z} - \gamma_z \nabla J(\mathbf{z}) \\ v_{\epsilon_i} \leftarrow (\beta_{\epsilon_0} + \frac{1}{2}(g_i - [\mathbf{H}\mathbf{f}]_i)^2) / (\alpha_{\epsilon_0} + 3/2) \\ v_{\xi_j} \leftarrow (\beta_{\xi_0} + \frac{1}{2}(f_j - [\mathbf{D}\mathbf{z}]_j)^2) / (\alpha_{\xi_0} + 3/2) \\ v_{z_j} \leftarrow (\beta_{z_0} + \frac{1}{2}|z_j|^2) / (\alpha_{z_0} + 3/2) \end{cases} \quad (12)$$

where γ_f and γ_z have to be adapted and updated at each iteration.

3 Simulation results

To show the effectiveness of the proposed method, we show here two examples of X ray image reconstruction from 32 projections. The images have 128x128 and 512x512 pixels and in both cases we simulated 32 projections uniformly distributed between 0 and 180 degrees. A Gaussian noise is added in such a way to have a SNR of 20dB.

We will show examples of 3D reconstruction results in the final paper. These results are obtained with objects of volume 256x256x256 and 32 projections of size 256x256.

4 Conclusion

We proposed a hierarchical Normal-Inverse Gamma prior for modelling the sparsity of both the error terms of the data-forward model and the error terms of dictionary based decomposition of the unknown images. With these priors we obtain

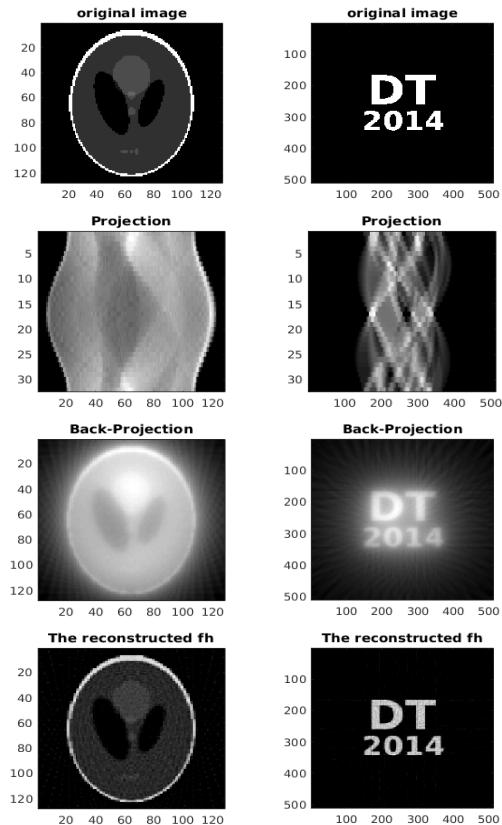


Figure 2: X ray CT: Originals, Projections, Initialization by Back-projection (BP), Reconstruction results.

an expression for the joint posterior law of all the unknowns (image itself \mathbf{f} , the coefficients of the decomposition \mathbf{z} and their respective hidden variances \mathbf{v}_ϵ , \mathbf{v}_ξ and \mathbf{v}_z). An approximate Bayesian Computation (ABC) based on the alternate optimization of this joint posterior law with respect its arguments gives an algorithm which can be implemented in an efficient way which can scales up for real applications.

References

- [1] A. Mohammad-Djafari, *Inverse Problems in Vision and 3D Tomography*. ISTE-WILEY, 2010.
- [2] K. Batenburg, S. Bals, J. Sijbers, C. Kubel, P. Midgley, J. Hernandez, U. Kaiser, E. Encina, E. Coronado, and G. Tendeloo, "3d imaging of nanomaterials by discrete tomography," *Ultramicroscopy*, vol. 109, no. 6, pp. 730–740, 2009.
- [3] J.-C. Baritau, K. Hassler, and M. Unser, "An efficient numerical method for general l_p regularization in fluorescence molecular tomography," *IEEE Transactions on Medical Imaging*, vol. 29, pp. 1075–1087, April 2010.
- [4] F. Luisier, C. Vonesch, T. Blu, and M. Unser, "Fast Haar-wavelet denoising of multidimensional fluorescence microscopy data," in *Proceedings of the Sixth IEEE International Symposium on Biomedical Imaging: From Nano to Macro (ISBI'09)*, (Boston MA, USA), pp. 310–313, June 28–July 1 2009.
- [5] A. Mohammad-Djafari, "Bayesian approach with prior models which enforce sparsity in signal and image processing," *EURASIP Journal on Advances in Signal Processing*, vol. Special issue on Sparse Signal Processing, p. 2012:52, 2012.
- [6] R. Leary, Z. Saghi, P. Midgley, and D. Holland, "Compressed sensing electron tomography," *Ultramicroscopy*, vol. 131, pp. 70–91, 2013.

Simultaneous reconstruction and separation in a spectral CT framework

S. Tairi¹, S. Anthoine², C. Morel¹ and Y. Boursier¹

¹Aix Marseille Université, CNRS/IN2P3, CPPM, UMR 7346, 13288 Marseille, France.

²Aix Marseille Université, CNRS, Centrale Marseille, I2M UMR 7373, 13453, Marseille, France

Abstract— In this paper, we propose a method to simultaneously separate and reconstruct the physical components of an object observed in the context of spectral Computed Tomography (CT). Spectral CT has been made possible by the technological breakthrough of X-ray hybrid pixel detectors in the last years and brings CT imaging from an anatomic to a functional biomedical imaging modality. Our paper considers the polychromatic model and combines it with a low-rank prior on the components. The simultaneous separation and reconstruction of the components is done by solving a non-convex ill-posed inverse problem. Promising results are shown on synthetic data with a simple regularization.

Introduction

The advent of new X-ray detection technology by hybrid pixel cameras working in a photon-counting mode opens a new field in tomographic X-ray imaging: the spectral Computed Tomography (CT). These new devices enrich the standard CT acquisition with a spectral information on the detected photons thanks to energy thresholds that can be set by the user. Such hyperspectral measurements pave the way to the identification, localization and quantification of biological markers like contrast agents and bring CT imaging from an anatomic to a functional biomedical imaging modality.

The problem in spectral CT is the simultaneous reconstruction and separation of spatio-spectral maps of absorption coefficients. A K-edge approach [8] firstly proved this possibility by coarsely approximating the acquisition model. Component separation methods [6, 7] also aimed at estimating components in the measurement space to subsequently reconstruct the spatial maps. We propose here to reconstruct the spatial and spectral characteristics simultaneously. We develop a complete mathematical polychromatic framework, similarly to [5], that encompasses strong physical priors based on a low-rank decomposition of the spatio-spectral map to be estimated. This investigation relies on the new generation of the XPAD3 hybrid pixel camera incorporated in the PIXSCAN-FLI prototype fully developed at CPPM.

1 Forward model

1.1 Acquisition model

A Computerized-Tomography (CT) scan is a set of measurements obtained by shining a rotating X-Ray light, modulated by spectral filters through an object. In the polychromatic setting, the p -th measurement y^p depends on

- the position of the source-detector couple with respect to the object, this is the line of sight \mathcal{L}^p ,
- the absorption coefficients of the object $\mu(l, E)$ for l on the line of sight \mathcal{L}^p ,

- the intensity energy spectrum of the X-ray source $I_0(E)$,
- the attenuation energy spectrum by the filter $Fi(E)$,
- the efficiency energy spectrum of the detector $De(E)$.

It is quantified by the Beer-Lambert law:

$$y^p = \int_{\mathbb{R}^+} I_0(E) Fi(E) De(E) e^{-\int_{\mathcal{L}^p} \mu(l, E) dl} dE. \quad (1)$$

The polychromatic CT reconstruction is the estimation of the map $\mu : \mathbb{R}^3 \times \mathbb{R}^+ \rightarrow \mathbb{R}^+$ from the knowledge of $I_0(E)$, $Fi(E)$ and $De(E)$ and a set of measurements y^p obtained by i) rotating the source/detector couple around the object, ii) changing the filters and iii) modifying the efficiency energy spectrum of the detector (*e.g.* by setting an energy discrimination threshold). $\mu(l, E)$ is the absorption coefficient of the object at point l and energy E .

Note that most of the literature on CT reconstruction considers the classical monochromatic setting, where the source is considered monochromatic ($I_0(E) = I_0 \delta(E - E_0)$, $I_0 \in \mathbb{R}^+$) so that $y^p = I_0 Fi(E_0) De(E_0) e^{-\int_{\mathcal{L}^p} \mu(l, E_0) dl}$. This case does not provide spectral information on absorption map. Recovering the spatial map $\mu(\cdot, E_0)$ from noisy measurements raises an ill-posed but usually convex inverse problem. By contrast, in the polychromatic setting, one is able to gather spectral information on the absorption map by combining the diversity at the detectors and at the source, using wide energy spectrum of the source intensity $I_0(E)$ and also different filters Fi .

Using P spatial configurations \mathcal{L}^p , Q spectral filters Fi and R settings per detector efficiency De , one obtains a set of $M = PQR$ measurements. Denoting $I_0(E) Fi^q(E) De^r(E) = f^m(E)$ the total spectral inputs, the m -th measurement reads:

$$y^m = \int_{\mathbb{R}^+} f^m(E) e^{-\int_{\mathcal{L}^m} \mu(l, E) dl} dE. \quad (2)$$

1.2 Absorption maps model

Recovering the full spatio-spectral absorption map might still be unrealistic with a finite number of measurements. However different components in an object, such as soft tissues, bones, etc., have a different spectral signature. A natural model for the absorption map is thus to consider it as the sum of the contribution of each of its components (say K in total): $\mu(l, E) = \sum_{k=1}^K \mu^k(l, E)$. The spectral signature is physically independent of the spatial location of a component, leading to:

$$\mu(l, E) = \sum_{k=1}^K \mu^k(l, E) = \sum_{k=1}^K a^k(l) \sigma^k(E), \quad (3)$$

with $a^k(l)$ the concentration of component k at point l , and $\sigma^k(E)$ its interaction cross section.

The perfect measurements now read:

$$y^m = \int_{\mathbb{R}^+} f^m(E) e^{-\sum_{k=1}^K \sigma^k(E) \int_{\mathcal{L}^m} a^k(l) dl} dE \quad (4)$$

1.3 Discretization

Let us discretize the energy E in N bins, and the 3D-volume where the object lives in D voxels and denote by $S[m, d]$ the contribution of the d -th voxel in the integral on \mathcal{L}^m , the forward discretized model reads:

$$Y[m] = \sum_{n=1}^N F[m, n] e^{-\sum_{k=1}^K \sum_{d=1}^D S[m, d] A[d, k] \Sigma[k, n]} \quad (5)$$

$$Y = (F \odot e^{-SA\Sigma}) \mathbb{1}_N,$$

with $F \in \mathbb{R}^{M \times N}$, $Y \in \mathbb{R}^M$, $A \in \mathbb{R}^{D \times K}$, and $\Sigma \in \mathbb{R}^{K \times N}$ the now discretized quantities. $\mathbb{1}_N$ is the column vector of length N filled with ones. \odot stands for the Hadamard product.

2 Reconstruction method

2.1 Inverse problem formulation

Let us consider that the measurements Y we have at hand are noisy versions of the perfect measurements described by Eq. (5). Our goal is to recover the matrix A containing the concentration coefficient maps of the K components of the object, from the knowledge of the noisy measurements Y , the experiment settings S , F and the spectral signatures Σ .

We propose to approach this inverse problem by minimizing

$$J(A) = D(Y, (F \odot e^{-SA\Sigma}) \mathbb{1}_N) + R(A) \quad (6)$$

with D a discrepancy measure for vectors and R a possibly non-smooth regularization term that models our a priori on A .

The discrepancy measure is naturally negative log-likelihood corresponding to the noise model, i.e. $D(Y, Z) = \sqrt{\sum_{m=1}^M (Y[m] - Z(m))^2}$ for i.i.d. Gaussian noise, or $D(Y, Z) = \sum_{m=1}^M D_{KL}(Y[m] - Z(m))$ for Poisson noise, with D_{KL} the Kullback-Leibler divergence.

Let us note that the polychromatic model leads to a discrepancy term which is non-convex in A . This was not the case in the classical monochromatic case and this renders the inverse problem quite more difficult. In this case, the sparse model designed on A will be the key to alleviate this problem.

2.2 A-priori on A

Firstly, the elements of A are concentration coefficients, so A is a non-negative matrix. Secondly, the number of components K in the object is typically much smaller than D the number of voxels in the model. A is thus a low-rank matrix. Modelling μ as $A\Sigma$ is not only physically sound but also a mathematical tool to render the non-convex problem at stake less ill-posed.

Here, we consider that the dictionary Σ is known from the experiment and we will assume that it is sufficiently incoherent to exploit the low-rank model. For example, we consider a dictionary of one soft component, and several contrast agents. The soft component has a polynomial decreasing spectral signature while contrast agents have a polynomial decreasing spectral signature with a discontinuity whose location is agent-specific.

The minimization of Eq. (6) with this model is a constrained non-convex model with $R(A)$ the indicator of non-negative

$D \times K$ matrices, that we investigate in the next experiments section with a simple trust-region algorithm.

Finer models on A may be considered. Each column of A is the concentration map of a physical component, and thus as was shown in [2] a sparse decomposition model or total variation model would yield more plausible maps. Each row of A corresponds to a voxel and thus is expected to contain only a few (say two or three) components. Additional row-wise sparsity would thus also be an asset. This type of regularization (both spatial and spectral) are captured by adding in $R(A)$ a structured sparsity term, for example a mixed normed [3]. The minimization of Eq. (6) is in this case, the sum of a non-convex differentiable term and a non-smooth but proximal term. In theory, it may be solved using algorithms such as [4]. However the large dimensions of the data renders for now such an implementation untractable.

3 Experiments

We generate a contrast phantom made of one large cylinder filled with water (this is the soft component in the dictionary), and six smaller tubes filled with contrast agents. Three tubes contain Yttrium at different concentrations, two contain Silver and one contains Iodine ($K = 4$). We simulate a set of tomographic measures corrupted by Gaussian noise with $Q = 5$ different spectral filters F_i , which are ideal pass-band filters around the discontinuities specifying the contrast agents. The discretized sizes are $M = 1440$, $D = 256$, and $N = 43$.

We minimize Eq. (6) with the non-negativity constraint using a trust-region algorithm [1] and report the results obtained for ten realizations of noise in Figure 1. They show that the low-rank model allows to reconstruct simple maps from non-linear polychromatic measurements. The output SNR evolves linearly with the input SNR. Note that the non-negative constraint is essential to obtain maps of good quality for realistic input SNR (i.e. SNR between 15 and 35).

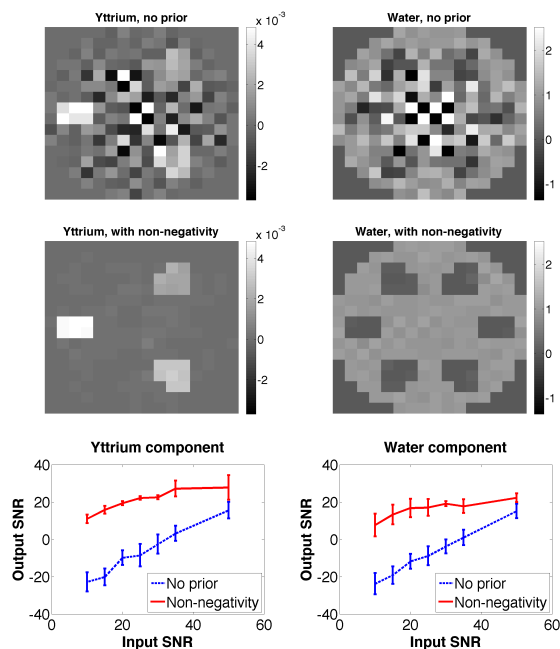


Figure 1: Reconstructions of the Yttrium (left) and the Water map (right) without (first row) or with (second row) non-negativity prior for an input SNR of 20 dB. Last row displays the input/output SNR evolution. The Silver and Iodine components exhibits results similar to the Yttrium component.

References

- [1] J. Nocedal and S. J. Wright. Numerical optimization. *Second edition 1999*.
- [2] S. Anthoine, J. F. Aujol, C. Mélot, and Y. Boursier. Some proximal methods for CBCT and PET tomography. *Inverse Problems in Imaging*, 6(4), Nov. 2012.
- [3] M. Kowalski. Sparse regression using mixed norms. *Applied and Computational Harmonic Analysis*, 27(3):303–324, 2009.
- [4] S. Bonettini and I. Loris and F. Porta and M. Prato. Variable Metric Inexact Line-Search-Based Methods for Nonsmooth Optimization. *Siam Journal on Optimization*, 26(2), 891-921, 2016. <http://dx.doi.org/10.1137/15M1019325>.
- [5] I. A. Elbakri and J. A. Fessler. Statistical image reconstruction for polyenergetic X-ray computed tomography. *IEEE Transactions in Medical Imaging*, 21(2):89–99, 2002.
- [6] J. P. Schlomka *et al.* Experimental feasibility of multi-energy photon-counting K-edge imaging in pre-clinical computed tomography. *Physics in Medicine and Biology*, 53(15):4031–4047, 2008.
- [7] M. Dupont *et al.* Component Separation for Spectral X-ray Imaging using the XPAD3 Hybrid Pixel Camera. *Proceedings of NSS/MIC 2013, IEEE Nuclear Science Symposium and Medical Imaging Conference*, 2013.
- [8] F. Cassol-Brunner *et al.* First K-Edge Imaging With a Micro-CT Based on the XPAD3 Hybrid Pixel Detector. *IEEE Transactions in Nuclear Science*, 60:103–108, 2013.

Debiasing incorporated into reconstruction of low-rank modelled dynamic MRI data

Marie Daňková^{1,2} and Pavel Rajmic¹

¹Department of Telecommunications, FEEC, Brno University of Technology, Czech Republic

²CEITEC, Masaryk University, Brno, Czech Republic

Abstract— Reconstruction of undersampled dynamic magnetic resonance imaging (MRI) data can be treated as a compressed sensing (CS) problem. Reconstruction using CS proved to be very useful in the area of MRI, but the estimates are biased due to convex relaxation of sparsity measures. Debiasing is a procedure usually carried out by the least squares method after the CS solution has been found. We show a method which debiases the estimates within a single procedure, when the CS problem, arising from the perfusion MRI analysis (DCE-MRI), involves a low-rank prior.

1 Introduction

Reconstruction procedures from compressed-sensed MRI data are often treated as optimization problems. The most popular approach is to solve convex problems including the ℓ_1 -norm [1, 2, 3]. It is known that this type of regularization seeks sparse solutions, however it gives biased estimates [4]. Debiasing is a postprocessing procedure commonly used in many applications, especially where the optimization criterion is penalized least squares. In LASSO-type problems [5], debiasing is performed such that an additional least squares estimate is run while the non-sparse support is fixed. In low-rank modelling, ℓ_1 -norm is applied on the singular values of a matrix. The debiasing procedure is more complicated [6], and especially, it turns out that it can amplify noise in the estimates. This paper shows a method which debiases the estimates within a single procedure.

2 Methods

Dynamic MRI often needs high temporal resolution of the acquisition to capture the vascular-distribution phase of the contrast agent, injected into a patient. Using the classic (i.e. Nyquist-rate) acquisition in MRI, it is impossible for both resolutions to be high at the same time. Therefore, much effort is devoted to using compressed sensing (CS) in MRI. In MRI, the images are acquired in their Fourier domain (also termed k-space). CS comes into play naturally by under-sampling of the k-space (sampling below the Nyquist rate).

The quality of CS reconstruction depends strongly on good prior knowledge about the signal. The assumption that different tissues have different but consistent perfusion characteristics is usually mathematically described by the low-rank property of the so-called Casorati matrix, which is an image sequence reshaped such that each image in time forms a column vector [7, 8]. Such a model of perfusion DCE-MRI can be mathematically formulated as

$$\hat{\mathbf{L}} = \arg \min_{\mathbf{L}} \frac{1}{2} \|\mathbf{Y} - E(\mathbf{L})\|_F^2 + \lambda \|\mathbf{L}\|_* \quad (1)$$

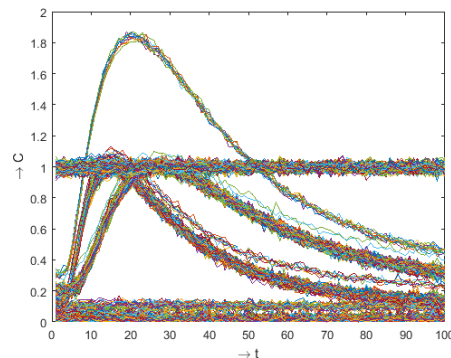


Figure 1: Reconstruction of phantom perfusion curves using CS with low-rank penalty, followed by least-squares debiasing

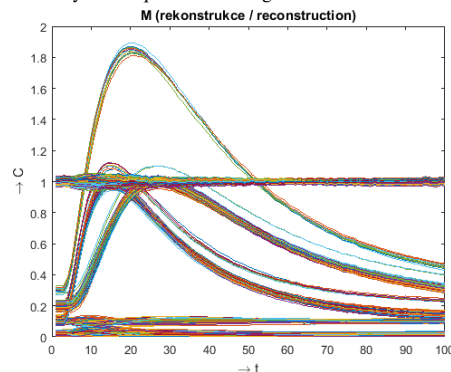


Figure 2: Reconstruction of phantom perfusion curves using CS with joint low-rank regularization and debiasing

where \mathbf{Y} is the casoritized k-t-space data, E is the subsampled Fourier transform w.r.t. \mathbf{Y} , and λ is a tuning parameter. The estimate $\hat{\mathbf{L}}$ represents the denoised evolution of the contrast agent concentration through time. Problem (1) can be solved using proximal algorithms [9]. The ordinary forward-backward algorithm consists of two steps per iteration: a gradient step w.r.t. data term and soft thresholding on the singular values. After each iteration (k) we know the current SVD decomposition $\mathbf{L}^{(k)} = \mathbf{U}^{(k)} \text{diag}(\sigma_1^{(k)}, \dots, \sigma_r^{(k)}) \mathbf{V}_r^{(k)*}$. Debiasing is then computed with fixed singular matrices $\mathbf{U}_r^{(k)}$, $\mathbf{V}_r^{(k)}$, which are restricted to positions of corresponding non-zero singular values. Formally, this is

$$\arg \min_{\substack{\sigma_1, \dots, \sigma_r > 0 \\ \sigma_i \in \mathbb{R}}} \left\| \mathbf{Y} - E \left(\mathbf{U}_r^{(k)} \text{diag}(\sigma_1, \dots, \sigma_r) \mathbf{V}_r^{(k)*} \right) \right\|_F^2, \quad (2)$$

and this sub-problem is solved by several repetitions of the gradient step w.r.t. σ_i and projecting its result to real, non-negative values. The described two-stage process repeats until convergence.

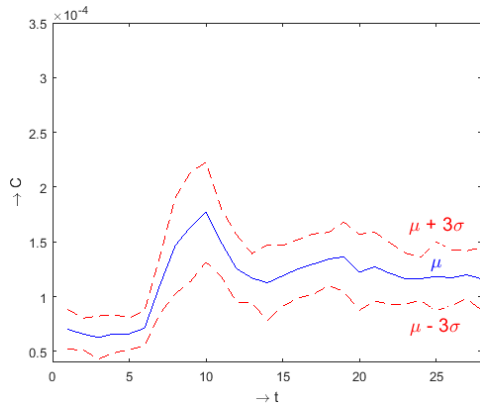


Figure 3: Reconstruction of perfusion curves in aorta using only low-rank prior on CS. Symbol μ stands for the mean of perfusion curves in the aorta area and σ is their standard deviation.

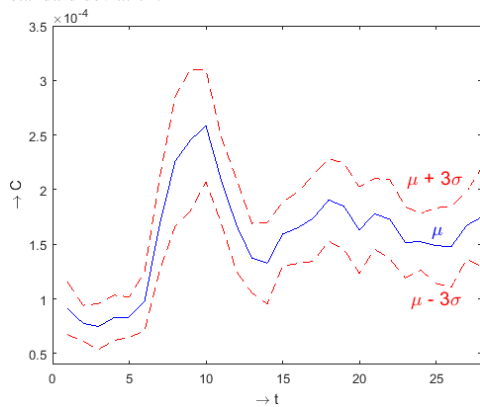


Figure 4: Reconstruction of perfusion curves in aorta with joint debiasing

We are not aware of any result specifying conditions that would guarantee the convergence of the proposed approach, however convergence has been achieved in all our experiments. Note that our procedure does not converge to $\hat{\mathbf{L}}$ from (1) but to an other matrix.

Simulation. Our algorithm has been first evaluated on a Shepp-Logan phantom [10]. The phantom has been modified to simulate perfusion using Matlab, see for example its use in [11]. We use a perfusion phantom of $100 \times 100 \text{ px} \times 100$ time points in size. The perfusion curves assigned to clearly separated areas of the phantom share the same behaviour in time, following the log-normal model [12]. At every time instant, the k-space values have been perturbed by additive Gaussian noise with standard deviation 0.05 to simulate the measurement noise. Such an experiment provided the possibility to compare to ground-truth data. The simulated acquisition used 100 radials per frame, where random slopes of spokes starting at the origin of k-space are used independently for each time frame.

Real data. We applied our algorithm to free-breathing abdominal DCE-MRI data [2]. The acquisition used golden-angle scheme using FLASH sequence on a whole-body 3T scanner (Magnetom Verio, Siemens Healthcare) with a 12-element receiver coil array. FOV = 380 mm^2 , 384 points per radial spoke, slice thickness 3 mm. For the reconstruction, 21 golden-angle radial trajectories per frame were used.

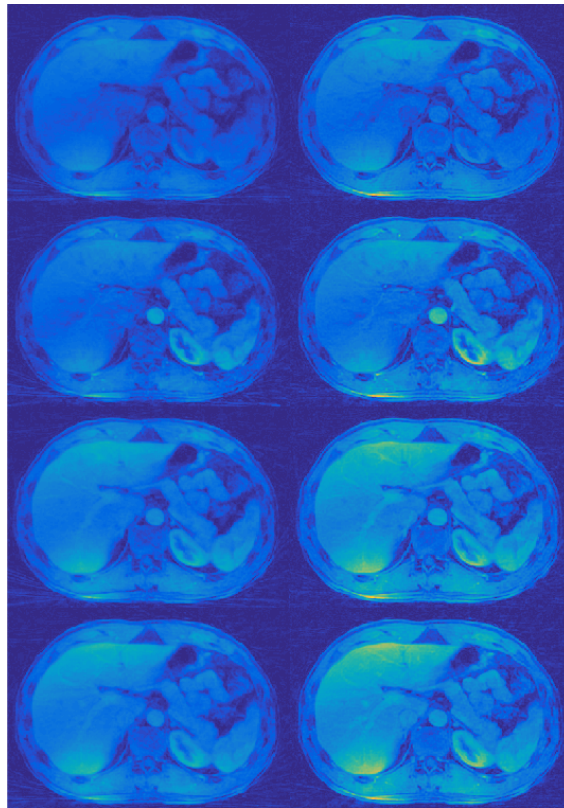


Figure 5: Reconstruction of dynamic MRI data using only low-rank prior on CS (left) and with incorporated debiasing (right); rows correspond to different time instances

3 Results

Simulation. We use compressed sensing (1) to reconstruct perfusion phantom. Using $\lambda = 3.525$, reconstruction resulted in SNR 26.46 dB and postdebiasing led to 22.86 dB (see Fig. 1). Our joint debiasing algorithm achieved 27.21 dB using $\lambda = 12$ (see Fig. 2). Fig. 1 shows that if the reconstruction contains singular vector corresponding to non-zero singular value that represents noise, debiasing increases this singular value and therefore noise is more notable. Conversely, if CS with joint debiasing is applied, singular vectors corresponding to noise are avoided.

Real data. Fig. 5 presents a comparison of reconstructions of a single slice in time; left column corresponds to results of (1) with $\lambda = 0.005\sigma_1$, the right column presents results for our algorithm using $\lambda = 0.025\sigma_1$. Figs. 3 and 4 show the respective intensity curves in the aorta. With debiasing, perfusion curves enjoy higher initial peak and the second peak is also more remarkable. Also other areas of the slices show greater contrast.

4 Conclusion

In this paper, we introduce a method which incorporates debiasing into CS reconstruction of low-rank modelled dynamic MRI data. We show better results obtained by this algorithm when compared to postdebiasing. We show this fact on both simulated and real dynamic data. In context of MRI, this method results in images with greater contrast, and noticeably, the aorta curve reveals a slightly better notion of blood cycle in humans.

References

- [1] Cohen, A., Dahmen, W., DeVore, R. Compressed sensing and best k -term approximation. *Journal of The American Mathematical Society*, vol. 22, 2009.
- [2] Otazo, R., Candes, E., Sodickson, D.K. Low-rank plus sparse matrix decomposition for accelerated dynamic MRI with separation of background and dynamic components. *Magnetic Resonance in Medicine*, 73(3), 2015.
- [3] Lingala, S., Hu, Y., DiBella, E. et al. Accelerated Dynamic MRI Exploiting Sparsity and Low-Rank Structure: k -t SLR. *Medical Imaging, IEEE Transactions on*, vol. 30, no. 5, 2011.
- [4] Bayram, İ. Penalty Functions Derived From Monotone Mappings. *IEEE Signal Processing Letters*, vol. 22, no. 3, 2015.
- [5] Tibshirani, R. Regression shrinkage and selection via the lasso. *Journal of the Royal Statistical Society. Series B (Methodological)*, vol. 58, no. 1, 1996.
- [6] Ma, S. Algorithms for Sparse and Low-Rank Optimization: Convergence, Complexity and Applications. Dissertation thesis, Columbia University, 2011.
- [7] N. Zhang, G. Song, W. Liao, et al. Accelerating dynamic contrast-enhanced MRI using K-T ISD. In *Proc. Intl. Soc. Mag. Reson. Med. 21*, page 4221, 2012.
- [8] Haoyu Wang, Yanwei Miao, Kun Zhou, Yanming Yu, Shanglian Bao, Qiang He, Yongming Dai, Stephanie Y. Xuan, Bisher Tarabishy, Yongquan Ye, and Jiani Hu. Feasibility of high temporal resolution breast DCE-MRI using compressed sensing theory. *Medical physics*, 37(9):4971–4981, September 2010.
- [9] P.L. Combettes and J.C. Pesquet. Proximal splitting methods in signal processing. *Fixed-Point Algorithms for Inverse Problems in Science and Engineering*, pages 185–212, 2011.
- [10] Shepp, L. A., Logan, B. F. The Fourier Reconstruction of a Head Section. *IEEE Transactions on Nuclear Science*, vol. 21, 1974.
- [11] Daňková, M., Rajmic, P., Jiřík, R. Acceleration of Perfusion MRI Using Locally Low-Rank Plus Sparse Model. In *Latent Variable Analysis and Signal Separation*. Liberec: Springer, 2015.
- [12] V. Harabiš, R. Kolář, M. Mézl, and R. Jiřík. Comparison and evaluation of indicator dilution models for bolus of ultrasound contrast agents. *Physiological Measurement*, 34:151–162, 2013.

Acknowledgement. The research was supported by the Czech Science Foundation grant no. GA15-12607S, by the Ministry of Education, Youth, and Sports of the Czech Republic (project LO1212), and by the SIX project CZ.1.05/2.1.00/03.0072.

Sparse MRI with a Markov Random Field Prior for the Subband Coefficients

Marko Panić*, Dejan Vukobratović†, Vladimir Crnojević* and Aleksandra Pižurica‡

*University of Novi Sad, BioSense Institute
mpanic@uns.ac.rs, crnjvc@gmail.com.

†University of Novi Sad, Department of Power, Electronics and Telecommunications
dejan.vukobratovic@gmail.com

‡Ghent University, Department Telecommunications and Information Processing, TELIN-IPI-iMinds
Aleksandra.Pizurica@ugent.be

Abstract—Recent work on compressed sensing in magnetic resonance imaging (CS-MRI) indicates benefits of modelling the *structure* of sparse coefficients. Comprehensive studies are available for tree-structured models. Much less work has been done on using statistical models for intra-scale (spatial) dependencies, like Markov Random Field (MRF) models in CS-MRI, although initial studies showed great potentials. We present here an efficient greedy algorithm with MRF priors and demonstrate encouraging performance in comparison to related methods, including those based on tree-structured sparsity.

I. INTRODUCTION

Compressed sensing (CS) for magnetic resonance imaging (MRI), dubbed CS-MRI, typically solves the problem

$$\min_{\mathbf{x}} \frac{1}{2} \|\mathbf{Ax} - \mathbf{y}\|_2^2 + \tau \phi(\mathbf{Px}) \quad (1)$$

where $\mathbf{x} \in \mathbb{C}^N$ is the ideal image and $\mathbf{y} \in \mathbb{C}^M$ are measurements obtained through partially observed Fourier transform $\mathbf{A} \in \mathbb{C}^{M \times N}$, $M \ll N$, with added noise $\mathbf{n} \in \mathbb{C}^M$ [1], [2]. $\mathbf{P} \in \mathbb{C}^{D \times N}$ denotes a sparsifying transform, $\tau > 0$ is a parameter and $\phi: \mathbb{C}^D \mapsto \mathbb{R} \cup \{-\infty, +\infty\}$ is a regularization function. When \mathbf{P} is a wavelet-like transform, ϕ is typically the ℓ_1 norm: $\phi(\boldsymbol{\theta}) = \|\boldsymbol{\theta}\|_1$. Another common regularization is Total Variation (TV), where \mathbf{P} is a discrete gradient operator. Compound regularization (a combination of ℓ_1 and TV) is often used as well [1]–[4]. Recent works incorporate modelling the *structured sparsity*, and in particular wavelet tree models have been proved beneficial in CS-MRI [5], [6]. An elegant algorithm LaMP (Lattice Matching Pursuit), which incorporates modelling of the spatial support of sparse images by a Markov Random Field (MRF), into a greedy solver was introduced in [7]. LaMP is not directly applicable to images that are not sparse in the canonical domain (and most MRI images are not). A related algorithm LaSB (Lattice Split Bregman) [8], which combines MRF modelling of the subband data with an augmented Lagrangian method showed promising results in MRI. It was unclear so far whether the success of LaSB could also be reached with a simpler, greedy type of methods, and it was also not clear how any of these methods would compare to alternative wavelet-tree sparsity methods [5], [6]. We address these questions and design a fast and simple MRF-based method for CS-MRI, demonstrating excellent performance.

II. A GREEDY CS-MRI ALGORITHM WITH MRF PRIORS

Let us first revisit briefly the original Lattice Matching Pursuit (LaMP) algorithm of [7], before analysing possible extensions to make it applicable to MRI. Our new algorithm, inspired by this analysis, will follow then.

The original LaMP, with the pseudocode (using our notation) in Alg. 1, assumes that the image is sparse in the canonical domain. Its main idea is to incorporate the estimation of the likely *support* \mathbf{s} of the actual signal into the matching pursuit iterations. In particular, Step 4 in each iteration k of Alg. 1 assigns to $\mathbf{s}^{\{k\}}$ the *maximum a posteriori* (MAP) estimate of the support of the temporary signal estimate $\mathbf{x}_t^{\{k\}}$, assuming a MRF prior for the support. With a homogeneous Ising model, with labels $s_i \in \{-1, 1\}$, and using the common conditional independence assumption for the likelihood $p(\mathbf{x}_t | \mathbf{s}) = \prod_i p([\mathbf{x}_t]_i | s_i)$, the MAP estimate of the support of $\mathbf{x}_t^{\{k\}}$ (denoted as *MAP-support* $\{\mathbf{x}_t^{\{k\}}\}$ in Alg. 1) is:

$$\mathbf{s}_{MAP}^{\{k\}} = \max_{\mathbf{s} \in \{-1, 1\}^N} \sum_{\langle i, j \rangle} \beta s_i s_j + \sum_i [\alpha s_i + \log(p([\mathbf{x}_t^{\{k\}}]_i | s_i))]$$

where β and α are the parameters of the Ising model, controlling the strength of the pair-wise clique potentials and the preference of one type of labels over the other, respectively¹. The pseudo-inversion \mathbf{A}^\dagger of the measurement matrix (Step 5) is then applied only for the columns of \mathbf{A} selected by $\mathbf{s}^{\{k\}}$. Additional pruning to K largest signal components (Step 6) yields the signal estimate $\mathbf{x}^{\{k\}}$.

This algorithm is directly applicable to the problem (1), only with $\mathbf{P} = \mathbf{I}$, where \mathbf{I} is the identity matrix. We need to extend it such that it works in the case where \mathbf{P} corresponds to a wavelet-like transform. A possible extension, which would allow applying LaMP to CS-MRI would be to replace steps 4-6 with:

$$\boldsymbol{\theta}_t^{\{k\}} = \mathbf{P} \mathbf{x}_t^{\{k\}}; \quad \mathbf{s}^{\{k\}} = \text{MAP-support}\{\boldsymbol{\theta}_t^{\{k\}}\} \quad (2a)$$

$$\boldsymbol{\theta}_{t'}^{\{k\}} = \mathbf{P} \mathbf{A}^\dagger \mathbf{y}; \quad \mathbf{t}[\mathbf{s}^{\{k\}} = 1] = \boldsymbol{\theta}_{t'}^{\{k\}}[\mathbf{s}^{\{k\}} = 1] \quad (2b)$$

$$\boldsymbol{\theta}^{\{k\}} = \text{Prune}(\mathbf{t}, K); \quad \mathbf{x}^{\{k\}} = \mathbf{P}^H \boldsymbol{\theta}^{\{k\}} \quad (2c)$$

¹In [7], a *non-homogeneous model* is allowed, with variable parameters $\beta_{i,j}$ and α_i depending on the spatial position, but this is not relevant here.

Algorithm 1 LaMP [7]

Input: $k = 1, \mathbf{y}, K, \mathbf{x}^{\{0\}}, \mathbf{t} = \mathbf{0}$

- 1: **repeat**{Matching Pursuit Iterations}
- 2: $\mathbf{r}^{\{k\}} = \mathbf{y} - \mathbf{A}\mathbf{x}^{\{k-1\}}$
- 3: $\mathbf{x}_t^{\{k\}} = \mathbf{A}^H \mathbf{r}^{\{k\}} + \mathbf{x}^{\{k-1\}}$
- 4: $\mathbf{s}^{\{k\}} = \text{MAP-support}\{\mathbf{x}_t^{\{k\}}\}$
- 5: $\mathbf{t} = \mathbf{0}; \quad \mathbf{t}[\mathbf{s}^{\{k\}} = 1] = \mathbf{A}^\dagger[\mathbf{s}^{\{k\}} = 1, :]\mathbf{y};$
- 6: $\mathbf{x}^{\{k\}} = \text{Prune}(\mathbf{t}, K)$
- 7: $k = k + 1$
- 8: **until** Maximum iterations or $\|\mathbf{r}^{\{k\}}\| \leq \text{threshold}$

Algorithm 2 The proposed algorithm: GreeLa

Input: $k = 1, \mathbf{y}, \mathbf{x}^{\{0\}}, \mathbf{t} = \mathbf{0}$

- 1: **repeat**
- 2: $\mathbf{r}^{\{k\}} = \mathbf{y} - \mathbf{A}\mathbf{x}^{\{k-1\}}$
- 3: $\mathbf{x}_t^{\{k\}} = \mathbf{A}^H \mathbf{r}^{\{k\}} + \mathbf{x}^{\{k-1\}}$
- 4: $\boldsymbol{\theta}_t^{\{k\}} = \mathbf{P}\mathbf{x}_t^{\{k\}}$
- 5: $\mathbf{s}^{\{k\}} = \text{MAP-support}\{\boldsymbol{\theta}_t^{\{k\}}\}$
- 6: $\mathbf{t} = \mathbf{0}; \quad \mathbf{t}[\mathbf{s}^{\{k\}} = 1] = \boldsymbol{\theta}_t^{\{k\}}[\mathbf{s}^{\{k\}} = 1]$
- 7: $\boldsymbol{\theta}^{\{k\}} = \mathbf{t}, \mathbf{x}^{\{k\}} = \mathbf{P}^H \boldsymbol{\theta}^{\{k\}}$
- 8: $k = k + 1$
- 9: **until** Maximum iterations or $\|\mathbf{r}^{\{k\}}\| \leq \text{threshold}$

Two important problems with this extension are: (i) the calculation of $\mathbf{P}\mathbf{A}^\dagger\mathbf{y}$ is costly, both in terms of the computation time and memory requirements and (ii) determining K in each subband is not trivial. Hence, we propose a simplified, greedy algorithm where the computation of the pseudo inverse is avoided by replacing $\boldsymbol{\theta}_t^{\{k\}}$ in (2b) by $\boldsymbol{\theta}_t^{\{k\}}$ and by excluding the additional pruning step (2c) (the sparseness is guaranteed already by the estimated support $\mathbf{s}^{\{k\}}$ using the right parameters of the prior MRF model). The proposed greedy algorithm named GreeLa (Greedy Lattice regularization) is summarized in Alg. 2. We employ the likelihood model from [8] and we also use the Metropolis sampler as in [8] for finding the MAP estimate of the support. Although there is no theoretical guarantee for the convergence at this point, the proposed method converges in practice relatively fast.

III. EXPERIMENTS AND DISCUSSION

In our experiments we used an MRI data set (brain scan) acquired on a Cartesian grid at the Ghent University hospital (UZ Gent)², also used in [8], [9]. Here we show the results on 248 sagittal slices from this data set (each slice is a 256×256 image, and Fig. 1 shows some of them). We report the results for simulated *radial* undersampling trajectories in the k -space with different sampling rates (similar results – not shown here – were obtained with other trajectories). For the sparsifying transform we used the non-decimated shearlet transform, with the implementation from [10], with 3 scales and 8, 4, and 2 orientations per scale (fine-to-coarse). We compare the

²Data acquired thanks to Prof. Dr. Karel Deblaere at the Radiology Department of UZ Gent.

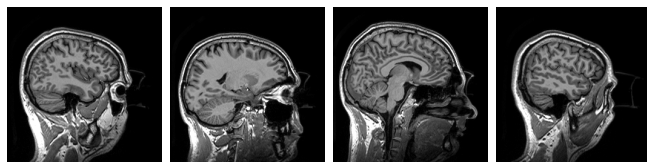


Fig. 1. Several sagittal slices from our MRI data set (256×256).

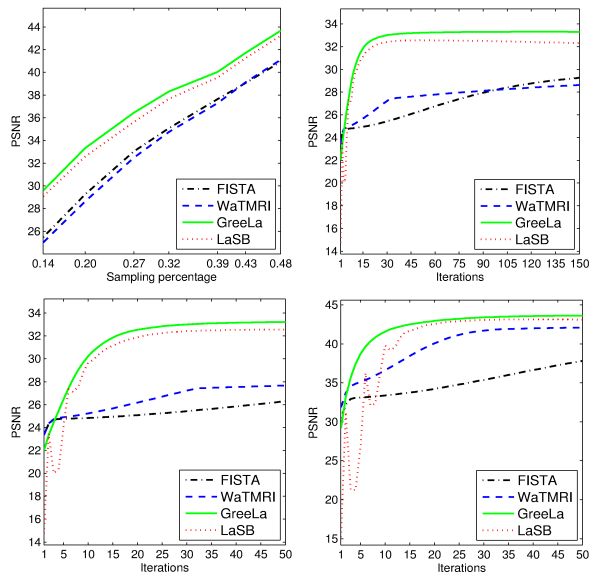


Fig. 2. **Top left:** PSNR for the reconstructions of one slice (second left in Fig. 1) for different sampling rates. **Top right** and **Bottom left:** Reconstruction performances on the same slice with 20% measurements in 150 and 50 iterations, respectively. **Bottom right:** Mean PSNR for 248 MRI slices with the sampling rate of 48%.

results to LaSB [8], FISTA [11] and the wavelet-tree sparsity (WaTMRI) method [5], [6] with the original implementation³. The MRF parameters were optimized separately for LaSB ($\alpha = .017, \beta = .07$) and for GreeLa ($\alpha = 1e-4, \beta = .34$). Fig. 2 shows the Peak Signal to Noise Ratio (PSNR) for one slice, with sampling rate (SR) ranging from 14% to 48%, and the evolution of the PSNR per iteration for a particular SR (20%). The MRF-based methods GreeLa and LaSB achieve a consistent and significant improvement in PSNR (up to 3 dB) compared to FISTA and WaTMRI for all SR values, and they also approach convergence in fewer iterations. GreeLa yields slightly higher PSNR than LaSB and shows a more stable behaviour in the first 20 iterations (see bottom left in Fig. 2). The average results on 248 MRI sagittal slices (bottom right in Fig. 2, SR=48%) lead to similar conclusions: although WaTMRI and FISTA increased their performances on average, GreeLa and LaSB yield a superior PSNR and converge in fewer iterations. A more stable behaviour of GreeLa compared to LaSB and slightly better PSNR are again observed. Given that the new algorithm is conceptually simpler, easier to implement and optimize, these results are highly encouraging.

³<http://ranger.uta.edu/~huang/index.html>

REFERENCES

- [1] M. Lustig, D. Donoho, and J. M. Pauly, "Sparse MRI: The application of compressed sensing for rapid MR imaging," *Magnetic Resonance in Medicine*, vol. 58, no. 6, pp. 1182–1195, 2007.
- [2] M. Lustig, D. L. Donoho, J. M. Santos, and J. M. Pauly, "Compressed sensing MRI," *IEEE Signal Processing Magazine*, vol. 25, no. 2, pp. 72–82, 2008.
- [3] J. Huang, S. Zhang, and D. Metaxas, "Efficient MR image reconstruction for compressed MR imaging," *Medical Image Analysis*, vol. 15, no. 5, pp. 670–679, 2011.
- [4] S. Ma, W. Yin, Y. Zhang, and A. Chakraborty, "An efficient algorithm for compressed MR imaging using total variation and wavelets," in *IEEE Conference on Computer Vision and Pattern Recognition (CVPR)*, 2008, pp. 1–8.
- [5] C. Chen and J. Huang, "Compressive sensing MRI with wavelet tree sparsity," in *Advances in neural information processing systems*, 2012, pp. 1115–1123.
- [6] C. Chen and J. Huang, "Exploiting the wavelet structure in compressed sensing MRI," *Magnetic Resonance Imaging*, vol. 32, no. 10, pp. 1377–1389, 2014.
- [7] V. Cevher, M. F. Duarte, C. Hegde, and R. Baraniuk, "Sparse signal recovery using Markov random fields," in *Advances in Neural Information Processing Systems*, 2009, pp. 257–264.
- [8] A. Pižurica, J. Aelterman, F. Bai, S. Vanloocke, Q. Luong, B. Goossens, and W. Philips, "On structured sparsity and selected applications in tomographic imaging," in *SPIE Conference on Wavelets and Sparsity XIV*, vol. 8138, 2011, pp. 81 381D–1–12.
- [9] J. Aelterman, H. Q. Luong, B. Goossens, A. Pižurica, and W. Philips, "Augmented Lagrangian based reconstruction of non-uniformly subnyquist sampled MRI data," *Signal Processing*, vol. 91, no. 12, pp. 2731–2742, 2011.
- [10] B. Goossens, J. Aelterman, H. Luong, A. Pižurica, and W. Philips, "Efficient design of a low redundant discrete shearlet transform," in *IEEE International Workshop Local and Non-Local Approximation in Image Processing (LNLA)*, 2009, pp. 112–124.
- [11] A. Beck and M. Teboulle, "A fast iterative shrinkage-thresholding algorithm for linear inverse problems," *SIAM Journal on Imaging Sciences*, vol. 2, no. 1, pp. 183–202, 2009.

Active GAP screening for the LASSO

A. Bonnefoy¹ and S. Anthoine².

¹Aix Marseille Université, CNRS, LIF, UMR 7279, 13288 Marseille, France.

²Aix Marseille Université, CNRS, Centrale Marseille, I2M UMR 7373, 13453, Marseille, France

Abstract— In this paper, we propose to combine two strategies to speed-up the resolution of Lasso-type problems, where the number of active variables in the solution is much smaller than the large number of variables of the initial problem. The first strategy is a dynamic screening test that eliminates variables that will not be active in the solution. The second strategy, the active-set strategy, works on the opposite direction by growing a set of variables that might be active in the solution. Numerical experiments show the effectiveness of this combination.

1 Introduction

In the context of sparse representations, LASSO-type problems are convex problems where the number k of active variables in the solution is much smaller than the large number of variables m of the initial problem. Global iterative minimisation methods used in this context, such as the well-known ISTA, may be significantly accelerated by optimisation techniques such as the two-steps acceleration obtained in FISTA or clever line-search techniques. However, these methods still require a number of evaluations of the full set of coefficients (i.e. products between the dictionary and a vector of length m). When the dictionary does not stem from a fast transform, as is the case for example in dictionary learning, and for large dimensional signals, these evaluations might still be prohibitive.

Two solutions have been proposed in the literature that reduce the size of the dictionary itself. Firstly, active-set methods have been proposed [5, 6]. Instead of working on the m variables, they rather try to identify the small set of variables that will be active (non-zero) in the solution. The so-called active-set is updated iteratively. Each iteration is computationally cheap because it involves only the variables in the active set that is kept small. Secondly, screening methods [3] on the contrary work on the set of inactive variables. More precisely, they identify through geometrical considerations variables that are probably not active in the solution.

In this paper, we combine the two approaches in a single procedure in order to sum up the acceleration effects obtained in either cases. The Active GAP procedure we propose is a combination of a classical active-set method with a state-of-the-art dynamic screening procedure. Numerical experiments show its effectiveness.

2 Active-sets meet dynamic screening

Let us consider the LASSO problem

$$x^* \triangleq \operatorname{argmin}_{x \in \mathbb{R}^m} \|Dx - y\|_2^2 + \lambda \|x\|_1 \quad (1)$$

for the signal y in \mathbb{R}^n and dictionary $D = (d_1, \dots, d_m)$ in $\mathbb{R}^{n \times m}$. The solution x^* depends on λ , so does its support

which is the set of indices of its active variables : $\{i = 1 \dots m / x^*(i) \neq 0\}$. The number k of active variables in the solution is much smaller than the total number of variables m for a large range of λ . The goal in both active-sets strategies and screening strategies is to exploit this fact to speed-up the computation time.

2.1 Dynamic screening

Screening strategies, originally introduced in [3], reduce the size of the dictionary D by eliminating atoms that will probably yield inactive variables in the solution x^* . The elimination is based on geometrical considerations in the dual.

The dual problem for the LASSO reads :

$$\begin{aligned} \theta^* \triangleq \operatorname{argmax}_{\theta} \frac{1}{2} \|y\|_2^2 - \frac{1}{2} \|\theta - y\|_2^2 \text{ such that} \\ \forall i = 1 \dots m, |d_i^T \theta| \leq \lambda, \end{aligned} \quad (2)$$

and the primal x^* and dual solutions θ^* are related by

$$y = Dx^* + \lambda \theta^* \text{ and} \quad (3)$$

$$\forall i = 1 \dots m \begin{cases} |d_i^T \theta^*| \leq \lambda & \text{if } x^*(i) = 0 \\ |d_i^T \theta^*| = \lambda & \text{if } x^*(i) \neq 0 \end{cases} \quad (4)$$

The dual solution θ^* is feasible (i.e. it verifies Eq. (2)) and its scalar products with the columns, or atoms, of the dictionary D identify inactive variables by Eq. (4). A screening test consists in designing a set that contains the solution θ^* , say \mathcal{S} , and bounding the scalar products of each atom with all elements of \mathcal{S} ; if the bound is smaller than λ , the atom yields an inactive variable. Usually, \mathcal{S} is a sphere or dome (intersection of a sphere and a half-space) thus rendering the computation of the bound analytical.

While in static screening, the atoms are eliminated once and for all before actually solving the minimization, in dynamic screening as introduced in [2], one proceeds to this elimination at each iteration of the minimization procedure, thus screening more atoms.

2.2 Active-sets

Active-set strategies [5, 6] work on the opposite on the set of active variables \mathcal{A} , starting with the empty set and growing it at each iteration. To update \mathcal{A} one considers $x_{\mathcal{A}}^*$ the solution of the LASSO subproblem:

$$z_{\mathcal{A}}^* \triangleq \operatorname{argmin}_{x \in \mathbb{R}^{|\mathcal{A}|}} \|D_{\mathcal{A}}x - y\|_2^2 + \lambda \|x\|_1 \quad (5)$$

$$\text{and } \begin{cases} x_{\mathcal{A}}^*(i) = z_{\mathcal{A}}^*(i) & \text{if } i \in \mathcal{A} \\ x_{\mathcal{A}}^*(i) = 0 & \text{otherwise} \end{cases} \quad (6)$$

for the subdictionary $D_{\mathcal{A}} = (d_i)_{\{i \in \mathcal{A}\}}$. The dual point $\theta_{\mathcal{A}}^* = y - Dx_{\mathcal{A}}^*$ verifies the KKT conditions (Eq. (4)) for the active

variables, but not necessarily for the inactive variables ($i \notin \mathcal{A}$). The one(s) which most violate(s) Eq. (4) are thus added to \mathcal{A} . One can also remove from the active set the variables in \mathcal{A} that are inactive in $x_{\mathcal{A}}^*$.

2.3 Active GAP screening

We propose to combine both active-set and screening strategies in an iterative scheme to solve the LASSO. At each iteration we will i) perform a screening test, ii) solve *approximately* a subproblem of the form (6), iii) update the active set.

The crux is to propose a screening test that is able to cope with the fact that at each iteration we only have access to an *approximate* solution of a *subproblem* of the LASSO. Having only an approximate solution is common with LASSO solvers, such as the ones we use here (ISTA and FISTA), but most screening techniques [3] require exact solutions. The screening test we propose here is inspired by the GAP test proposed in [4] that leverages on the duality gap to exploit only approximate solutions.

The GAP test [4] for the global LASSO problem builds a region \mathcal{S} that is a crescent moon (intersection of a ball with the complement of another ball) from an approximate solution x^+ and a feasible point θ for the global LASSO problem. \mathcal{S} is then bounded by a dome and the test derived.

The active GAP-test we propose requires only an approximate solution of the subproblem $x_{\mathcal{A}}^+$ and follows the steps :

- s.1. Compute the dual point $\theta = y - D_{\mathcal{A}}x_{\mathcal{A}}^+$. Derive by dual scaling a feasible point θ_{Γ} for the whole problem, and a feasible point $\theta_{\mathcal{A}}$ for the subproblem.
- s.2. Use the GAP procedure first on $x_{\mathcal{A}}^+$ and θ_{Γ} to obtain the red dome in Figure 1 containing θ^* .
- s.3. Since we do not have access to the optimal dual of the subproblem $\theta_{\mathcal{A}}^*$, we use the GAP procedure to obtain a set containing it. More precisely, we use the GAP procedure on $\theta_{\mathcal{A}}$ and $x_{\mathcal{A}}^+$, to obtain the blue crescent moon in Figure 1 containing the optimal dual of the subproblem $\theta_{\mathcal{A}}^*$.
- s.4. Each possible location of $\theta_{\mathcal{A}}^*$ defines a half-space containing θ^* . The extremal point θ_T of the blue crescent moon thus enables to define the half space characterized by the cyan hyperplane in Figure 1 whose normal vector is $n_{\mathcal{A}}$.
- s.5. The final screening set (green in Figure 1) is the intersection of the red dome and the half space defined just above.
- s.6. The screening test is derived.

The details of the screening sets and tests may be found in [1] and are not reproduced here by lack of space.

3 Experiments

The active GAP procedure has been implemented with a ISTA solver for the subproblems and tested on both synthetic and real datasets. The synthetic datasets are of two kinds. A k -sparse model x is generated using i.i.d. centered Gaussian values for the non-zero entries drawn at random. The signal y is generated using a classical i.i.d Gaussian dictionary in the case called *Gnoise*. A more correlated dictionary as proposed in [7] is used in the experiment called *Pnoise*, with $m = 5000$ and $n = 1000$. The real dataset is the *Leukemia* dataset.

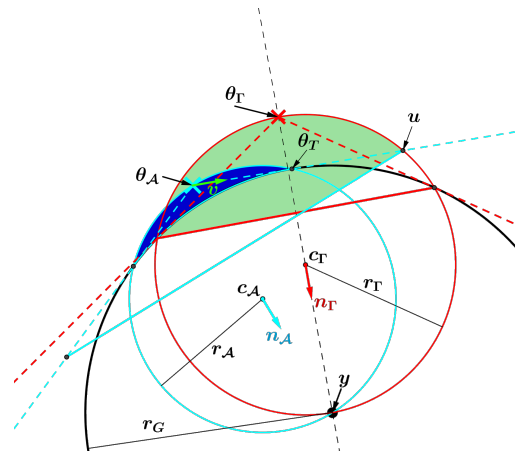


Figure 1: Active GAP set illustration. r_G is a radius given by the weak-duality property, it satisfies $\|\theta^* - y\| \geq r_G$ and $\|\theta_{\mathcal{A}}^* - y\| \geq r_G$. $c_{\mathcal{A}}$, $r_{\mathcal{A}}$, $n_{\mathcal{A}}$ and c_{Γ} , r_{Γ} , n_{Γ} are the center, the radius and the normal vector defining the dome constructed in s.2. and the dome constructed in s.4. respectively.

Each experiment is repeated 5 times. We compute the solutions up to a dual gap of 10^{-6} obtained by i) the plain ISTA, ii) ISTA with only GAP screening (GAP ISTA), iii) ISTA with only active sets (Active-Set ISTA) and iv) active GAP ISTA (Active GAP ISTA). The solutions are computed for a logarithmic grid of decreasing values for λ , using warm-start between two consecutive values. We report in Figure 2 the performances of three accelerated versions compared to the plain ISTA quantified by the ratio between the number of flops required by the accelerated version over the number of flops required by ISTA.

These graphs show that the three versions yield computational gain in the resolution of a LASSO problem. In the synthetic case however, the active strategy seems to bring the most substantial gain (up to ten times faster in the case of *Gnoise* and up to twenty times in the case of *Pnoise*). The addition of the screening via the active-GAP procedure proposed yields a substantial additional gain for larger values of λ .

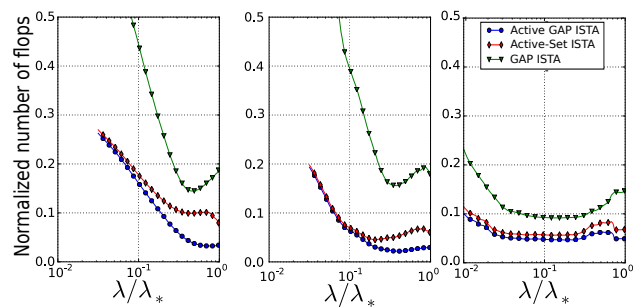


Figure 2: Normalized number of flops with respect to the ratio $\frac{\lambda}{\lambda^*}$ for the *Gnoise* synthetic data (left), *Pnoise* synthetic data (middle) and *Leukemia* dataset.

References

- [1] A. Bonnefoy. *PhD thesis, Aix-Marseille Université*, 2016.
- [2] A. Bonnefoy, V. Emiya, L. Ralaivola and R. Gribonval Dynamic Screening : Accelerating First-Order Algorithms for the Lasso and Group-Lasso. *IEEE Trans. Signal Process.* 2015.

- [3] L. El Ghaoui, V. Viallon and T. Rabbani Safe feature elimination in sparse supervised learning *CoRR*, 2010.
- [4] O. Fercoq, J. Salmon and A. Gramfort (2015). Mind the duality gap : safer rules for the Lasso. *Int. Conf. Mach. Learn*, Lille, 2015.
- [5] J. Nocedal and S. J. Wright. Numerical optimization. *Second edition 1999*.
- [6] V. Roth and B. Fischer The group-lasso for generalized linear models : uniqueness of solutions and efficient algorithms *Int. Conf. Mach. Learn.*, 2008.
- [7] Z.J. Xiang and P. J. Ramadge Fast lasso screening tests based on correlations. *ICASSP, IEEE Int. Conf. Acoust. Speech Signal Process. - Proc.* (2012).

Paint Loss Detection in Old Paintings by Sparse Representation Classification

Shaoguang Huang*, Wenzhi Liao*, Hongyan Zhang[†] and Aleksandra Pižurica*

*Ghent University, Department Telecommunications and Information Processing, TELIN-IPI-iMinds, Belgium
shaoguang.huang@ugent.be, wenzhi.liao@ugent.be, aleksandra.pizurica@ugent.be.

[†]The State Key Lab. of Inform. Engineering in Surveying, Mapping, and Remote Sensing, Wuhan University, China
zhanghongyan@whu.edu.cn

Abstract—In this paper, we explore the potential of sparse representation classification (SRC) in digital painting analysis, with the aim to aid the conservation/restoration treatment of old masterpieces. The focus is on detecting paint losses using multimodal acquisitions (such as optical images taken at different time instances before and during the conservation treatment, infrared images and digital radiography images). While SRC has been applied before in different scenarios, the present application requires some specific adaptations due to the nature and the size of the data, as well as the uncertainty to the labelled samples. Our initial results are very promising, compared to some more traditional or commonly used classification approaches, such as linear regression classification and support vector machines.

I. INTRODUCTION

Digital analysis of artworks, including digital painting analysis, is a rapidly growing field, attracting an increasing interest in the signal processing community [1]. Image processing techniques have already demonstrated potential in tasks such as characterization of painting style and forgery detection [2], [3], crack detection [4] and virtual inpainting [5], [6].

In this paper, we address the problem of detecting automatically paint losses revealed during the painting conservation treatments. Loss of paint in one or more layers can arise due to abrasion and mechanical fracture. In old oil paintings, paint losses were often overpainted during various restoration campaigns. Modern conservation treatments typically require not only removal of old varnish, but also removal of old retouches and overpaint, which may reveal paint losses underneath. Detection of such paint loss areas is of great importance to painting conservators for estimating the extent of the damaged area, which needs to be maintained for documenting purposes, but also as a crucial step for virtual inpainting to provide simulations for the actual restoration. Typically, digitized scans of masterpieces are taken in different modalities, including optical imaging, infrared reflectography and radiography. Painting conservators and restorers consult these various modalities to locate more reliably various areas of interest, such as overpaint and retouching, as well as paint losses. A well designed digital signal processing method for this purpose should also be able to combine efficiently this multi-modal information. We do not know of any reported signal/image processing techniques that address this specific problem. Currently, painting conservators typically use some semi-automatic tools in commercial programs, which includes



Fig. 1. A detail of *Prophet Zachariah* in three modalities (left to right): infra red and macro photograph before cleaning, and the macro photograph after the cleaning. Image copyright: Ghent, Kathedrale Kerkfabriek, Luksaweb.

a lot of manual work and hence enables annotating paint losses only in relatively small areas.

Technically, paint loss detection can be treated as a binary classification problem on a pixel level, assigning paint losses to a class of interest and all the rest to another class. Dictionary-based methods [7]–[14] have shown a great improvement over many popular classifiers (such as support vector machine (SVM) [15] and linear regression (LR) [16]) in many applications (*e.g.*, face recognition and iris recognition). Among the dictionary based methods, Sparse Representation Classification (SRC) [7] is attracting a lot of attention recently. While this method has been proved effective in various computer vision and remote sensing tasks, it has never been applied before to the type of problems that we are dealing with in this paper.

Before evaluating the potential of the SRC framework for paint loss detection, we need to address some specific problems: definition of the right features, dealing with extremely high spatial resolution, corrupted data samples and uncertainty to the labelled data. As a case study, we use the multimodal acquisitions of the *Ghent Altarpiece*, painted by brothers Van Eyck in the 15th century. Fig. 1 illustrates the employed imaging modalities on a piece of the panel *Prophet Zachariah*. The painting before the current conservation treatment (including the first two images from Fig. 1) can be viewed in high resolution at the website of the project *Closer to Van Eyck: Rediscovering the Ghent Altarpiece* (<http://closertovaneyck.kikirpa.be/>).



Fig. 2. Left to right: original image and paint loss detection results, marked in red, using linear regression classification on the visible modality alone, SVM on all the three modalities, and SRC on the same three modalities illustrated in Fig. 1.

II. PAINT LOSS DETECTION WITH SRC

Suppose there are C classes to be classified and $\mathbf{D}_i \in \mathbb{R}^{m \times n_i}$ ($i = 1, 2, \dots, C$), are the sub-dictionaries of a shared dictionary $\mathbf{D} = [\mathbf{D}_1, \mathbf{D}_2, \dots, \mathbf{D}_C] \in \mathbb{R}^{m \times n}$ ($n = \sum_i n_i$, $m > n$), where m is the data dimensionality and n_i is the number of training samples from the i -th class. In the SRC algorithm [7], each \mathbf{D}_i is composed of the samples from the i -th class. For a query signal $\mathbf{y} \in \mathbb{R}^m$, its sparse vector $\boldsymbol{\alpha}$ is first obtained

$$\hat{\boldsymbol{\alpha}} = \arg \min_{\boldsymbol{\alpha}} \|\mathbf{y} - \mathbf{D}\boldsymbol{\alpha}\|_2^2 + \lambda \|\boldsymbol{\alpha}\|_1 \quad (1)$$

where $\lambda > 0$ is a parameter that controls the trade-off between reconstruction error and sparsity, and each column of \mathbf{D} is normalized in ℓ_2 norm. The class is then identified as [7]:

$$\text{identity}(\mathbf{y}) = \arg \min_i \|\mathbf{y} - \mathbf{D}_i \hat{\boldsymbol{\alpha}}_i\|_2 \quad (2)$$

where $\hat{\boldsymbol{\alpha}}_i$ is the coefficient vector associated with class i .

We use the three modalities illustrated in Fig. 1 and the algorithm of [17] for registering them. Since our data are of extremely high spatial resolution, and may also be affected by scanning artefacts and noise, it would be unreliable to work with pixel-wise features alone. Therefore we make use of the local spatial information. In particular, we define our feature set as follows. Let the three registered imaging modalities make up a data cube, and refer to each of its layers as one component. Assuming raster scanning, let (j, k) denote the j th pixel in the k th component, and denote by $\mathbf{A}_{j,k} \in \mathbb{R}^{3 \times 3}$ a matrix of pixel intensities from a 3×3 window centred at j in the k th component. We compute a feature vector $\mathbf{y}_{j,k} = \{y_{1,j,k}, \dots, y_{N,j,k}\}$ from N features extracted from $\mathbf{A}_{j,k}$. In addition to mean, variance and range, we also utilize the correlation of neighbourhood, $\mathbf{A}'\mathbf{A}$ and $\mathbf{A}\mathbf{A}'$ (the correlation between each column and each row of \mathbf{A}). Only six entries are picked up in the upper triangular of $\mathbf{A}'\mathbf{A}$ and $\mathbf{A}\mathbf{A}'$ to avoid repeated elements. Finally, $\mathbf{y}_{j,k}$ are stacked to produce the feature vector \mathbf{y}_j for the j th spatial position.

In our problem, labelling of the training samples is extremely difficult and time consuming, and also highly prone to errors. Therefore, we run the SRC K times, each time using a different portion of the labelled data set for dictionary construction and for testing. This yields K classification results for each pixel. Let N_j^c denote the number of times that pixel j was assigned to class $c \in \{\text{PaintLoss}, \text{Other}\}$. The fraction $p_j^c = N_j^c / K$ is an empirical probability for the pixel j belonging to the class c . Hence, we finally select the identity (class) of each pixel as:

$$\text{identity}(\mathbf{y}_j) = \arg \max_c p_j^c \quad (3)$$

In practice, we obtain satisfactory results with $K = 5$.

III. RESULTS AND DISCUSSION

Fig. 2 illustrates the results on a part of the tested panel *Prophet Zachariah*. The size of the test image is 1945×1248 pixels and all training samples (7531 pixels in paint loss areas and 31296 pixels in other areas) were sampled manually. A randomly selected half of the labelled samples are used to construct the dictionary in each run. The second left image in Fig. 2 shows the result of linear regression classification, on a single modality only (visible after cleaning) to illustrate the difficulty of the problem. Notice that some obvious paint losses were not detected, while many false detections were already made (in the lower right part of the image). The SVM classifier (Gaussian kernel) was run using the optimization toolbox in MATLAB 2015b and parameter optimization by fivefold cross-validation. A visual assessment indicates slightly better performance of SRC compared to SVM: both methods locate similarly the paint loss areas, but SVM has more false detections (see the lower and right image parts). Although very encouraging, these initial results should still be taken with a reserve. Quantitative evaluation will be subject to future work, after obtaining reliable ‘ground truth’ labelling.

ACKNOWLEDGEMENT

The authors are grateful to Dr. Bruno Cornelis for registering the data sets and for useful discussions and also to Attila Fesus, Prof. Maximiliaan Martens and Prof. Ingrid Daubechies for many insightful discussions inspiring this work. We also thank painting conservators H el ene Dubois and Bart Devolder for providing the acquisitions of the painting taken during the conservation process.

REFERENCES

- [1] P. Abry, A. G. Klein, W. A. Sethares, and C. R. Johnson. Signal processing for art investigation. *IEEE Signal Processing Magazine*, 32(4):14–16, July 2015.
- [2] C. R. Johnson, E. Hendriks, I. J. Berezchnoy, E. Brevdo, S. M. Hughes, I. Daubechies, J. Li, E. Postma, and J. Z. Wang. Image processing for artist identification. *IEEE Signal Processing Magazine*, 25(4):37–48, July 2008.
- [3] L. Platiša, B. Cornelis, T. Ružic, A. Pižurica, A. Doods, M. Martens, M. De Mey, and I. Daubechies. Spatiogram features to characterize pearls in paintings. In *18th IEEE International Conference on Image Processing (ICIP)*, pages 801–804, 2011.
- [4] B. Cornelis, T. Ružic, E. Gezels, A. Doods, A. Pižurica, L. Platiša, J. Cornelis, M. Martens, M. De Mey, and I. Daubechies. Crack detection and inpainting for virtual restoration of paintings: The case of the ghent altarpiece. *Signal Processing*, 93(3):605–619, 2013.
- [5] T. Ružic, B. Cornelis, L. Platiša, A. Pižurica, A. Doods, W. Philips, M. Martens, M. De Mey, and I. Daubechies. Virtual restoration of the ghent altarpiece using crack detection and inpainting. In *Advanced Concepts for Intelligent Vision Systems*, pages 417–428, 2011.
- [6] A. Pižurica, L. Platiša, T. Ružic, B. Cornelis, A. Doods, M. Martens, H. Dubois, B. Devolder, M. De Mey, and I. Daubechies. Digital image processing of the ghent altarpiece: Supporting the painting’s study and conservation treatment. *IEEE Signal Processing Magazine*, 32(4):112–122, 2015.
- [7] J. Wright, A. Yang, A. Ganesh, S. Sastry, and Y. Ma. Robust face recognition via sparse representation. *IEEE Transactions on Pattern Analysis and Machine Intelligence*, 31(2):210–227, 2009.
- [8] L. Zhang, M. Yang, and X. Feng. Sparse representation or collaborative representation: Which helps face recognition? In *IEEE International Conference on Computer Vision (ICCV)*, pages 471–478, 2011.
- [9] M. Aharon, M. Elad, and A. Bruckstein. k-svd: An algorithm for designing overcomplete dictionaries for sparse representation. *IEEE Transactions on Signal Processing*, 54(11):4311–4322, Nov 2006.
- [10] Q. Zhang and B. Li. Discriminative k-svd for dictionary learning in face recognition. In *IEEE Conference on Computer Vision and Pattern Recognition (CVPR)*, pages 2691–2698, 2010.
- [11] Z. Jiang, Z. Lin, and L. S. Davis. Label consistent k-svd: Learning a discriminative dictionary for recognition. *IEEE Transactions on Pattern Analysis and Machine Intelligence*, 35(11):2651–2664, 2013.
- [12] M. Yang, X. F. L. Zhang, and D. Zhang. Fisher discrimination dictionary learning for sparse representation. In *IEEE International Conference on Computer Vision (ICCV)*, pages 543–550, 2011.
- [13] J. Mairal, F. Bach, and J. Ponce. Task-driven dictionary learning. *IEEE Transactions on Pattern Analysis and Machine Intelligence*, 34(4):791–804, 2012.
- [14] Q. Qiu, V. Patel, and R. Chellappa. Information-theoretic dictionary learning for image classification. *IEEE Transactions on Pattern Analysis and Machine Intelligence*, 36(11):2173–2184, 2014.
- [15] C. Cortes and V. Vapnik. Support-vector networks. *Machine learning*, 20(3):273–297, 1995.
- [16] E. Arthur and W. Robert. Ridge regression: Biased estimation for nonorthogonal problems. *Technometrics*, 12(1):55–67, 1970.
- [17] H.Q. Luong, B. Goossens, A. Piurica, and W. Philips. Joint photometric and geometric image registration in the total least square sense. *Pattern Recognition Letters*, 32(15):2061–2067, 2011.